Wide Bandgap Semiconductors Based Energy-Efficient Optoelectronics and Power Electronics

by

Houqiang Fu

A Dissertation Presented in Partial Fulfillment
of the Requirements for the Degree
Doctor of Philosophy

Approved February 2019 by the
Graduate Supervisory Committee:

Yuji Zhao, Chair
Dragica Vasileska
Stephen Goodnick
Hongbin Yu
Liping Wang

ARIZONA STATE UNIVERSITY

May 2019

ABSTRACT

Wide bandgap (WBG) semiconductors GaN (3.4 eV), Ga_2O_3 (4.8 eV) and AlN (6.2 eV), have gained considerable interests for energy-efficient optoelectronic and electronic applications in solid-state lighting, photovoltaics, power conversion, and so on. They can offer unique device performance compared with traditional semiconductors such as Si. Efficient GaN based light-emitting diodes (LEDs) have increasingly displaced incandescent and fluorescent bulbs as the new major light sources for lighting and display. In addition, due to their large bandgap and high critical electrical field, WBG semiconductors are also ideal candidates for efficient power conversion.

In this dissertation, two types of devices are demonstrated: optoelectronic and electronic devices. Commercial polar *c*-plane LEDs suffer from reduced efficiency with increasing current densities, knowns as "efficiency droop", while nonpolar/semipolar LEDs exhibit a very low efficiency droop. A modified *ABC* model with weak phase space filling effects is proposed to explain the low droop performance, providing insights for designing droop-free LEDs. The other emerging optoelectronics is nonpolar/semipolar III-nitride intersubband transition (ISBT) based photodetectors in terahertz and far infrared regime due to the large optical phonon energy and band offset, and the potential of room-temperature operation. ISBT properties are systematically studied for devices with different structures parameters.

In terms of electronic devices, vertical GaN p-n diodes and Schottky barrier diodes (SBDs) with high breakdown voltages are homoepitaxially grown on GaN bulk substrates with much reduced defect densities and improved device performance. The advantages of the vertical structure over the lateral structure are multifold: smaller chip

area, larger current, less sensitivity to surface states, better scalability, and smaller current dispersion. Three methods are proposed to boost the device performances: thick buffer layer design, hydrogen-plasma based edge termination technique, and multiple drift layer design. In addition, newly emerged Ga_2O_3 and AlN power electronics may outperform GaN devices. Because of the highly anisotropic crystal structure of Ga_2O_3, anisotropic electrical properties have been observed in Ga_2O_3 electronics. The first 1-kV-class AlN SBDs are demonstrated on cost-effective sapphire substrates. Several future topics are also proposed including selective-area doping in GaN power devices, vertical AlN power devices, and $(Al,Ga,In)_2O_3$ materials and devices.

ACKNOWLEDGMENTS

I am deeply grateful for my advisor Prof. Yuji Zhao for his endless help and guidance in both my research and personal life during these years, without whom all these works wound not be possible. I'd like to thank my committee members Prof. Dragica Vasileska, Prof. Stephen Goodnick, Prof. Hongbin Yu and Prof. Liping Wang for their many constructive advice and devoted efforts, which gave me new perspectives for my research. I also want to thank my group members Zhijian, Xuanqi, Hong, Xiaodong, Kai, Izak, Jossue, Tsung-han, Chen and Jinan, for their help in my research. I am especially grateful for being this great group: dynamic, collaborative, and productive, thanks to Prof. Zhao's effort to creating such a constructive group culture. I would also like to thank our collaborators from Dr. Ponce's group: Prof. Ponce, Hanxiao and Shanthan for their help in SEM and CL studies. I'd like to thank financial supports from Bisgrove Scholar Program from Science Foundation Arizona, Defense Threat Reduction Agency (DTRA) Young Investigator Award, and ARPA-E PNDIODES Program for this work. We gratefully acknowledge the use of facilities within the LeRoy Eyring Center for Solid State Science and ASU Nanofab at Arizona State University. We thank our collaborators from IQE and Kyma Technologies.

TABLE OF CONTENTS

Page

LIST OF TABLES vii

LIST OF FIGURES viii

CHAPTER

1 INTRODUCTION 1

1.1 III-nitride Devices for Optoelectronic and Electronic Applications 1

1.2 Wide Bandgap Semiconductors based Power Electronics 3

1.3 Polar, Nonpolar and Semipolar III-nitride 4

1.4 Growth of Bulk Substrates 7

1.5 Efficiency Droop in InGaN LEDs 8

1.6 Work Synopsis 10

2 LOW EFFICIENCY DROOP SEMIPOLAR INGAN LEDS AND THE MODIFIED *ABC* MODEL 12

2.1 Modified *ABC* Model 12

2.2 Carrier Lifetime Study 15

2.3 Simulation Results 19

3 INTERSUBBAND TRANSITION IN SEMIPOLAR ALGAN/GAN QUANTUM WELL AND THE CRYSTAL ORIENTATION EFFECTS 21

3.1 Simulation Method 21

3.2 Effect of Crystal Orientation 23

3.3 Effect of Quantum Well Thickness 27

3.4 Effect of Barrier Thickness 29

CHAPTER Page

3.5 Barrier Al Composition 31

3.6 Summary 33

4 VERTICAL GAN-ON-GAN P-N AND SCHOTTKY POWER DIODES WITH DIFFERENT BUFFER LAYER THICKNESS 34

4.1 Material Growth by MOCVD 35

4.2 Material Characterizations by XRD and AFM 36

4.3 Device Fabrication 37

4.4 Electrical Properties of P-N Diodes 38

4.5 Electrical Properties of Schottky Barrier Diodes 41

4.6 Summary 43

5 VERTICAL GAN-ON-GAN P-N DIODES WITH HYDROGEN-PLASMA BASED EDGE TERMINATION 44

5.1 Device Growth and Structure and Material Characterizations 44

5.2 Hydrogen-Plasma Treatment 46

5.3 Capacitance-Voltage (C-V) Characteristics 47

5.4 Forward Current-Voltage (I-V) Characteristics 47

5.5 Reverse Breakdow 48

5.6 Benchmark Plot 49

5.7 Summary 50

6 VERTICAL GAN-ON-GAN SCHOTTKY BARRIER DIODES WITH DOUBLE DRIFT LAYERS 51

6.1 Device Structure and Material Characterization 53

CHAPTER Page

6.2 Forward I-V Characteristics at Room Temperature (RT) 55

6.3 C-V Characteristics at RT 56

6.4 Reverse Breakdown at RT 57

6.5 Temperature-Dependent Forward I-V 58

6.6 Summary 60

7 OTHER WBG SEMICONDUCTORS BASED POWER ELECTRONICS 61

7.1 Ga_2O_3 based Power Electronics 61

7.1.1 Previous Studies on Material Anisotropy of Ga_2O_3 61

7.1.2 Surface Anisotropy Revealed by XPS 62

7.1.3 Anisotropic Electrical Properties of β-Ga_2O_3 SBDs 63

7.2 AlN based Power Electronics 68

7.2.1 Ohmic Contacts to n-AlN 69

7.2.2 Effect of Surface States on AlN SBDs 70

7.2.3 1-kV-Class AlN SBDs 72

7.2.4 Challenges and Proposed Work 75

8 CONCLUSIONS AND OUTLOOK 61

8.1 Conclusions 76

8.2 Outlook 77

REFERENCES 82

LIST OF TABLES

Table Page

1. Droop Ratio (%) of IQE Curves with Different n_0 at Differetn at Different Current Densities 13

2. Carrier Lifetime of Semipolar ($20\bar{2}\bar{1}$) and *C*-plane LEDs 17

3. The IQE, τ_{rad}, and τ_{nonrad} of ($20\bar{2}\bar{1}$) and *C*-plane InGaN LEDs 19

4. *A*, *B*, *C*, *d* and n_0 Coefficients Used in Modified *ABC* Model for Both *C*-plane and Semipolar InGaN LEDs 20

5. Material Parameters Used in SiLENSe....22

6. Structure Parameters of GaN P-N Diodes with Different Buffer Layers 36

7. Material Characterizations of Diode A and Diode B by HRXRD and AFM....54

8. Device Parameters of Diode A and Diode B 58

9. Device Parameters of ($\bar{2}01$) and (010) Ga_2O_3 SBDs 67

10. Properties of Si, SiC, GaN, and AlN Power Electronics 69

LIST OF FIGURES

Figure Page

1. Optoelectronic and Electronic Applications of III-Nitride Devices 1

2. (Left) Bandgap vs. Lattice Constant for III-Nitrides; (Right) Material Properties of III-Nitride Power Electronics. 2

3. Schematics of the Power Conversion Process 3

4. On-Resistance vs. Breakdown Voltage of Different Semiconductors 4

5. Different Planes of GaN Crystal. The Angles Indicate the Inclination Angles from the *C*-plane 4

6. (a) P_{pz}^{InGaN} and (b) ΔP_{tot} as a Function of θ for InGaN/GaN Heterostructure with In Compositions from 10% to 40% 6

7. Schematic Band Diagram and Electron and Hole Wavefunctions of (a) *C*-plane and (b) Nonpolar/Semipolar InGaN LEDs 7

8. IQE and Efficiency Droop vs. Current Density for a Typical *C*-plane InGaN LED 8

9. Calculated IQE Curves vs. Current Density with Different n_0. The Inset Shows the Peak IQEs and Peak Current Densities as a Function of n_0 13

10. Calculated IQE Curves vs. Current Density with Weak PSF Effect (Solid Line, $n_0 = 5\times 10^{19}$ cm^{-3}) and Strong PSF Effect (Dash Line, $n_0 = 3\times 10^{18}$ cm^{-3}) Varying (a) A (b) B (c) C and (d) d 14

11. TRPL Spectra of Semipolar $(20\bar{2}\bar{1})$ and *C*-plane LEDs 17

12. PL Spectra of (Left) Semipolar $(20\bar{2}\bar{1})$ and (Right) *C*-plane LEDs at 10K, 200K and 300K 18

Figure Page

13. Simulated IQE Curves for Reported Semipolar $(20\bar{2}\bar{1})$ LEDs, Nicha *C*-plane LEDs and UCSB *C*-plane LEDs 20

14. Conduction Band (CB) of AlGaN/GaN SQW on (a) *C*-plane, (b) $(10\bar{1}3)$, (c) $(20\bar{2}1)$, and (d) *M*-plane 24

15. ISBT Frequency and M_{12}/e of AlGaN/GaN SQW vs. Crystal Orientations 24

16. (a) Absorption Spectra for AlGaN/GaN SQW on Various Crystal Orientations. (b) Peak Absorption Coefficient and Peak Absorption Wavelength vs. Crystal Orientation 25

17. Peak Absorption QE and 50% Absorption QW Numbers vs. Peak Absorption Wavelength 26

18. (a) M_{12}/e and (b) ISBT Frequency of AlGaN/GaN SQW v.s. QW Thickness 27

19. Absorption Spectra of (a) *C*-plane, (b) $(10\bar{1}3)$, (c) $(20\bar{2}1)$ AlGaN/GaN SQW Varying QW Thickness. (d) Peak Absorption Coefficient and (e) Peak Absorption Wavelength vs. QW Thickness 28

20. (a) M_{12}/e and (b) ISBT Frequency of AlGaN/GaN SQW vs. Barrier Thickness 29

21. Absorption Spectra of (a) *C*-plane, (b) $(10\bar{1}3)$, (c) $(20\bar{2}1)$ AlGaN/GaN SQW Varying Barrier Thickness. (d) Peak Absorption Coefficient and Peak Absorption Wavelength vs. Barrier Thickness 30

22. CB of (a) *C*-plane, (b) $(10\bar{1}3)$, (c) $(20\bar{2}1)$, and (d) *M*-plane AlGaN/GaN SQW with Different Barrier Thicknesses 31

Figure Page

23. (a) ISBT Frequency and (b) M_{12}/e of AlGaN/GaN SQW vs. Barrier Al Composition. (c) Peak Absorption Wavelength and (d) Peak Absorption Coefficient vs. Barrier Al Composition 32

24. (a) Schematic Cross-Section View of Vertical GaN P-N Diodes. RCs of (b) (002) Plane and (c) (102) Plane 35

25. AFM Images of Sample (a) A, (b) B, (c) C, and (d) D 37

26. (a) Forward I–V Characteristics and R_{on} of Sample A, B, C,and D in Semilog Scale. The Insets Are Linear Scale I–V Curves. (b) EL Spectrum of Four Samples at A Forward Bias of 4 V. The Inset Shows Images of Illuminated Samples 38

27. Reverse I–V Characteristics of Sample A, B, C and D 40

28. (a) Forward I–V Characteristics and (b) Ideality Factor of SBD1, SBD2, SBD3, and SBD4 41

29. (a) C–V Characteristics at A Frequency of 1 MHz. The Inset Shows the Net Doping Concentrations for the Four Devices. (b) Comparison of Critical Electric Field of P-N Diodes with Different Buffer Layer thicknesses 42

30. Reverse I-V Characteristics of SBD1, SBD2, SBD3 and SBD4 43

31. Schematics of P-N Diodes (a) without (b) with H_2 Plasma Treatment 45

32. (a) RCs of the (002) Plane and the (102) Plane of Device. (b) The AFM Image of the Device with a $5 \times 5\ \mu m^2$ Scanning Area 45

33. I-V Curves of Two P-type Ohmic Contacts Before and After H_2 Plasma Treatment 46

Figure Page

34. (a) C and $1/C^2$ versus V at a Frequency of 1 MHz. (b) The Extracted Carrier Concentration Profile 47

35. (a) Forward I–V Characteristics of GaN P-N Diodes w/o and w/ the HEPT. (b) The Current Density, R_{on}, and Ideality Factor vs. Voltage for the Device w/ the HPET 47

36. Reverse I–V Characteristics Measured by (a) Keithley 2410 and (b) Tektronix 370A Curve Tracer 48

37. Benchmark Plot of R_{on} vs. V_{BD} for Vertical GaN P-N Diodes. The Publication Year and the Drift Layer Thickness in µm of Each Device are Marked 49

38. Theoretical Calculation of Electric Fields by One-Dimensional Poisson's Equation for SDL Structure Biased at −2.7 kV, DDL Structure with High UID Top Drift Layer Biased at −3.4 kV, and DDL Structure with Low UID Top Drift Layer Biased at −4.1 kV. Breakdown was Assumed to Occur at A Peak Electric Field of 3.3 MV/cm 52

39. Schematic View of Cross-Section (Left) and Device Structure (Right) for Diode A and B 53

40. (a)-(b) (002) and (102) RCs. (c)-(d) AFM Images 54

41. (a) Forward Current and Ideality Factor vs. Voltage in Linear Scale. (b) Forward Current Density and R_{on} vs. Voltage in Semi-Log Scale. (c) Comparison of V_{on} and R_{on} of Reported Vertical GaN SBDs 55

42. (a) C–V and (b) $1/C^2$–V Characteristics of Diode A and B at 1 MHz 56

43. (a) Reverse I–V Characteristics of Diode A and B. The Inset Shows V_{BD} of

Figure Page

Diode A and B. (b) Electric Field Profiles of Diode A and B 57

44. Temperature-Dependent Forward I–V Characteristics for (a) Diode A and (b) Diode B. (c) Richardson Plot of the Two Diodes with Schottky Barrier Height Extracted. (d) Ideality Factor and R_{on} vs. Temperature 59

45. Mobility vs. Temperature for (a) Diode A and (b) Diode B in Log-Log Scale 60

46. (a) Unit Cell of β-Ga_2O_3 Crystal. Surface of (b) ($\bar{2}01$) and (c) (010) Plane 62

47. XPS VB Spectra of (a) ($\bar{2}01$) and (b) (010) β-Ga_2O_3. The Insets Indicate the Upward Band Bending at the Surfaces 63

48. (a) Current and Ideality Factor vs. Forward Bias in Linear Scale. (b) Current Density and R_{on} vs. Forward Bias in Semi-Log Scale. (c) Comparison of R_{on} of β-Ga_2O_3 SBDs on Different Orientations. (d) Comparison of Φ_B of Reported ($\bar{2}01$) and (010) β-Ga_2O_3 SBDs 64

49. (a) C–V and (b) $1/C^2$–V Characteristics of ($\bar{2}01$) and (010) SBDs at 1 MHz. The Inset in the Right Figure Shows the Band Diagram of β-Ga_2O_3 Schottky Interface 65

50. Temperature-Dependent I–V Characteristics. (c) Ideality Factor and Φ_B vs. Temperature. (d) Φ_B vs. Ideality Factor 66

51. (a) Arrhenius Plot of Reverse Leakage Current. (b) Conductivity as a Function of $1/T^{1/2}$. The Insets Show the Electron Transport Models 67

52. (a) TLM I–V Characteristics of the Ohmic Contacts at RT. (b) Contact Resistance and Sheet Resistance vs. Temperature 70

Figure Page

53. (a) Schematic View of the Cross-Section of a Lateral AlN SBD. (b) Top View of AlN SBDs with Different Geometries 70

54. (a) Temperature-Dependent Reverse I–V Characteristics of AlN SBDs. (b) V_{BD} vs. Temperature 71

55. (a) Temperature-Dependent Reverse Leakage Current at Different Reverse Voltages. (b) Conductivity of AlN SBDs as a Function of $1/T^{1/3}$ at Different Reverse Voltages 72

56. (a) V_{BD} vs. Contact Distance. (b) Leakage Current vs. Contact Distance at Different Reverse Voltages 72

57. Schematic View of the Fabricated AlN SBDs 73

58. (a) Temperature-Dependent Forward I–V Characteristics. (b) The Richardson Plot from 1.6 V to 2.0 V 73

59. C-V and $1/C^2$ vs. V Characteristics for AlN SBDs at 1 MHz 74

60. (a) Reverse I-V Characteristics of Circular and Square AlN SBDs. (b) Comparison of V_{BD} and V_{on} of Reported AlN SBDs 74

61. (a) Schematics of the Selective-Area Doping and the Resulting Lateral p-n Junction. (b)-(c) The Epitaxial Growth and Regrowth Process for the Lateral p-n Junction 78

62. (a) JBS or MPS Diodes. (b) Superjunctions. (c) VJFETs 78

63. (a) SIMS Profile of the Regrown p-n Junction. (b) TEM Images of the Regrown p-n Junction Interface. (b) CL Image of the Regrown p-n Junction 79

64. (a) XPS Valence Band Spectrum of AlN. (b) Vertical AlN SBDs. (c) Vertical

Figure Page

AlN FinFETs 80

65. Band Alignments between In_2O_3, Ga_2O_3 and Al_2O_3 81

CHAPTER 1

INTRODUCTION

1.1 III-nitride Devices for Optoelectronic and Electronic Applications

Wurtzite (Al, Ga, In)N wide bandgap III-nitride semiconductors have attracted tremendous attention due to their successful applications (Fig. 1) in optoelectronics such as blue and green light-emitting diodes (LEDs) [1]-[4], laser diodes (LDs) [5], intersubband transition (ISBT) based emitters and photodetectors [6], photovoltaics [7]-[9], nonlinear optics [10], and power electronics such as high electron mobility transistors (HEMTs) [11], p-n diodes [12], and Schottky barrier diodes (SBDs) [13]. InGaN LEDs have enabled efficient solid-state lighting, full-color displays, visible light communication, and so on [5]. LEDs have been considered as the future general light sources to replace the traditional source such as fluorescent lamps and incandescent bulbs, due to its high efficiency and long lifetime. InGaN LDs are popular candidates for high intensity automobile headlights and miniaturized projectors.

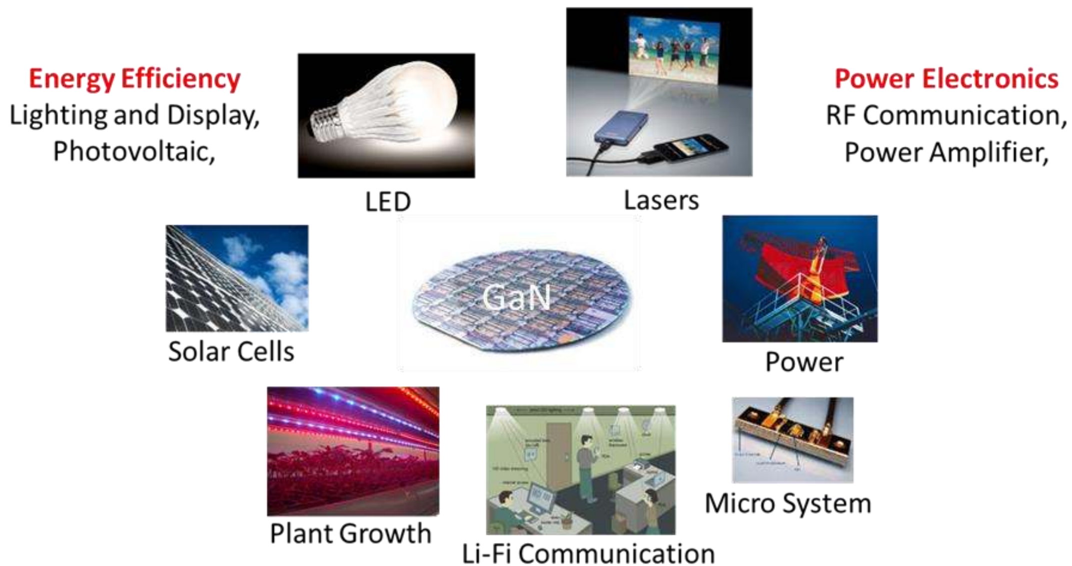

Fig. 1. Optoelectronic and electronic applications of III-nitride devices [14].

In terms of III-nitride ISBT devices, due to their large optical phonon energy (~ 90 meV), large band offset (~ 2 eV for GaN/AlN) and ultrafast carrier dynamics (~ 100 fs) [15], [16], they will offer excellent device performance for high temperature terahertz (THz) and far infrared (FIR) applications. THz region is loosely defined as 1-10THz, which corresponds to wavelengths ranging from 30 µm–300 µm (FIR region). THz or FIR devices are highly desired for various applications such as healthcare, medical imaging, biological analysis, security and communication [17]. InGaN alloys can cover the whole solar spectrum (Fig. 2), which makes InGaN an ideal candidate for photovoltaics. Recently, III-nitride based power electronics are becoming hot topics because of their high breakdown field and high electronic mobility. These properties make III-nitride electronics superior to Si based devices in power switching and RF applications. And III-nitride HEMTs have already been commercialized.

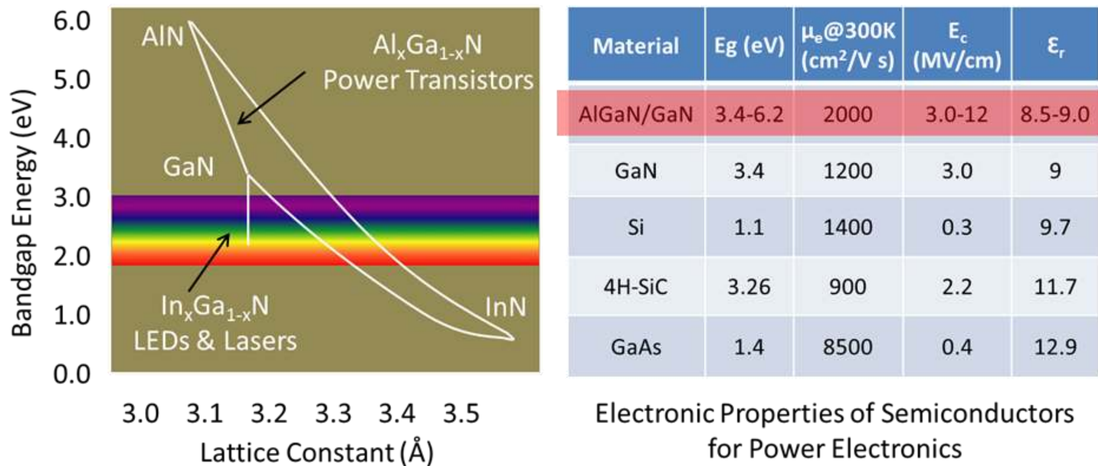

Material	Eg (eV)	μ_e@300K (cm^2/V s)	E_c (MV/cm)	ε_r
AlGaN/GaN	3.4-6.2	2000	3.0-12	8.5-9.0
GaN	3.4	1200	3.0	9
Si	1.1	1400	0.3	9.7
4H-SiC	3.26	900	2.2	11.7
GaAs	1.4	8500	0.4	12.9

Electronic Properties of Semiconductors for Power Electronics

Fig. 2. (Left) Bandgap vs. lattice constant for III-nitrides; (Right) Material properties of III-nitride power electronics.

1.2 Wide Bandgap Semiconductors based Power Electronics

Power conversion refers to the process of the electrical power transfer from a power source to a load by converting currents and voltages from one form to another, such as from alternate current (AC) to direct current (DC), DC to AC, AC to AC and DC to DC. This process is indispensable since the power source and the load often differ in voltages, frequencies and phases. Power conversion is ubiquitous in the electricity-dependent modern society. And the applications are everywhere: smart grid, Internet, renewable energy, data center, automobiles, smart phones, household appliances, rail tractions, ships, motors, etc. At the heart of the power conversion process is power electronics. Figure 3 schematically shows the power conversion process.

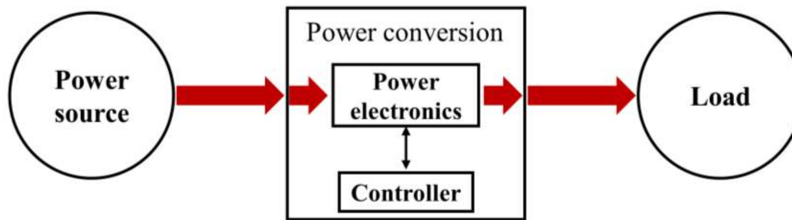

Fig. 3. Schematics of the power conversion process [12].

An efficient power electronic device should have a high breakdown voltage (V_{BD}) in the OFF state and a low on-resistance (R_{on}) in the ON state in order to reduce power conversion losses. Figure 4 shows R_{on} versus V_{BD} for different semiconductors [18]. The recent advent of wide bandgap (WBG) semiconductors such as GaN (3.4 eV), Ga_2O_3 (4.8 eV) and AlN (6.0 eV), has completely transformed the technological landscape of power electronics. With the same R_{on}, WBG semiconductors can achieve larger V_{BD} than conventional semiconductors such as Si (1.1 eV), GaAs (1.4 eV) and SiC (3.3 eV); with the same V_{BD}, they show smaller R_{on}. Therefore, WBG semiconductors are ideal

candidates for high performance power electronics. Currently, power conversion losses using silicon-based devices are ~ 10% of the total electricity generated in the U. S., which is more than all the electricity generated by renewable energy sources combined [18]. It's imperative to develop more efficient power electronics based on WBG semiconductors.

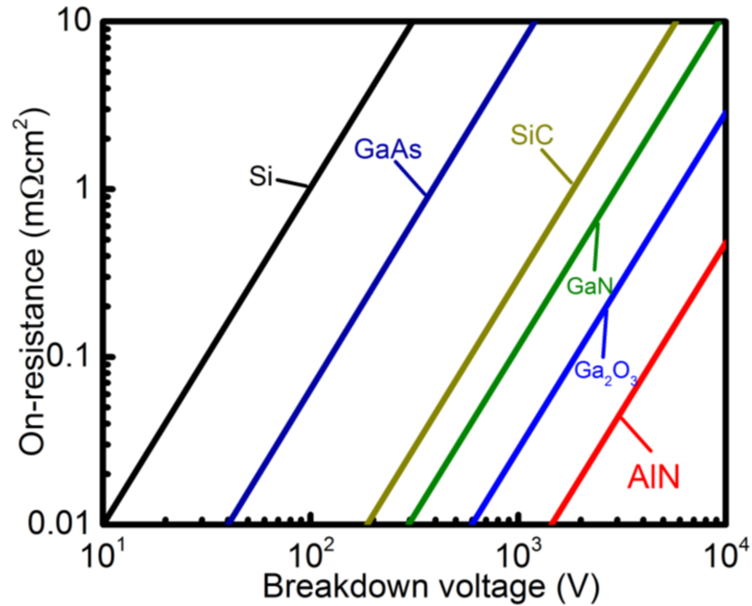

Fig. 4. On-resistance vs. breakdown voltage of different semiconductors [18].

1.3 Polar, Nonpolar and Semipolar III-nitride

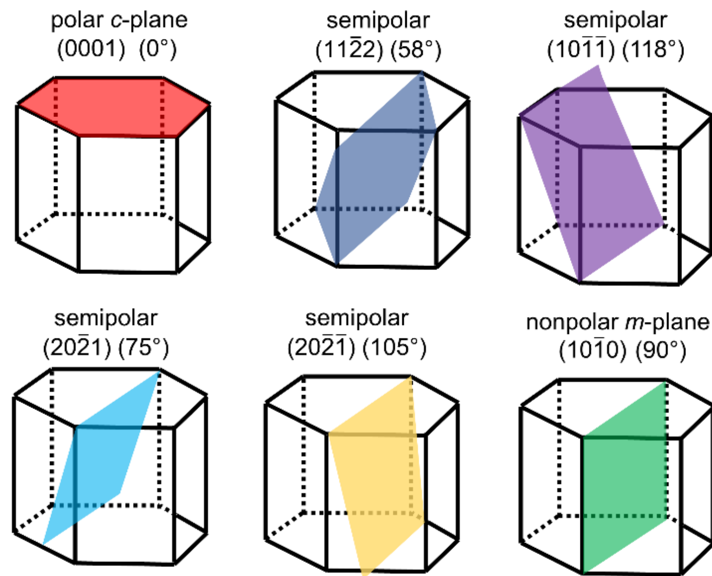

Fig. 5. Different planes of GaN crystal. The angles indicate the inclination angles from the *c*-plane [19].

Wurtzite III-nitride crystal has many planes as shown in Fig. 5, which can be categorized into polar planes such as (0001) *c*-plane, nonpolar planes such as $(10\bar{1}0)$ *m*-plane, and semipolar planes such as $(30\bar{3}1)$, $(20\bar{2}1)$, $(10\bar{1}1)$, $(10\overline{11})$ and $(11\bar{2}2)$ [19]. III-nitrides have strong spontaneous polarization along the [0001] *c*-axis due to the lack of inversion symmetry and piezoelectric polarization due to the lattice mismatch and strain [20], [21]. Take the coherently grown InGaN quantum well (QW) on GaN as an example. The total polarization difference at the InGaN/GaN interface consists of spontaneous polarization plus piezoelectric polarization difference. Romanov *et al.* proposed an easy-to-use method to calculate the polarization of any crystal planes [21]. The primed z' is along the growth direction and x' and y' are in the substrate surface plane. For a plane inclined from *c*-plane by an angle of θ, the total polarization difference along z' direction at InGaN/GaN interface is given by [20], [21]

$$\Delta P_{tot} = P_{pz}^{InGaN} + (P_{sp}^{InGaN} - P_{sp}^{GaN})\cos\theta \qquad (1)$$

where ΔP_{tot} is the total polarization difference between InGaN layer and GaN template, and P_{sp}^{InGaN} and P_{sp}^{GaN} are the spontaneous polarization of InGaN layer and GaN template, respectively. P_{pz}^{InGaN} is the strain-induced piezoelectric polarization in InGaN layer, which be expressed as [20], [21]

$$P_{pz}^{InGaN} = e_{31}\cos\theta\epsilon_{x'x'} + \left(e_{31}\cos^3\theta + \frac{e_{33}-e_{15}}{2}\sin\theta\sin2\theta\right)\epsilon_{y'y'} + \left(\frac{(e_{31}+e_{15})}{2}\sin\theta\sin2\theta + e_{33}\cos^3\theta\right)$$
$$\epsilon_{z'z'} + [(e_{31}-e_{33})\cos\theta\sin2\theta + e_{15}\sin\theta\cos2\theta]\epsilon_{y'z'} \qquad (2)$$

where elements $\epsilon_{k'm'}$ are the strain tensor components and elements e_{ij} are the components of piezoelectric tensor in Voigt notation. Figure 6 presents polarizations of InGaN/GaN QWs with different indium composition as a function of θ [20]. For InGaN/GaN heterostructure, P_{pz}^{InGaN} is dominant and ΔP_{tot} is almost not changed with the addition of spontaneous polarization. There are two crossovers for ΔP_{tot} at θ=45° and θ=90°, which are almost not influenced by the indium composition. The magnitude of polarization is compared for several common planes as follows: *c*-plane (0001) > $(10\bar{1}\bar{1})$ > $(20\bar{2}1)$ ≈ $(20\bar{2}\bar{1})$ > $(11\bar{2}2)$.

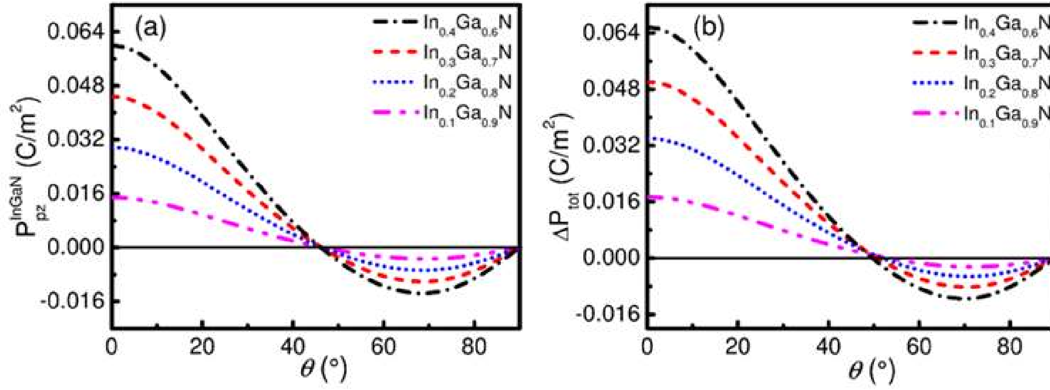

Fig. 6. (a) P_{pz}^{InGaN} and (b) ΔP_{tot} as a function of θ for InGaN/GaN heterostructure with In compositions from 10% to 40% [20].

For *c*-plane III-nitride QW based optoelectronic devices such as InGaN LEDs, strong polarization-induced electric field exists inside the QW, resulting in significant energy band tilting, a phenomenon known as quantum confined Stark effect (QCSE) [22]. As shown in Fig. 7(a), the tilted band diagram decreases the electron and hole's wavefunction overlap, which will reduce the efficiency of LEDs. In contrast, nonpolar or semipolar InGaN QWs have eliminated or reduced QCSE (Fig. 7(b)), which leads to a flatter QW profile and larger wavefunction overlap.

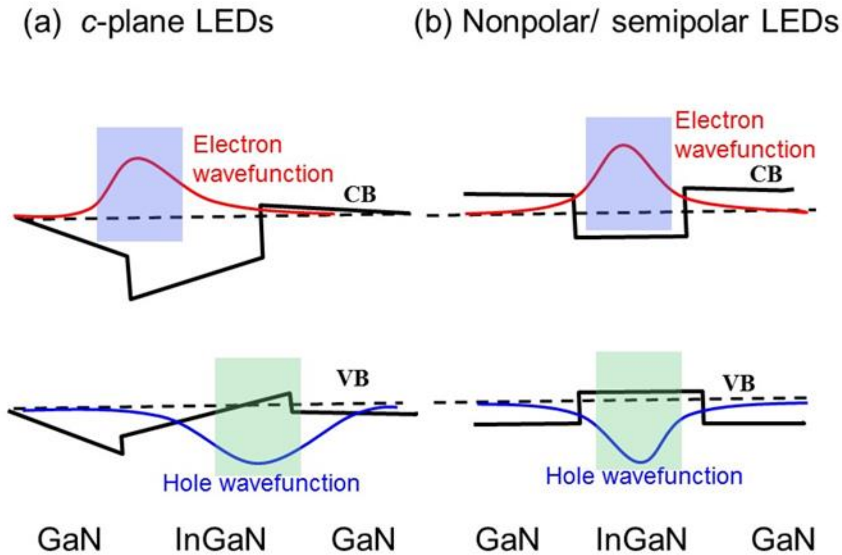

Fig. 7. Schematic band diagram and electron and hole wavefunctions of (a) *c*-plane and (b) nonpolar/semipolar InGaN LEDs.

1.4 Growth of Bulk Substrate

Homoepitaxial growth of devices on bulk GaN substrates are usually highly desired since it can significantly reduce material defect densities and improve device performance. Due to the commercial availability of bulk GaN substrates, currently the majority of high performance nonpolar and semipolar LEDs and vertical GaN power electronics are homoepitaxially grown on bulk substrates. The most commonly used growth methods are hydride vapor phase epitaxy (HVPE) [23] and ammonothermal growth [24]. The commercialized 2-inch *c*-plane bulk GaN substrates have low defect densities on the order of 10^6 cm^{-2} or less. Bulk substrates are relatively expensive for mass-production for now. But advancements in growth methods are continuing to drive down the wafer price and 4-inch wafers are under development. After obtaining thick *c*-

plane GaN boule, semipolar and nonpolar bulk GaN substrates can be produced by slicing the boule via a wire saw at a specific angle that corresponds to that plane.

1.5 Efficiency Droop in InGaN LEDs

Commercially available InGaN LEDs are usually grown on the conventional *c*-plane substrate and suffer from reduced efficiency with increasing current density, a phenomenon known as "efficiency droop" [25]. Figure 8 shows the internal quantum efficiency (IQE) as a function of injected current density [19]. When the current increases beyond ~ 10 A/cm^2, IQE drops dramatically. The efficiency droop of a InGaN LEDs is defined as [26]

$$\text{Droop} = (\text{IQE}_{\text{Max}} - \text{IQE}_{\text{J}})/\ \text{IQE}_{\text{Max}} \times 100\% \qquad (3)$$

where the IQE_{Max} and IQE_{J} represent the IQE maximum and the IQE at a given current density *J*.

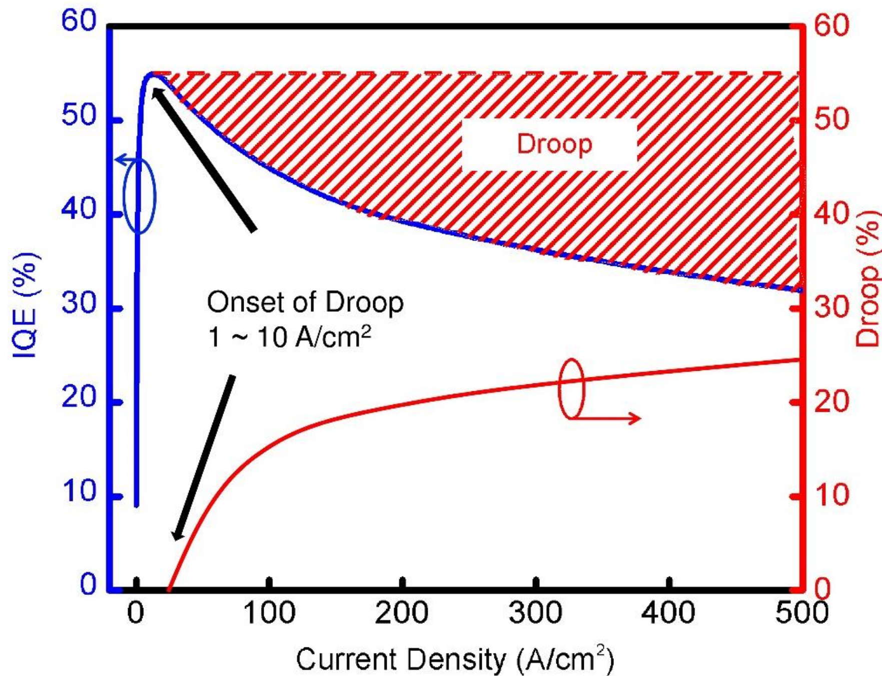

Fig. 8. IQE and efficiency droop vs. current density for a typical *c*-plane InGaN LED.

The widely used model for the droop characteristic of InGaN LEDs is the so-called *ABC* model, a carrier rate equation (Eqs. (4) and (5)) with *A, B,* and *C* coefficients, where *A*, *B*, and *C* are Shockley-Read-Hall (SRH), radiative, and Auger coefficients, respectively [27].

$$J = qd\,(An+Bn^2+Cn^3) \quad (4)$$

$$IQE = Bn^2/(An+Bn^2+Cn^3) \quad (5)$$

where q is the charge of electron, n is the carrier density, and d is the active region thickness.

The origin of efficiency droop is a highly controversial topic and people proposed many mechanisms including Auger recombination [28], [29], carrier leakage [25], [30], effective active region [31], carrier delocalization [32], QCSE [22], and defects [33], etc. The two most popular mechanisms are Auger recombination and carrier leakage. In an Auger recombination process, the energy due to the electron-hole pairs (e-h) recombination is absorbed by another electron (*eeh* process) or hole (*hhe* process), which is then excited to a higher energy level. Because this process doesn't give off photons, it is a non-radiative recombination pathway. The main supporting findings for the Auger recombination mechanism are: (1) As shown in the *ABC* model, Auger recombination is proportional to the cube of carrier density. So, it plays the major role at high current densities where the droop occurs. (2) The Auger coefficient is large enough to lead to efficiency droop when taking both direct and indirect Auger recombination processes into consideration [34]; (3) Researchers have experimentally observed Auger electrons in InGaN LEDs and correlated them with the efficiency droop [29]. Carrier leakage refers a process where some electrons escape from the active region of InGaN

LEDs and nonradiatively recombines with holes [25]. Due to the Fermi-Dirac distribution, there are always some energetic electrons that can fly over the barrier of the active region and contributes to efficiency droop. People have directly observed carrier leakage in InGaN LEDs, and proposed *ABC + f(n)* model to simulate the experimental data [35].

In addition, some other mechanisms also provided some insights into the efficiency droop of InGaN LEDs. The first one is the effective active region volume. Due to the poor hole injection, indium fluctuation and polarization-induced additional barriers, the effective active region volume should be smaller than the physical active region volume [31]. The second one is carrier delocalization. The spontaneous emission in InGaN LEDs is mainly from the carrier recombination in localized states [36]. These localized states can prevent carrier from participating nonradiative recombination processes. If carrier delocalization occurs, the nonradiative recombination will become stronger and can result in efficiency droop [32]. David *et al.* [37] performed differential carrier lifetime analysis and investigated the phase-space filling (PSF) effect on efficiency droop. They proposed a modified *ABC* model with the PSF effect to simulate the efficiency droop of the InGaN LEDs. More details will be discussed in Section 2.

1.6 Work synopsis

In the rest of this work, I will first discuss the efficiency droop in InGaN based blue LEDs and low-droop performance of semipolar LEDs in Section 2. Physical explanations will be provided, and modified *ABC* model will be applied to simulate the efficiency curves. In Section 3, the polarization effects on The ISBT properties of AlGaN/GaN QW will be studied. And we identify proper crystal orientations for THz and

FIR devices. Structure designs such as quantum well thickness, barrier thickness and barrier Al composition will also be discussed. The remaining two sections switch gear to III-nitride based power electronics. In Section 4, I will demonstrate the effect of buffer layer thickness on the vertical GaN-on-GaN p-n diodes and Schottky diodes. It's shown that thick buffer layer is beneficial to achieving high breakdown voltages. In Section 5, ultra-low turn-on voltage and on-resistance GaN-on-GaN Schottky diodes are reported via double drift layer design. This design can balance the forward and reverse characteristics to provide optimal performances for power switching applications. In Section 6, we demonstrated an easy-to-implement hydrogen-plasma based edge termination technique and considerably enhanced the breakdown voltages. After the discussion about our current work, we propose several future research topics.

CHAPTER 2

LOW EFFICIENCY DROOP SEMIPOLAR LEDS AND THE MODIFIED *ABC* MODEL

To reduce the efficiency droop in *c*-plane InGaN LEDs, growing LED devices on novel nonpolar and semipolar planes has recently been proposed as a possible solution [26], [38], [39]. These planes can enable the growth of thick and flat QWs, which result in reduced carrier density in the active region and thus less efficiency droop. Because of the different physical properties and resulting carrier dynamics, the traditional *ABC* model (Eq. 4 and 5) was not able to properly describe the droop characteristics of nonpolar/semipolar LEDs [40], even although it was suitable for *c*-plane LEDs. In this section, we study the phase space filling (PSF) effect on the modelling of semipolar InGaN LEDs. A much weaker PSF effect was found on semipolar LEDs possibly due to the lower carrier density.

2.1 Modified *ABC* Model

In the modified *ABC* model with the PSF effect, the current density J and IQE can be rewritten as [37]

$$J = qd\,(An+Bn^2/(1+n/n_0)+Cn^3/(1+n/n_0)) \quad (6)$$

$$IQE = Bn^2/(1+n/n_0)/[\,An+Bn^2/(1+n/n_0)+Cn^3/(1+n/n_0)] \quad (7)$$

where n_0 is the PSF coefficient, and $B/(1+n/n_0)$ and $C/(1+n/n_0)$ are radiative and Auger coefficients with PSF effect. A larger n_0 indicates a weaker PSF effect, and a smaller n_0 indicates a stronger PSF effect. Physically, PSF effect derives from the fact that at high current density carrier distribution should be described by Fermi-distribution instead of

Boltzmann distribution due to the Pauli Exclusion Principle [41]. Here, we simulated the IQE curves of InGaN LEDs with different n_0, A, B, C coefficients and d [42].

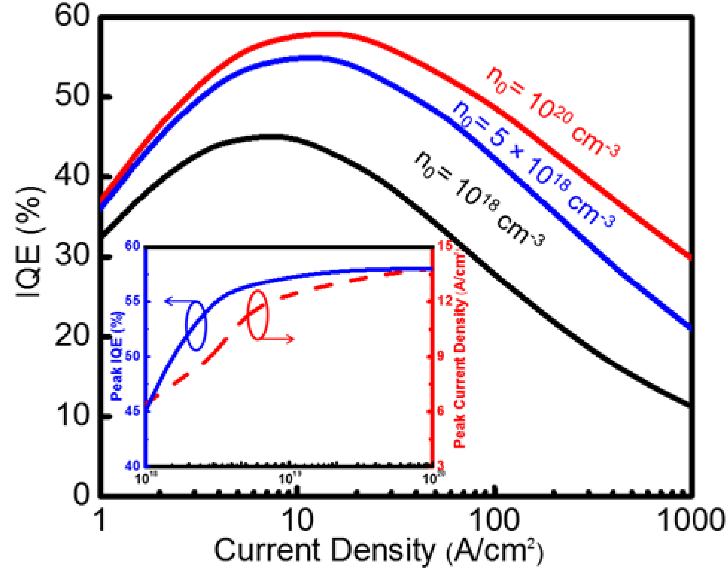

Fig. 9. Calculated IQE curves vs. current density with different n_0. The inset shows the peak IQEs and peak current densities as a function of n_0.

Table 1 Droop ratio (%) of IQE curves with different n_0 at different current densities.

n_0 /cm^3	100 A/cm^2	200 A/cm^2	300 A/cm^2	400 A/cm^2
10^{18}	38.4	51.1	58.2	62.4
5×10^{18}	23.1	35.1	43.6	47.0
10^{20}	15.5	25.0	31.5	35.3

Figure 9 shows IQE curves as a function of current densities varying different coefficients. The A, B, C and d values used in the calculations are 1×10^7 s^{-1}, 2×10^{-11} cm^3·s^{-1}, 5×10^{-30} cm^6·s^{-1} and 12 nm, respectively. These are reasonable values based on current InGaN LEDs technology. We can see that n_0 strongly impacts both the peak IQE and the efficiency droop of the LEDs. A weaker PSF effect (larger n_0) leads to a higher

IQE at all current densities. The peak IQE and peak current density first increase with increasing n_0 and then saturate at around n_0= 10^{20} cm^{-3}. When n_0 exceeds 10^{20} cm^{-3}, PSF effect shows almost no impact on device performance. This is possibly because PSF effect only comes into play when n_0 is comparable to n. When n_0 is larger than 10^{20} cm^{-3}, n/n_0 << 1 and therefore the PSF effect is minimal. According to Table 1, when n_0 increases and the PSF effect becomes weaker, the droop ratio decreases significantly, especially at high current density. These results indicate that the PSF effects can play a critical role in the efficiency droop of InGaN LEDs.

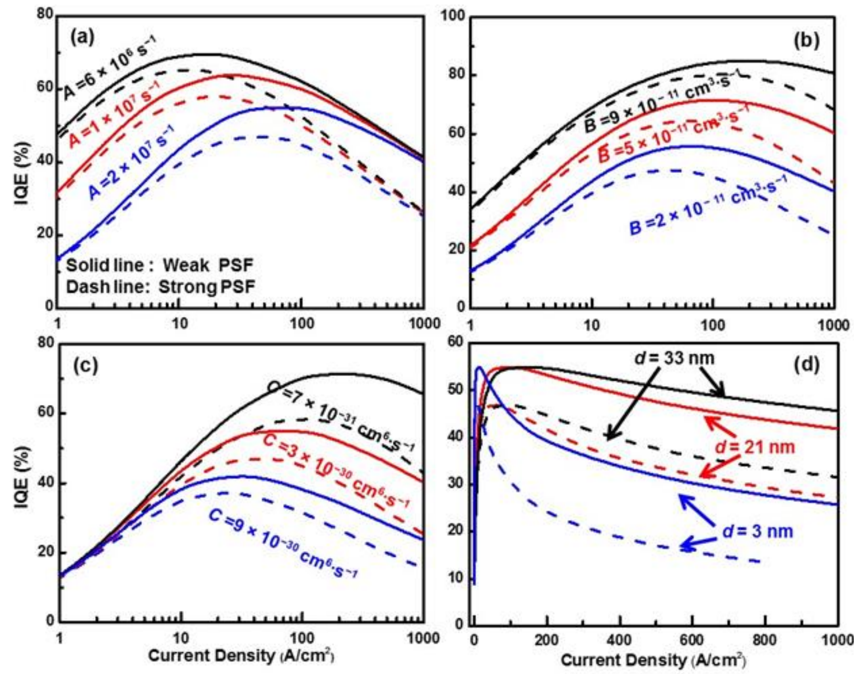

Fig. 10. Calculated IQE curves vs. current density with weak PSF effect (solid line, n_0 = 5× 10^{19} cm^{-3}) and strong PSF effect (dash line, n_0 = 3× 10^{18} cm^{-3}) varying (a) A (b) B (c) C and (d) d.

Figures 10(a)-10(c) present IQE curve versus current density with different A, B, and C coefficients under both strong and weak PSF effects. In Fig. 10(a), IQE curve is

calculated with various A coefficients while B (2×10^{-11} $cm^3 \cdot s^{-1}$) and C (3×10^{-30} $cm^6 \cdot s^{-1}$) and d (18 nm) are kept the same. Strong PSF effect reduces IQE and leads to smaller peak IQE and peak current density. In addition, the IQE difference under strong and weak PSF effect is particularly prominent at high current density. Similar trends were also observed in Figs. 10(b) and 10(c). Figure 10(d) demonstrates IQE versus current density with different active region thickness. The A B and C coefficients used are 2×10^7 s^{-1}, 2×10^{-11} $cm^3 \cdot s^{-1}$, 3×10^{-30} $cm^6 \cdot s^{-1}$, respectively. d is set as 3 nm (1 set of QWs), 21 nm (7 sets of QWs) and 33 nm (11 sets of QWs), respectively. An increasing active region thickness will effectively reduce the efficiency droop. This could be one of theoretical evidence for the advantages of growing thick QW on nonpolar/semipolar LEDs. At the same d, strong PSF effect will result in a significantly reduced IQE.

2.2 Carrier Lifetime Study

The emission properties of semipolar $(20\bar{2}\bar{1})$ LEDs were investigated using time-resolved photoluminescence (TRPL) and steady-state PL measurement [43]. We found out that the carrier lifetime of semipolar $(20\bar{2}\bar{1})$ InGaN LED is much smaller than that of the *c*-plane LED. This indicates a reduced excess carrier density in semipolar $(20\bar{2}\bar{1})$ LEDs. The smaller radiative carrier lifetime is expected due to the large electron and hole wavefunction overlap in semipolar LEDs, which can increase the efficiency as well as reduce efficiency droop.

Semipolar $(20\bar{2}\bar{1})$ LEDs were grown by metalorganic chemical vapor deposition (MOCVD) on bulk GaN substrates. The device structure is comprised of 1μm Si-doped *n*-type GaN layer, an InGaN active region, a 20 nm *p*-type Mg-doped $Al_{0.15}Ga_{0.85}N$ electron blocking layer (EBL), and a 60 nm *p*-type GaN layer. Two active layer structures

were grown: the 3 periods of InGaN (3 nm) / GaN (20 nm) multiple QWs (MQWs), and the 12 nm single QW (SQW). For reference, *c*-plane LED LEDs with the same structure also grown. Please be noted 12 nm InGaN LEDs were not grown for *c*-plane LEDs due to the excessively large QCSE and expected low device performance. These LEDs have various wavelengths and comparable light output power.

TRPL measurements were carried out using a time-correlated single photon counting (TCSPC) system at room temperature (300K) with a resolution of ~20 ps. The light source is an ultrafast titanium-sapphire laser with a 130-fs pulse duration. The 780 nm output is sent to a pulse selector to obtain pulses at a repetition rate of 4 MHz. The pulsed light then goes through a frequency doubler to get 390 nm output light which then incidents on the LEDs. The single photon counting is done by a monochromator which is set at the peak PL wavelength of the samples and a high-speed microchannel plate PMT detector. The laser power is set at a low power of ~ 0.1 mW not to affect the internal electric field of the LEDs. The PL measurements were performed using 405 nm laser diode and a spectrometer equipped with a photomultiplier under temperatures of 300K, 200K, and 10K. It should be noted that the discussed wavelengths below indicate PL peak wavelengths of the LEDs.

Figure 11 presents the TRPL measurements of semipolar $(20\overline{2}\overline{1})$ and *c*-plane LEDs. The carrier decay dynamics was simulated using an exponential fitting: $\Delta n = \Delta n_0 \exp(-t/\tau)$, where Δn is the excess carrier density, Δn_0 is the photogenerated carrier density and τ is the minority carrier lifetime. The carrier lifetime was 0.47 ns for semipolar $(20\overline{2}\overline{1})$ LEDs, and 3.3 ns for *c*-plane LEDs. The dominate decay process is possibly associated with the localized exciton emission [36], [44]. Table 2 summaries τ of

semipolar ($20\bar{2}\bar{1}$) and *c*-plane LEDs with different wavelength and active layer structures. It's obvious that the semipolar ($20\bar{2}\bar{1}$) LEDs had much smaller τ than *c*-plane LEDs.

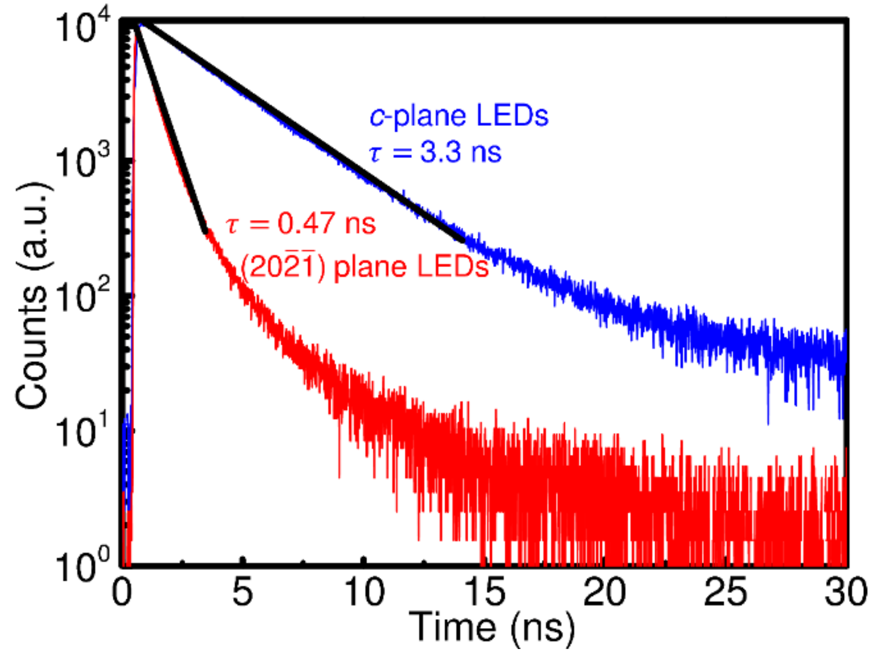

Fig. 11. TRPL spectra of semipolar ($20\bar{2}\bar{1}$) and *c*-plane LEDs.

Table 2. Carrier lifetime of semipolar ($20\bar{2}\bar{1}$) and *c*-plane LEDs.

Plane	Active region	Wavelength (nm)	τ (ns)
($20\bar{2}\bar{1}$)	12nm SQW	436	0.47
($20\bar{2}\bar{1}$)	12nm SQW	405	0.67
($20\bar{2}\bar{1}$)	3 × 3 nm MQW	452	1.36
($20\bar{2}\bar{1}$)	3 × 3 nm MQW	444	1.70
c-plane	3 × 3 nm MQW	500	3.67
c-plane	3 × 3 nm MQW	455	3.30
c-plane	3 × 3 nm MQW	433	2.80

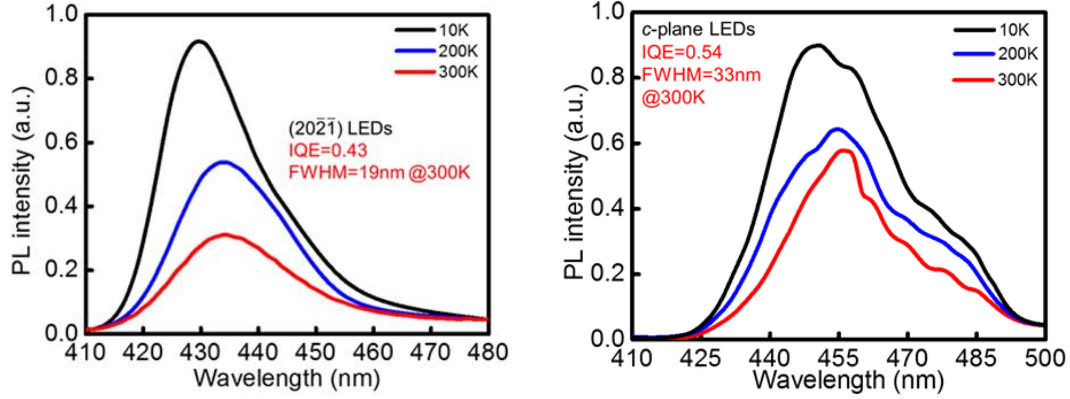

Fig. 12. PL spectra of (left) semipolar (20$\bar{2}\bar{1}$) and (right) *c*-plane LEDs at 10K, 200K and 300K.

The measured lifetime τ is can be further decomposed into radiative recombination lifetime τ_{rad} and nonradiative recombination lifetime τ_{nonrad} using $1/\tau = 1/\tau_{rad} + 1/\tau_{nonrad}$. Using temperature-dependent PL measurements, $\eta_{300K/10K} = \tau_{nonrad}/(\tau_{nonrad} + \tau_{rad})$, where $\eta_{300K/10K}$ is the ratio of integrated PL intensity of 300K to that of 10K, which is also called IQE. At very low temperature, the nonradiative recombination centers are assumed to be frozen and the nonradiative lifetime is infinite, leading to IQE = 1 at 10K [45], [46]. Figures 12(a) and 12(b) present the temperature-dependent PL results of above semipolar (20$\bar{2}\bar{1}$) and *c*-plane LEDs under 300K, 200K, and 10K, respectively. Table 3 summarizes the obtained IQE, τ_{nonrad}, and τ_{rad} for two semipolar (20$\bar{2}\bar{1}$) LEDs and one *c*-plane LED. Semipolar LEDs had smaller τ_{rad} and τ_{nonrad} than *c*-plane LEDs. Smaller τ_{rad} can increase IQE and decrease efficiency droop. Although smaller τ_{nonrad} may result in low IQE, it can also reduce efficiency droop. The smaller τ_{rad} of semipolar LEDs is attributed to small QCSE and large electron and hole's wavefunction overlap, therefore increasing the recombination rate and decreasing the radiative lifetime. The smaller τ_{nonrad} on semipolar (20$\bar{2}\bar{1}$) samples is possibly due to

the smaller indium fluctuation, which results in more carriers trapped in nonradiative recombination centers. This is confirmed by the smaller full width at half maximum (FWHM) of the semipolar LEDs [47].

Table 3. The IQE, τ_{rad}, and τ_{nonrad} of $(20\bar{2}\bar{1})$ and *c*-plane InGaN LEDs.

Sample	Wavelength (nm)	IQE ($\eta_{300K/10K}$)	τ_{rad} (ns)	τ_{nonrad} (ns)
$(20\bar{2}\bar{1})$ 12 nm SQW	436	0.43	1.0	0.8
$(20\bar{2}\bar{1})$ 3 × 3 nm MQW	444	0.53	3.2	3.6
c-plane 3 × 3 nm MQW	455	0.54	6.4	7.2

2.3 Simulation Results

Figure 13 presents the fitting results of semipolar and *c*-plane LEDs using modified *ABC* model with PSF effect. The light extraction efficiency (η_{extr}) is reasonable with current technology status, and the injection efficiency is assumed to be 100% for all three LEDs. A very good agreement between experimental data and the theoretical modeling was obtained for semipolar LED [47] using weak PSF effect (n_0=5.0×10^{19} cm^{-3}) and two *c*-plane LEDs [48], [49] using strong PSF effect (n_0=1.0×10^{18} cm^{-3} or 6.0×10^{18} cm^{-3}). Table 4 lists the fitting parameters of modified *ABC* model for other *c*-plane and semipolar LEDs. By comparison, we can see that n_0 of semipolar LEDs are larger than that of *c*-plane LEDs. Large n_0 must be used in the fitting of semipolar LEDs. This indicates that weak PSF effect may exists in semipolar LEDs which leads to the low efficiency droop.

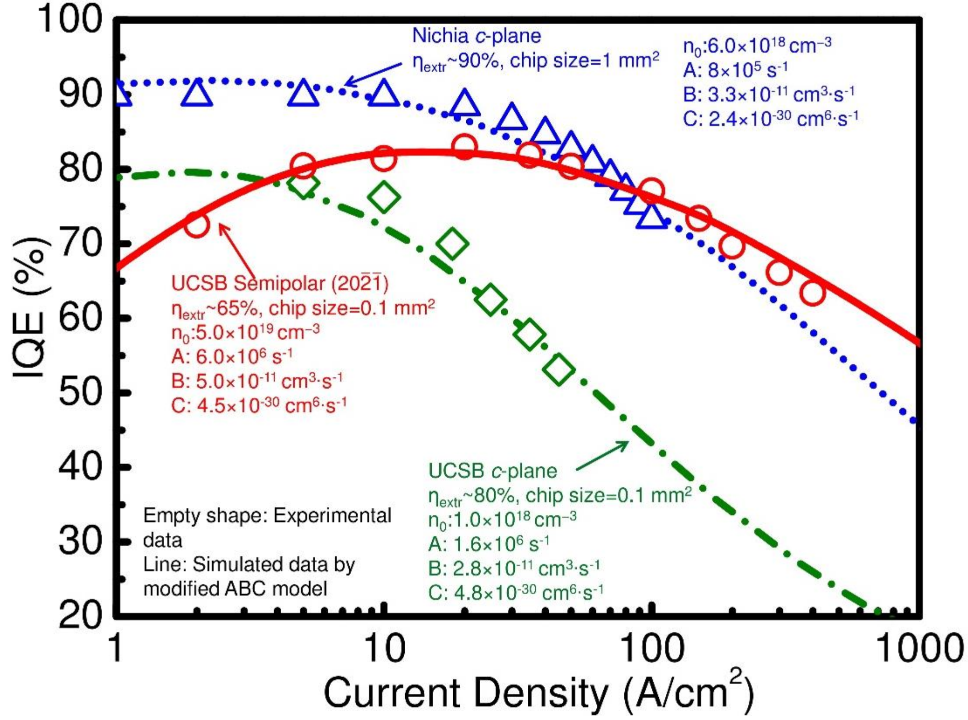

Fig. 13. Simulated IQE curves for reported semipolar $(20\bar{2}\bar{1})$ LEDs [47], Nicha *c*-plane LEDs [49] and UCSB *c*-plane LEDs [48].

Table 4. *A*, *B*, *C*, *d* and n_0 coefficients used in modified *ABC* model for both *c*-plane and semipolar InGaN LEDs.

Planes	$A\times10^{-7}$ (s^{-1})	$B\times10^{11}$ ($cm^3\ s^{-1}$)	$C\times10^{30}$ ($cm^6\ s^{-1}$)	d (nm)	$n_0\times10^{-19}$ (cm^{-3})
c[48]	0.16	2.8	4.8	15	0.10
c[49]	0.08	3.3	2.4	12	0.60
$(30\bar{3}\bar{1})$[39]	1.2	4.5	6.0	15	3.0
$(20\bar{2}\bar{1})$[47]	0.6	5.0	4.5	12	5.0

CHAPTER 3

INTERSUBBAND TRANSITION IN SEMIPOLAR ALGAN/GAN QUANTUM WELL AND THE CRYSTAL ORIENTATION EFFECTS

Currently, III-nitride ISBT devices are mainly grown on polar *c*-plane substrates with titled QW, limiting their access to THz or FIR regime. In addition, it is also challenging to grow ISBT devices on polarization-free nonpolar *m*-plane due to stacking faults and alloy inhomogeneity [50]-[52]. We proposed using semipolar planes to realize high performance ISBT devices due to their high material epitaxial quality and weak polarization properties [53], [54]. In this Section, we comprehensively investigated the effects of crystal orientation, QW thickness, barrier thickness and barrier Al composition on ISBT properties of AlGaN/GaN SQW [53]. It's found out that nonpolar and certain semipolar planes ($55° < \theta < 90°$) have the optimal performance for THz ISBT devices with high absorption quantum efficiency. Semipolar SQW ISBT can access sub-10THz and FIR wavelength by increasing QW thickness.

3.1 Simulation Method

A commercial software SiLENSe was used to calculate the QW bandstructures and subband wavefunctions [55], where one-dimensional Schrödinger-Poisson equation is solved self-consistently with drift-diffusion model included. The software has accounted for strain and polarization effects on arbitrary crystal orientations of III-nitride. For AlGaN/GaN heterostructure, the calculation process of polarization of any crystal orientation is similar to Eq. 1 and 2. More details about the polarization calculation can be found in Ref. [21]. Table 5 summaries material parameters used in the SiLENSe

software. After obtaining device parameters from the software, all the data was plugged into the Matlab code to do the absorption calculation as shown in the following.

In a photodetector, the absorption coefficient $\alpha(\lambda)$ between the first and the second subbands can be expressed as [56]

$$\alpha(\lambda)=\frac{8\pi^3c^2\mu}{\lambda n_r L}\sin^2\delta|M_{12}|^2\frac{m^*kT}{\pi h^2}\ln\left\{\frac{1+\exp[(E_f-E_1)/kT]}{1+\exp[(E_f-E_2)/kT]}\right\}\frac{h/(2\pi\tau)}{(E_2-E_1-hc/\lambda)^2+[h/(2\pi\lambda)]^2} \quad (8)$$

where c is the speed of light in vacuum, μ is the permeability, λ is wavelength of incident light, n_r is refractive index, L is the QW thickness, δ is the light propagation angle (usually 45° is used [16]), M_{12} is the dipole matrix element of first two subbands, m^* is the effect mass, k is the Boltzmann constant, T is the operation temperature, h is the Planck constant, E_f is the Fermi energy, E_1 is the energy of the first subband, E_2 is the energy of the second subband and τ is the relaxation time. The AlGaN barrier is unintentionally doped with a carrier concentration of 10^{15} cm^{-3} and the QW is doped in a way to maximize the background limited infrared performance temperature [16]. The other parameters used in this work can also be found in Ref. [16]. M_{12} is given by

$$M_{12} = q\int_{-\infty}^{\infty}\psi_2^*(z)z\psi_1(z)dz \quad (9)$$

where z is the along the device growth direction, ψ_1 is wavefuction of the first subband and ψ_2 is the wavefunction of the second subband.

Table 5 Material parameters used in SiLENSe.

Material parameter	Unit	AlN	GaN
Elastic constant C_{11}	GPa	395	375
Elastic constant C_{12}	GPa	140	140
Elastic constant C_{13}	GPa	115	105

Elastic constant C_{33}	GPa	385	395
Elastic constant C_{44}	GPa	120	100
Piezoelectric coefficient e_{15}	C/cm^2	-0.48	-0.27
Piezoelectric coefficient e_{31}	C/cm^2	-0.58	-0.33
Piezoelectric coefficient e_{33}	C/cm^2	1.55	0.65
P_{sp}	C/cm^2	-0.081	-0.029
Donor ionization energy	meV	13	13
Acceptor ionization energy	meV	470	170
Lattice constant *a*	nm	0.3112	0.3188
Lattice constant *c*	nm	0.4982	0.5186
Energy bandgap	eV	6.25	3.51
Varshni parameter a	meV/K	1.80	0.91
Varshni parameter b	K	1462	830
Crystal-field splitting	meV	-93	22
Spin-orbital splitting	meV	11	11
Electron affinity	eV	0	1.96
Dielectric constant	-	8.5	8.9
Electron effective mass along axis *a*	m_0	0.26	0.2
Electron effective mass along axis *c*	m_0	0.25	0.2
Heavy hole effective mass along axis *a*	m_0	2.58	1.65
Heavy hole effective mass along axis *a*	m_0	1.95	1.1

3.2 Effect of Crystal Orientation

The simulated structure was 25 nm $Al_{0.3}Ga_{0.7}N$ / 5 nm GaN/ 25 nm $Al_{0.3}Ga_{0.7}N$ SQW. As shown in Fig. 14. polar *c*-plane (θ=0°) and semipolar $(10\bar{1}3)$ (θ = 32°) SQW

show tilted bandstructures, while *m*-plane ($\theta = 90°$) and semipolar $(20\bar{2}1)$ ($\theta = 75°$) have relatively flat profiles. The titled band profile can separate ψ_1 and ψ_2 in terms of energy and position, which will influence M_{12}, ISBT frequency and absorption coefficients.

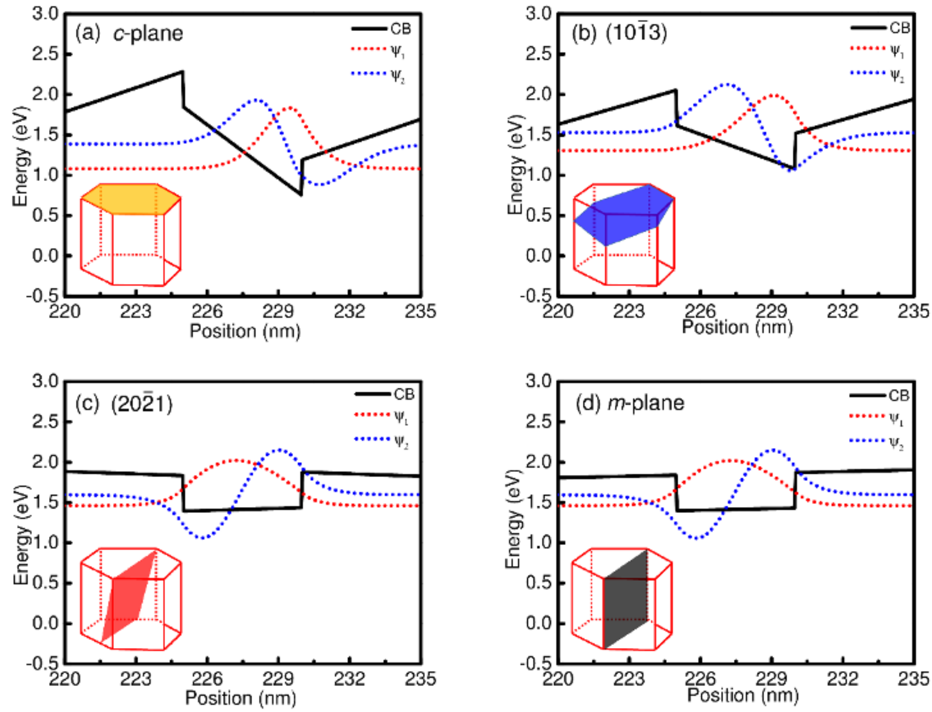

Fig. 14. Conduction band (CB) of AlGaN/GaN SQW on (a) *c*-plane, (b) $(10\bar{1}3)$, (c) $(20\bar{2}1)$, and (d) *m*-plane.

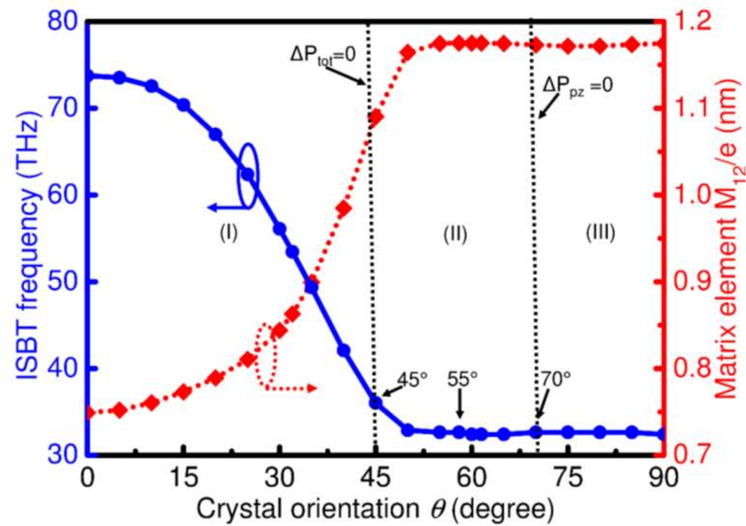

Fig. 15. ISBT frequency and M_{12}/e of AlGaN/GaN SQW vs. crystal orientations.

Figure 15 presents ISBT frequencies and matrix elements for various crystal orientations. The transition frequency is calculated by $(E_2 - E_1)/h$. Please be noted that the "pair" semipolar planes with different polarity [e.g., $(20\bar{2}1)$ at 75° and $(20\bar{2}\bar{1})$ at 105°] have almost identical ISBT properties, which is not shown here. ISBT frequency decreases monotonically with θ from 0° to 55°; and it becomes stable when $\theta > 55°$. This trend can be explained by the polarization effects of III-nitride. With weaker polarizations, QW profile is flatter and the wavefuctions of subbands are less separated, leading to a smaller transition frequency. All the semipolar planes can be divided into three regions: in region I ($0° < \theta < 45°$) the ΔP_{pz} is the dominant effect; in region II ($45° < \theta < 70°$), ΔP_{pz} and ΔP_{sp} are both important; in region III ($70° < \theta < 90°$), $\Delta P_{tot} \approx 0$. Although the crossover of ΔP_{tot} happens at θ=70°, ΔP_{tot} is already small enough when $\theta > 55°$and has negligible effects on QW profile. For THz applications, nonpolar and semipolar planes with $\theta > 55°$ are preferable. In addition, an opposite trend was also observed for the dipole matrix elements. Semipolar structures with $\theta > 55°$ have very large matrix elements and possibly high absorption coefficients.

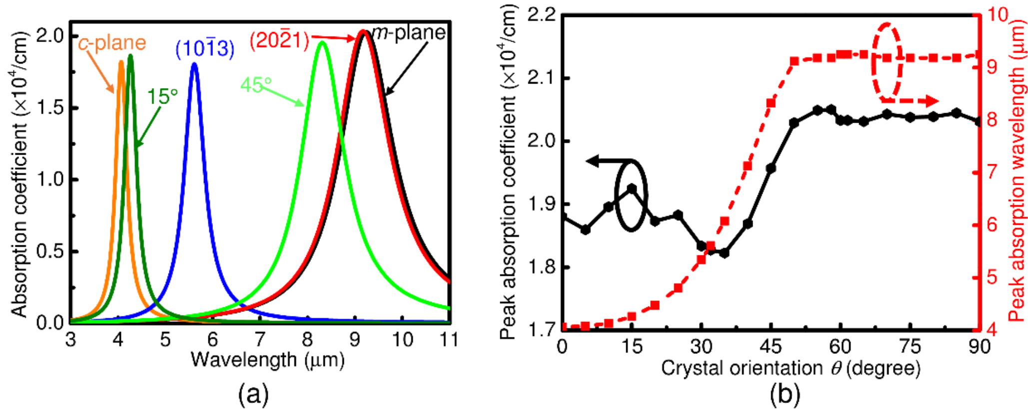

Fig. 16. (a) Absorption spectra for AlGaN/GaN SQW on various crystal orientations. (b) Peak absorption coefficient and peak absorption wavelength vs. crystal orientation.

In Fig. 16(a), with increasing θ, the spectra of semipolar planes are moving towards that of nonpolar *m*-plane. As shown in Fig. 16(b), the peak absorption wavelength increases with increasing θ when $0° < \theta < 55°$; both the parameters reached maxima when $\theta > 55°$. In terms of peak absorption coefficients, semipolar planes with $\theta > 55°$ show the highest absorption.

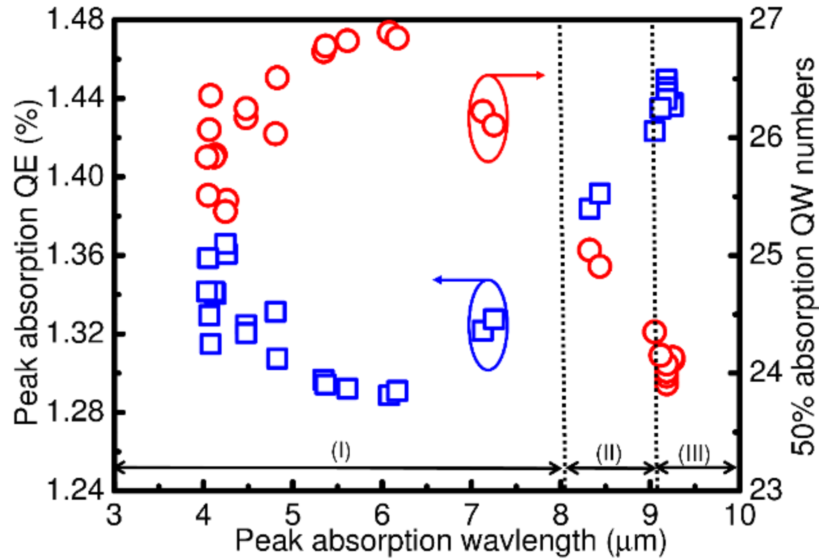

Fig. 17. Peak absorption QE and 50% absorption QW numbers vs. peak absorption wavelength.

For real device applications, it is important to evaluate the absorption quantum efficiency (QE), given by $\alpha(\lambda)L/\cos\gamma$ where $L/\cos\gamma$ is the light propagation length in devices [16]. Figure 17 shows that nonpolar and semipolar planes with $\theta > 55°$ can access longer wavelength and have higher peak absorption QE. In addition, it's also desired to grow less QWs in order to obtain good material qualities since the strain increases significantly with the number of QWs. The 50% absorption QW numbers is the QW

numbers when 50% of incident light are absorbed per round-trip, which is given by N= –ln(50%)/(peak absorption QE) [16]. Semipolar planes with θ > 55°) require few QWs to achieve 50% absorption. Therefore, QWs on nonpolar and semipolar planes (55° < θ < 90°) will deliver better performance at longer wavelength and have less stringent material requirements.

3.3 Effect of Quantum Well Thickness

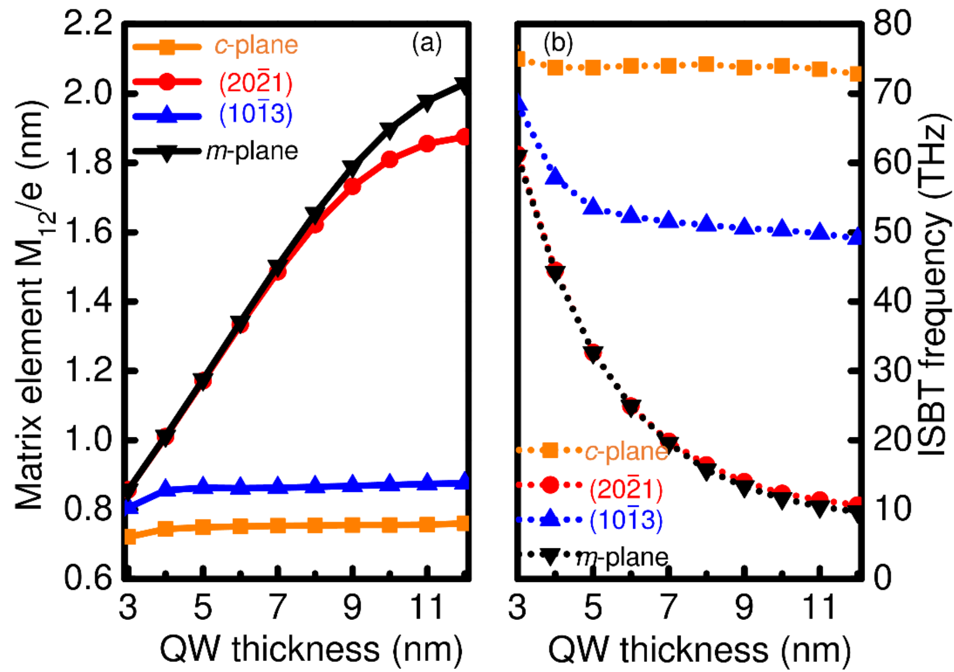

Fig. 18. (a) M_{12}/e and (b) ISBT frequency of AlGaN/GaN SQW vs. QW thickness.

The simulated SQW structure has a 25 nm $Al_{0.3}Ga_{0.7}N$ barrier and the thicknesses of QW is varied from 3 nm to 12 nm. As shown in Fig. 18, (20$\bar{2}$1) and *m*-plane SQW have lower transition frequency at a certain QW thickness compared with semipolar (10$\bar{1}$3) and *c*-plane SQW. In addition, with increasing QW thickness the transition frequency of (20$\bar{2}$1) SQW decreases. This is because in a relatively flat QW the energy separation of the subbands and transition frequency are inversely proportional to the well

thickness. In contrast, for $(10\bar{1}3)$ and *c*-plane SQW with strong polarization-related effects, the transition frequency first decreases with increasing QW thickness and then becomes stable. This is because the triangular potential well limits the separation of subband wavefuctions. Therefore, semipolar $(20\bar{2}1)$ SQW shows tunable ISB transition frequency and are capable of reaching sub-10 THz regime. In addition, both $(20\bar{2}1)$ and *m*-plane SQW have larger dipole matrix elements and thus higher absorption coefficient.

As shown in Fig. 19 (a), all the spectra of the *c*-plane SQW peak at a wavelength around 4 μm. For $(10\bar{1}3)$ SQW, most of the spectra are at a peak wavelength of 6 μm although the first two spectra are separated. In contrast, $(20\bar{2}1)$ SQW has much distributed absorption spectra along the wavelength range. At a QW thickness of 12 nm, the peak absorption wavelength is around 28 μm (FIR), indicating it can operate at FIR wavelength.

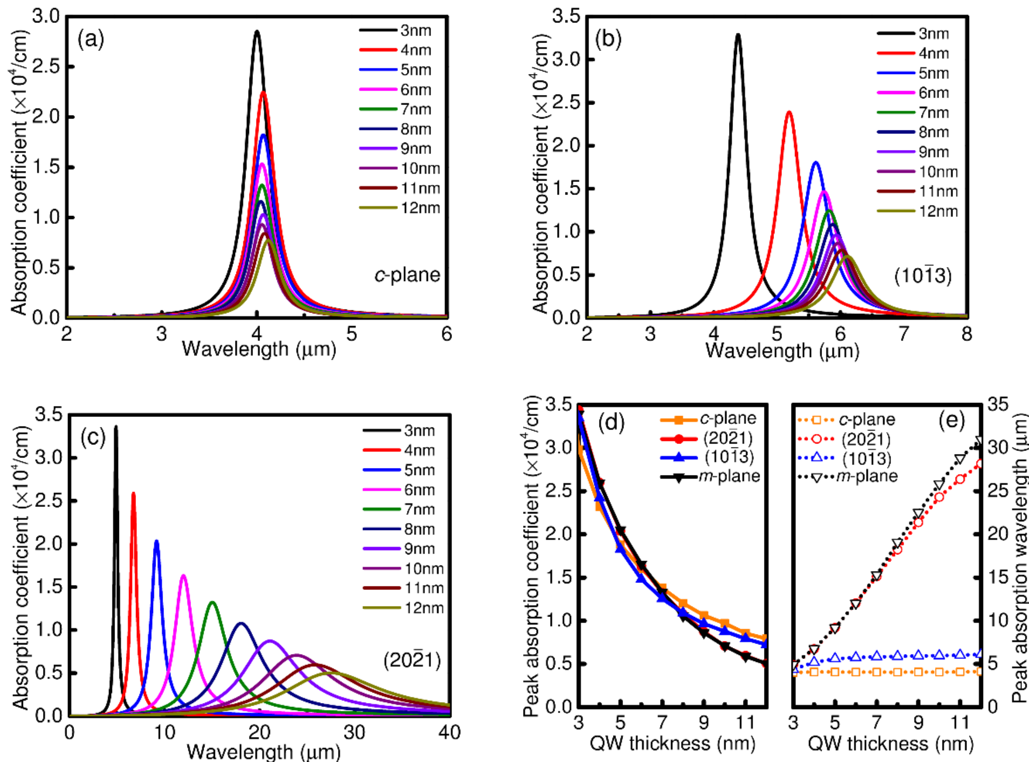

Fig. 19. Absorption spectra of (a) *c*-plane, (b) $(10\bar{1}3)$, (c) $(20\bar{2}1)$ AlGaN/GaN SQW varying QW thickness. (d) Peak absorption coefficient and (e) peak absorption wavelength vs. QW thickness.

3.4 Effect of Barrier Thickness

$Al_{0.3}Ga_{0.7}N$ / GaN (5 nm) SQW with barrier thickness varying from 5 nm to 25 nm were studied in Fig. 20. $(20\bar{2}1)$ and *m*-plane SQW don't show any decrease in transition frequency and dipole matrix elements with increasing barrier thickness. For $(10\bar{1}3)$ and *c*-plane SQW, the transition frequency increases dramatically with barrier thickness and the dipole matrix elements are largely reduced. Therefore semipolar $(20\bar{2}1)$ based ISBT devices could offer stable performance in terms of barrier thickness variation during device growth.

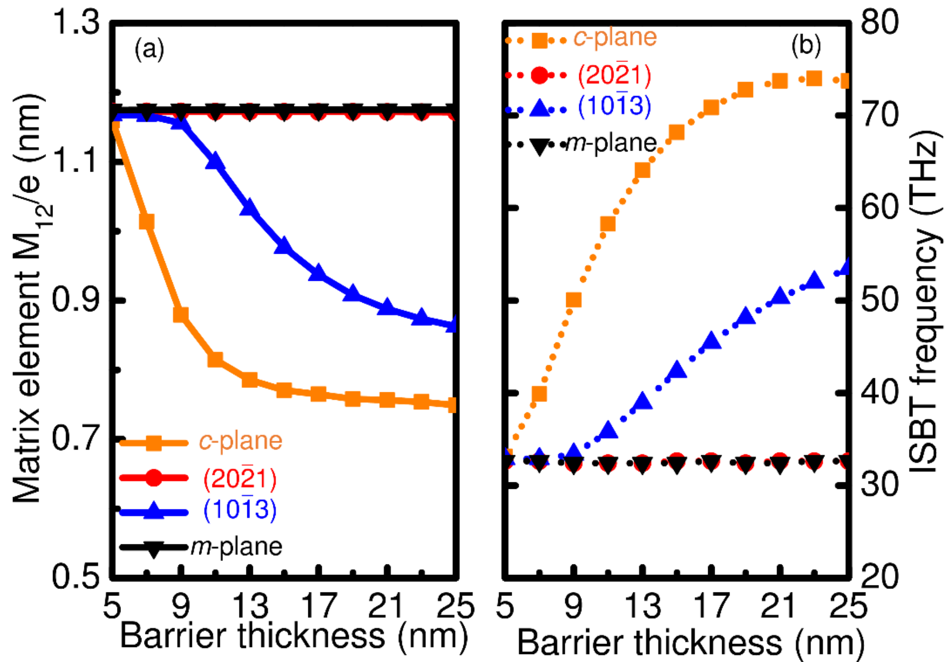

Fig. 20. (a) M_{12}/e and (b) ISBT frequency of AlGaN/GaN SQW vs. barrier thickness.

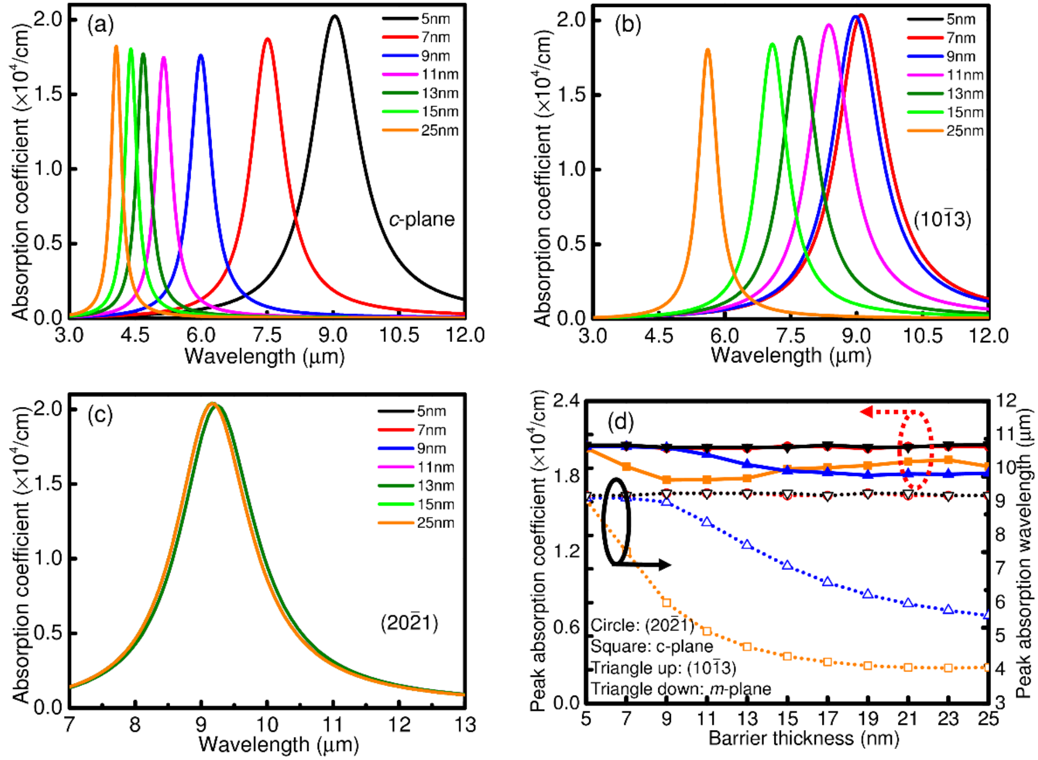

Fig. 21. Absorption spectra of (a) *c*-plane, (b) (10$\bar{1}$3), (c) (20$\bar{2}$1) AlGaN/GaN SQW varying barrier thickness. (d) Peak absorption coefficient and peak absorption wavelength vs. barrier thickness.

Almost all the spectra of (20$\bar{2}$1) SQW are overlapped at peak wavelength of 9 μm in Fig. 21 (c). For (10$\bar{1}$3) and *c*-plane SQW, their absorption spectra move towards much shorter wavelength with increasing barrier thickness. Furthermore, the decrease of peak absorption coefficients is also observed on (10$\bar{1}$3) and *c*-plane SQW. Therefore, thick barriers have minimum influence on (20$\bar{2}$1) and *m*-plane SQW, but adversely affect the device performance of (10$\bar{1}$3) and *c*-plane SQW.

Figure 22 explains the effect of barrier thickness on ISBT properties. The QW profile of *c*-plane and (10$\bar{1}$3) SQW gets more tilted with increasing barrier thickness, which further pushes the subband wavefuctions apart, resulting in increased ISBT

frequency and decreased dipole matrix elements. However, semipolar $(20\bar{2}1)$ and *m*-plane SQW don't show much change in QW profile when the barrier thickness is varied. With increasing barrier thickness, distances between polarization-induced charges in the QWs are changed. As a result, the electric field in the QW is increased and the electric field is the barrier is decreased [57], [58]. Therefore, a thicker barrier of *c*-plane and $(10\bar{1}3)$ SQW leads to more titling in QW. Due to small charge at the interface, $(20\bar{2}1)$ and *m*-plane are not affected by barrier thickness.

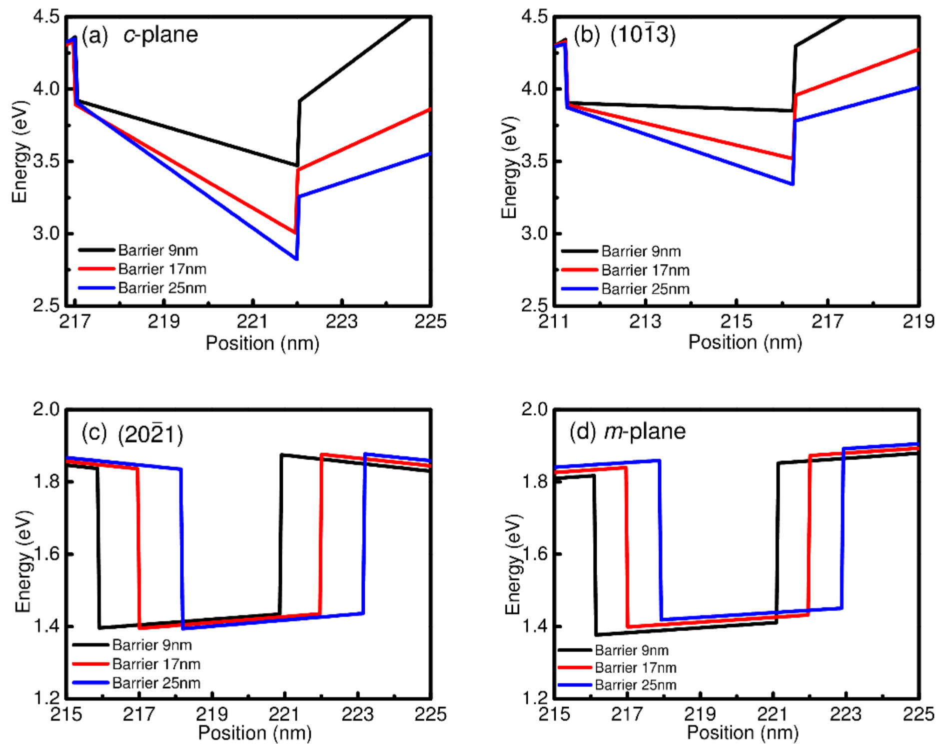

Fig. 22. CB of (a) *c*-plane, (b) $(10\bar{1}3)$, (c) $(20\bar{2}1)$, and (d) *m*-plane AlGaN/GaN SQW with different barrier thicknesses.

3.5 Effect of Barrier Al Composition

Figure 23 shows the effect of barrier Al composition on the ISBT properties. The Al composition next to the legends are the minimum Al composition required to have two

subbands in the QW. The transition frequencies of $(10\bar{1}3)$ and *c*-plane SQW experience a dramatic increase with increasing Al composition, while those of $(20\bar{2}1)$ and *m*-plane SQW are mostly stable. This is because high Al composition leads to strong polarizations and thus a titled QW profile. Furthermore, the dipole matrix elements and peak absorption wavelength on $(10\bar{1}3)$ and *c*-plane SQW are also reduced by high Al composition in the barrier. But the wavelength reduction is relative smaller for semipolar $(20\bar{2}1)$ SQW. And the peak absorption coefficients of $(20\bar{2}1)$ SQW remain constant with increasing Al composition. These results indicate semipolar $(20\bar{2}1)$ SQW behaves much better at high Al compositions.

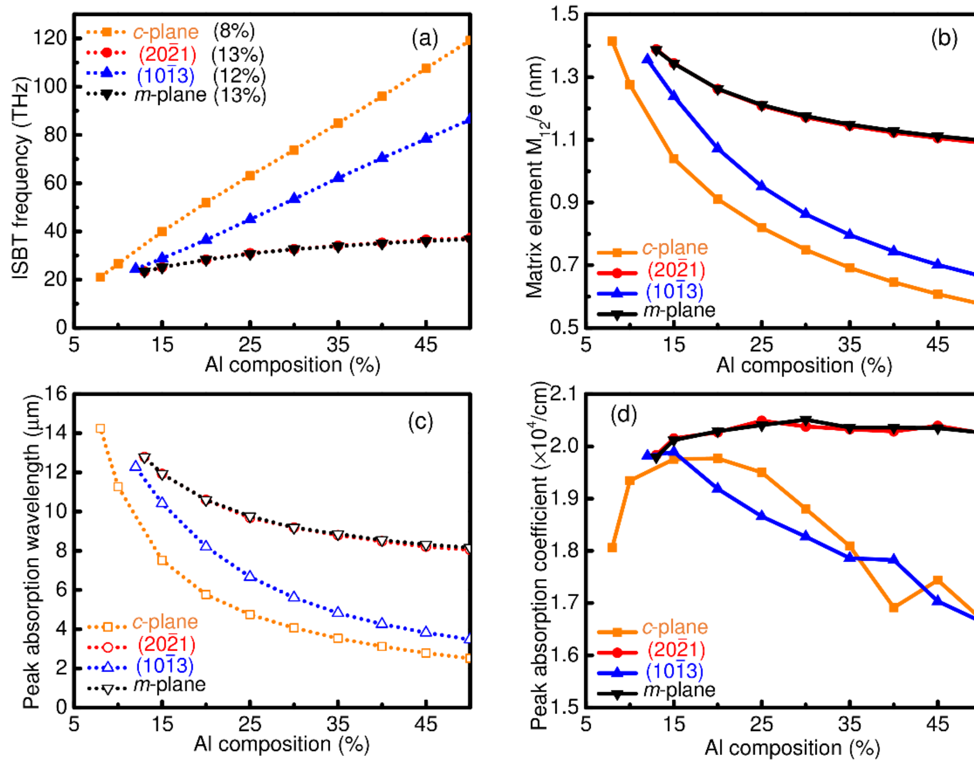

Fig. 23. (a) ISBT frequency and (b) M_{12}/e of AlGaN/GaN SQW vs. barrier Al composition. (c) Peak absorption wavelength and (d) peak absorption coefficient vs. barrier Al composition.

3.6 Summary

We studied the effect of crystal orientation, QW thickness, barrier thickness and barrier Al composition on the ISBT properties of AlGaN/GaN SQWs. Semipolar planes with θ between 55° and 90° show THz ISBT frequencies and long wavelength (FIR) responses. In addition, they have higher absorption coefficients and absorption quantum efficiency, require fewer QWs to absorb the same amount of incident light, and have tunable transition frequencies and absorption wavelengths when varying QW thickness. Semipolar $(20\bar{2}1)$ SQW also shows stable device performance when varying barrier thickness and Al composition. These results indicate semipolar planes with weak polarization are promising candidates for high performance THz and FIR optoelectronics.

CHAPTER 4

VERTICAL GAN-ON-GAN P-N AND SCHOTTKY POWER DIODES WITH DIFFERENT BUFFER LAYER THICKNESS

With large bandgap and large critical electrical field, GaN based power electronics has recently garnered significant attention for efficient power conversion applications. GaN-based power diodes such as SBDs and p-n diodes are an essential part of this power system. Conventional GaN power devices are usually grown on foreign substrates such as sapphire [59], [60] and Si [61]-[64]. However, the disadvantage is the high defect densities in the devices (> 10^9 cm^{-2}) due to the large lattice mismatch. These defects can serve as leakage pathways and significantly limit the potential of the GaN devices. Recently, bulk GaN substrates have enabled a wave of studies on the vertical GaN power diodes. The advantages are two-fold. First, the defect densities are considerably reduced (< 10^6 cm^{-2}). Second, the vertical structures can avoid surface-related issues and reduce chip size. Devices with promising performance such as high V_{BD} and low R_{on} [12], [13] have been demonstrated. Researchers have proposed various strategies to further enhance the breakdown voltage including low doping concentration, thicker drift layer, passivation and field plates. However, the effect of the buffer layer thickness has not yet been investigated. The conventional wisdom was that the buffer layer was not necessary for homoepitaxial growth. However, bulk GaN substrates still have a fair number of defects. In this work, we study the effect of the buffer layer on the electrical properties of vertical GaN-on-GaN p-n and SBDs [65]. And we found that buffer layer thickness does play an important role even in GaN homoepitaxial growth.

4.1 Material Growth by MOCVD

The device epilayer structures were grown by MOCVD on free-standing heavily-doped GaN substrates with a carrier concentration on the order of 10^{18} cm^{-3}. Trimethylgallium (TMGa) and ammonia (NH_3) were the sources for Ga and N, respectively. Silane (SiH_4) was the precursor for n-type Si dopants and Bis(cyclopentadienyl)magnesium (Cp_2Mg) was the precursor for p-type Mg dopants. The carrier gas was hydrogen (H_2). As shown in Fig. 24(a), it started with the growth of a Si-doped n$^+$-GaN buffer layer with a doping concentration of 2×10^{18} cm^{-3}. The buffer layer thickness was varied: 50 nm, 400 nm, 1 µm, and 1 µm for samples A, B, C, and D, respectively. Then a 9-µm-thick unintentionally doped (UID) or lightly doped ([Si] = 2×10^{16} cm^{-3} only for sample D) drift layer was grown, followed by a 500 nm p-GaN with a Mg doping concentration of 10^{19} cm^{-3}, and a 20 nm heavily doped p$^+$-GaN ohmic contact layer with a Mg doping concentration of 10^{20} cm^{-3}. The detailed structure parameters of the four samples are listed in Table 6. More general information about the MOCVD growth of GaN can be found in Ref. 5.

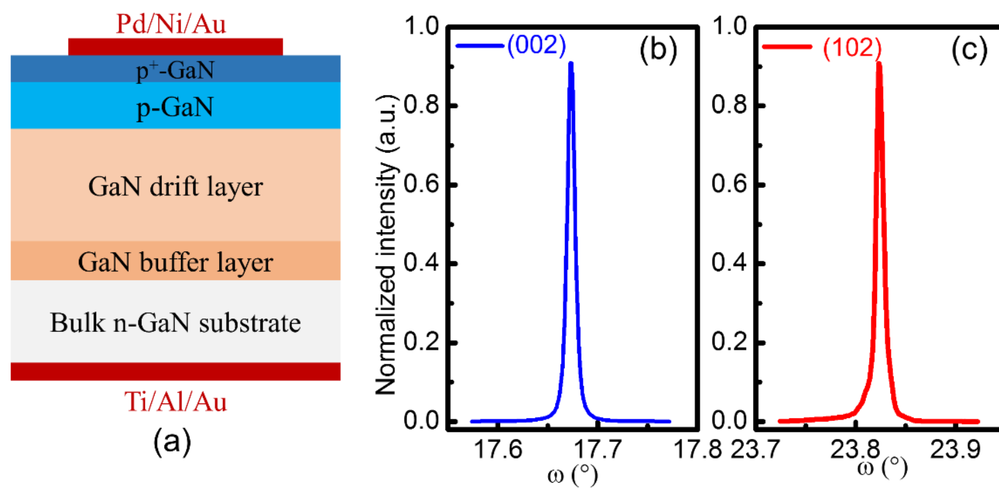

Fig. 24. (a) Schematic cross-section view of vertical GaN p-n diodes. RCs of (b) (002) plane and (c) (102) plane.

Table 6. Structure parameters of GaN p-n diodes with different buffer layers.

Layer description	A	B	C	D
p^+-GaN	20nm, [Mg]= 10^{20} cm^{-3}			
p-GaN	500nm, [Mg]= 10^{19} cm^{-3}			
Drift layer	9μm, UID	9μm, UID	9μm, UID	9μm, [Si]
Buffer layer	50nm	400nm	1μm	1μm
Bulk GaN substrate	No split			

4.2 Material Characterizations by XRD and AFM

The as-grown samples were characterized by high resolution X-ray diffraction (HRXRD) using PANalytical X'Pert Pro materials research X-ray diffractometer (MRD) system. The X-ray source is Cu Kα radiation with a wavelength of 0.154 nm. The incident beam optics was hybrid monochromator and the diffracted beam optics was triple axis module. The (002) symmetric and (102) asymmetric plane rocking curves (RCs) were shown in Fig. 24(a) and 24(b), respectively. The FWHM of (002) RCs are 30–60 arcsec and FWHM of (102) RCs are 20–30 arcsec. The dislocation density D of the samples can be estimated based on the FWHM [66]:

$$D = \frac{\beta^2{}_{(002)}}{9\overrightarrow{b_1}^2} + \frac{\beta^2{}_{(102)}}{9\overrightarrow{b_2}^2} \tag{10}$$

where β is FWHM and $\vec{b}$ is the Burgers vector. The dislocation densities were estimated to be on the order of 10^6 cm^{-2} for all the samples. This is much lower than heteroepitaxial growth (> 10^9 cm^{-2}). The surface morphology of as-grown samples was also investigated

by Bruker's Dimension atomic force microscopy (AFM) and the results were shown in Fig. 25. We scanned regions with the size of 10 × 10 μm^2 and the root-mean-square (RMS) roughness was in the range of 0.5-1.5 nm. Based on the XRD and AFM results, we obtained high quality GaN epilayers on bulk GaN substrate with low defect densities and smooth surfaces.

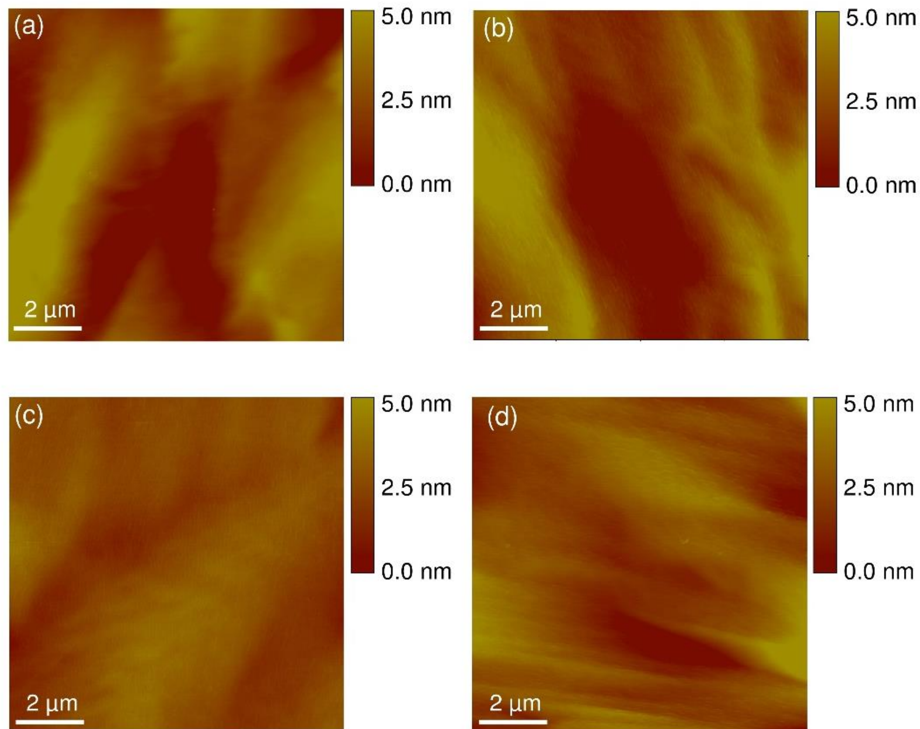

Fig. 25. AFM images of sample (a) A, (b) B, (c) C, and (d) D.

4.3 Device Fabrication

The devices were fabricated using traditional optical photolithography and metal deposition and lift-off processes. First, the as-grown samples were cleaned in acetone and isopropyl alcohol under ultrasonic to remove organic contaminations. And the patterns were transferred from masks to samples using photolithography. The circular mesa isolation was then realized using the chlorine based inductively coupled plasma (ICP) dry

etch at an ICP power of 350 W and a pressure of 5 mTorr. The etching depth was ~ 1.5 μm. Before depositing metal contacts on samples using electron beam evaporation, we briefly dipped them in hydrochloric acid to remove possible native Ga_2O_3 on top of the surface. The circular p-GaN ohmic contact has a diameter of 200 μm. Pd (20 nm) /Ni (30 nm) /Au (150 nm) metal stacks were deposited and subsequently annealed in N_2 at 450 C for 5 minutes. The p-contacts were studied by transmission line method (TLM). They showed good ohmic behavior with a contact resistance of 8.6×10^{-3} $\Omega\cdot cm^2$ and sheet resistance of 33.3 kΩ/sq. The entire backside of the samples was deposited with non-alloyed Ti (50 nm) /Al (200 nm) /Au (50 nm) stacks as n-type ohmic contacts. We didn't employ passivation or field plates (FP). The current–voltage (I–V) and capacitance-voltage (C–V) characteristics were measured using Keithley 4200-SCS parameter analyzer and Keithley 2410 sourcemeter. The reverse breakdown measurements were conducted in non-conductive Fluorinert liquid FC-70 to prevent flash-over.

4.4 Electrical Properties of P-N Diodes

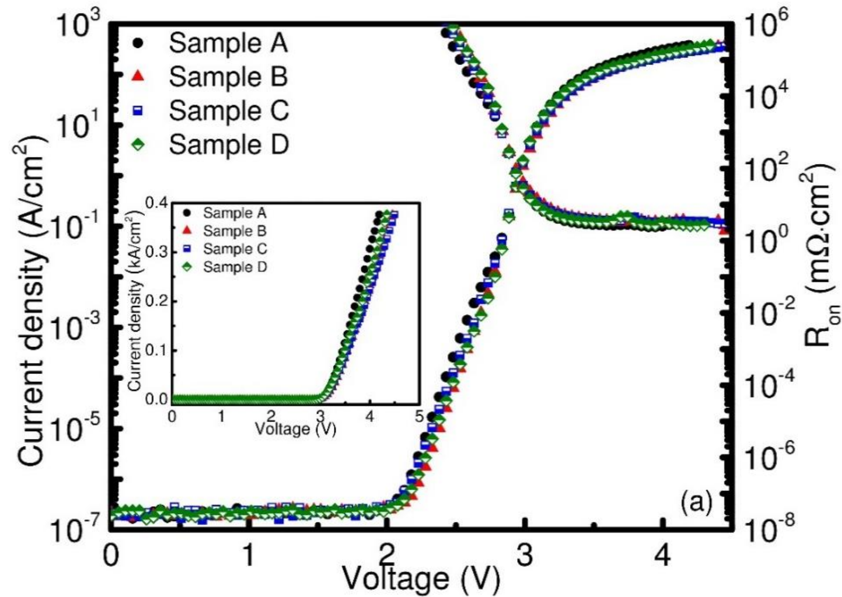

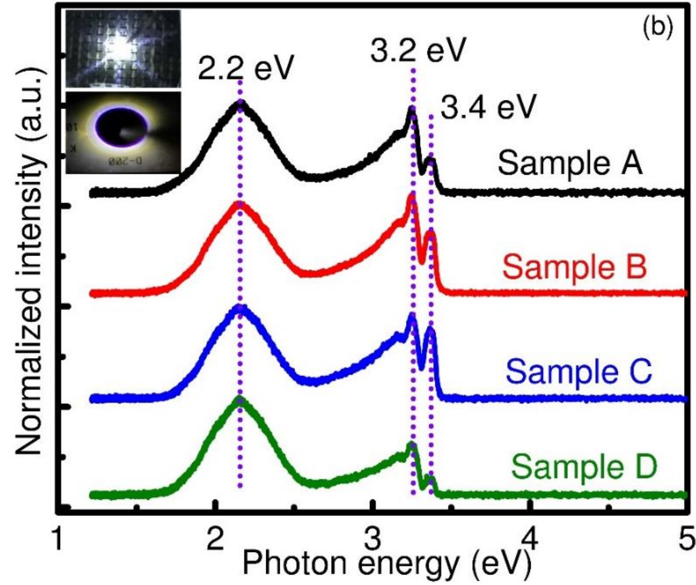

Fig. 26. (a) Forward I–V characteristics and R_{on} of sample A, B, C,and D in semilog scale. The insets are linear scale I–V curves. (b) EL spectrum of four samples at forward bias of 4 V. The inset shows images of illuminated samples.

Figure 26(a) shows that all diodes exhibited good rectifying behaviors with a turn-on voltage (V_{on}) of ~ 3.1 V and a high on/off ratio ~ 10^{10}. There is a slight difference in on-current between the four samples possibly due to inhomogeneous p-contact resistances [67]. We obtained a low R_{on} of ~3 mΩ·cm^2 on all devices at 4 V. It's interesting to note that strong light emission was observed on all devices under forward bias voltage beyond the turn-on voltage. This is due to the electron-hole radiative recombination in the p-n diodes and is often seen as an indicator of high material quality of the devices. We analyzed the emission spectrum using a spectrometer and the measured electroluminescence (EL) spectrum were shown in Fig. 26(b). We observed three EL peaks at 2.2 eV (deep-level transition), 3.2 eV (conduction band to acceptor level transition) and 3.4 (band-edge emission), respectively [67]. The strong light

emission indicates the high material quality of the homoepitaxially grown devices due to low defect densities which can serve as nonradiative recombination centers.

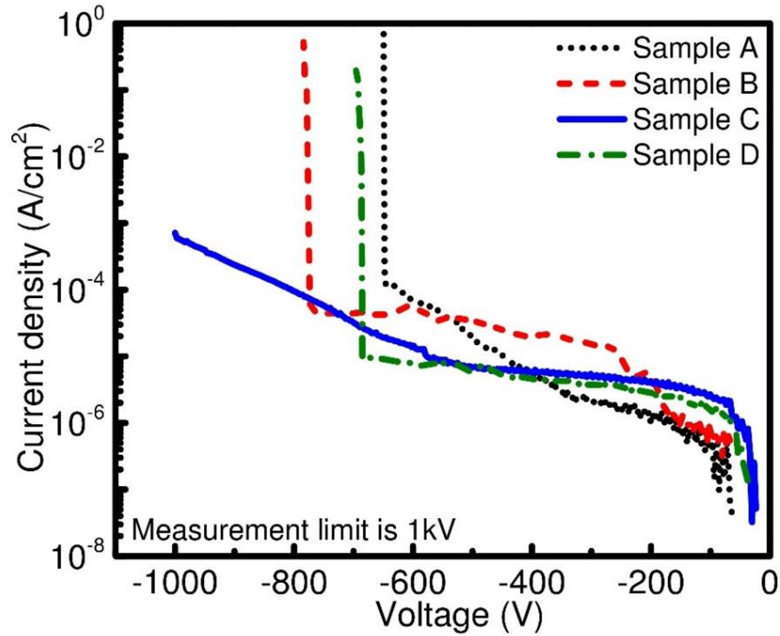

Fig. 27. Reverse I–V characteristics of sample A, B, C and D.

The breakdown measurements of the four samples were shown in Figure 27. We can see that with increasing buffer layer thickness, the V_{BD} increases comparing sample C (more than 1000 V), sample B (772 V) and sample A (647 V). Therefore, buffer layer thickness plays an important role in enhancing the breakdown capability. We also observed the V_{BD} difference between sample C and D (687 V) due to the different the doping concentrations of the drift layers. According to the analysis in the following, the better material quality due to thicker buffer layer and/or lower net doping concentration of drift layer can enhance V_{BD}.

4.5 Electrical Properties of Schottky Barrier Diodes

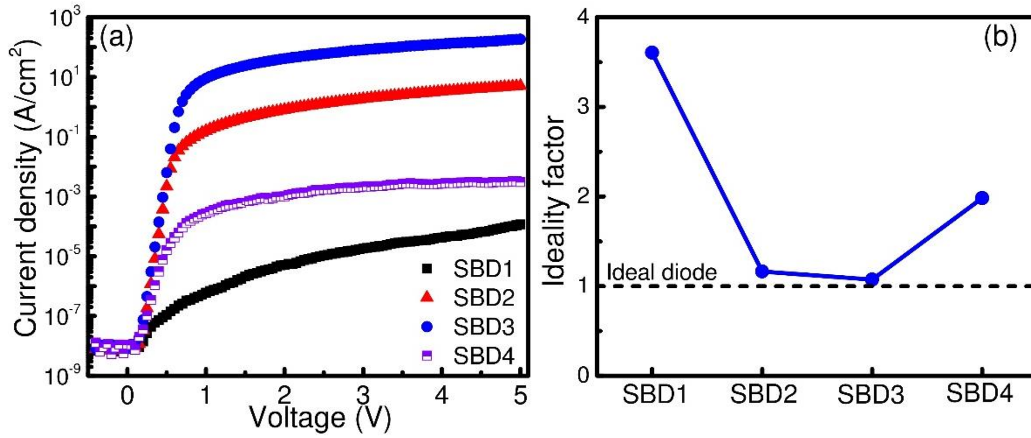

Fig. 28. (a) Forward I–V characteristics and (b) ideality factor of SBD1, SBD2, SBD3, and SBD4.

We also fabricated Pd/GaN SBDs on the same drift layers without growing p-GaN layer in order to investigate the electrical properties of the drift layers. The SBDs have different n^+-GaN buffer layer thickness (20 nm, 100 nm, 400 nm, and 400 nm for SBD1, SBD2, SBD3, and SBD4), and a 9-µm-thick UID or lightly doped ([Si] = 2×10^{16} cm^{-3} only for SBD4) drift layer. Please be noted that in Fig. 26(a), all the p-n diodes showed comparable forward currents possibly due to large p-contact resistance. However, Fig. 28(a) shows that the SBDs with different buffer layer thickness had distinct on-currents. Since forward currents of SBDs is mainly determined by the metal/drift layer interface, this indicates that buffer layer thickness can impact the electrical properties of the drift layers. In addition, ideality factor is an indicator of material quality. SBD3 had a near unity ideality factor of 1.07, indicating high material quality of the drift layer [68]. As shown in Fig. 28(b), the ideality factor decreases with increasing buffer layer thickness. Therefore, the material quality of the drift layer increases with buffer layer

thickness. And high doping concentration in the drift layer can decrease the ideality factor and reduce the material quality. These results indicate that it's better to grow a thick buffer layer for high voltage p-n diodes although they may be homoepitaxially grown on bulk substrates.

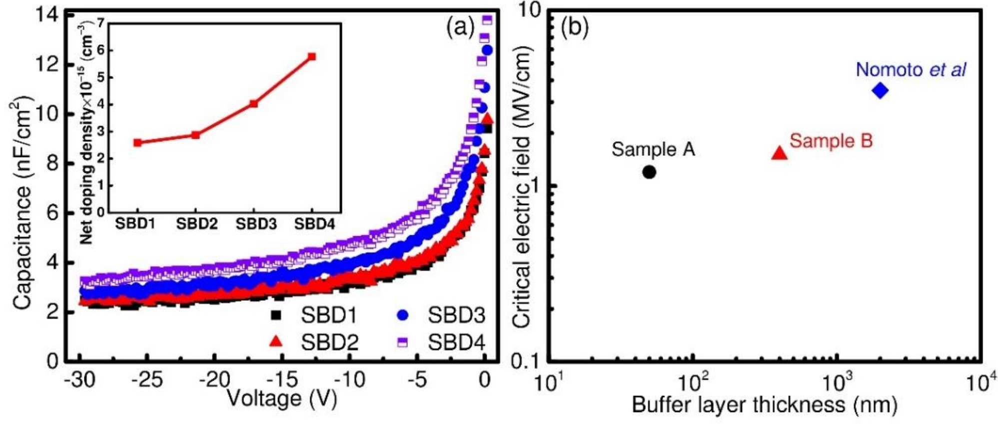

Fig. 29. (a) C–V characteristics at a frequency of 1 MHz. The inset shows the net doping concentration for the four devices. (b) Comparison of critical electric field of p-n diodes with different buffer layer thicknesses [69].

We can extract the net doping concentration ($N_D - N_A$) using [69]

$$d\left(1/C^2\right)/dV = -\frac{2}{q\varepsilon_0\varepsilon_r(N_D - N_A)} \tag{11}$$

where q is electron charge, ε_0 is permittivity of the vacuum, and ε_r is relative permittivity of GaN. The ($N_D - N_A$) can be calculated from the slope of $1/C^2$ vs V, which is in the range of 2×10^{15} to 4×10^{15} cm^{-3}. From Fig. 29(a), the ($N_D - N_A$) increases with increasing buffer layer thickness, possibly related to charged defects in GaN [70]. In addition, in a punch-through structure, the critical electric field E_c and V_{BD} are related by [69]

$$V_{BD} = E_c t_{DR} - \frac{q\left(N_D - N_A\right)t_{DR}^2}{2\varepsilon_0\varepsilon_r} \tag{12}$$

where t_{DR} is the thickness of drift layer. As shown in Fig. 29(b), E_c also increases with increasing buffer layer thickness. Figure 30 shows the SBDs have similar trend in V_{BD}: thicker buffer layer can enhance the V_{BD} while high doping concentration in drift layer can reduce it.

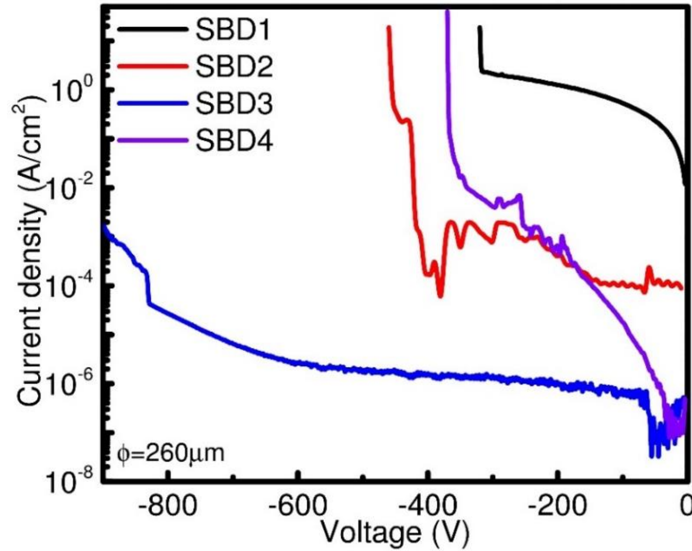

Fig. 30. Reverse I-V characteristics of SBD1, SBD2, SBD3 and SBD4.

4.6 Summary

This work shows that buffer layer has significant impacts on the device performance even though homoepitaxial growth is concerned. A thicker buffer layer will significantly enhance the breakdown voltages of these devices possibly due to improved material quality of drift layers with reduced defect densities. Thicker buffer layers also result in slightly higher doping concentration in drift layer, which can lower V_{BD}. But the highest breakdown voltages were still obtained on devices with thickest buffer layers (Sample C and SBD3). This indicates material quality of a drift layer is very important in achieving high V_{BD}.

CHAPTER 5

VERTICAL GAN-ON-GAN P-N DIODES WITH HYDROGEN-PLASMA BASED EDGE TERMINATION

GaN power diodes tend to breakdown prematurely at the junction edge due to the electric field crowding effects [71], [72]. Therefore, edge termination techniques are of critical important for high voltage devices. Traditional technology uses ion-implantation to form the junction termination extension [73], [74]. The disadvantages are two-fold: first, significant material damages are induced due to the high energy ion bombardments; second, extremely high temperature (usually over 1500 °C) is needed to active these implanted atoms, which often results in lifetime killer defects [75], [76]. In addition, this technology is far from mature for GaN devices [72]. In this Section, we proposed a implantation-free edge termination a low-damage, low-temperature and easy-to-implement hydrogen-plasma based edge termination technique (HPET) to improve the V_{BD} of GaN p-n diodes [77]. The mechanism is that H atoms can strongly bond with Mg acceptors in p-GaN to form neutral Mg-H complexes [78], and effectively passivate p-GaN into highly resistive GaN (HR-GaN) [79]. The reliability issues of the hydrogen-plasma based technique have also been studied in GaN power devices [79]. In addition, this process can be easily realized by ICP tools. Therefore, the HPET can considerably reduce costs and simplify processes of the device fabrication.

5.1 Device Growth and Structure and Material Characterizations

The device growth was also carried out by MOCVD. The detailed growth process can be found in Section 4. As shown in Fig. 31(a), the GaN p-n diode consists of a n^+-GaN buffer layer, an UID drift layer, a p-GaN, and a heavily doped p^+-GaN contact layer.

The FWHM of the (002) and (102) RCs are 62.3 and 37.8 arcsec, respectively, as characterized by HRXRD in Fig. 32 (a). According to Eq. 10, we estimated the dislocation density to be 4.2×10^{6} cm^{-2}. The epilayers also had a smooth surface with RMS roughness of 0.33 nm as shown in Fig. 32(b).

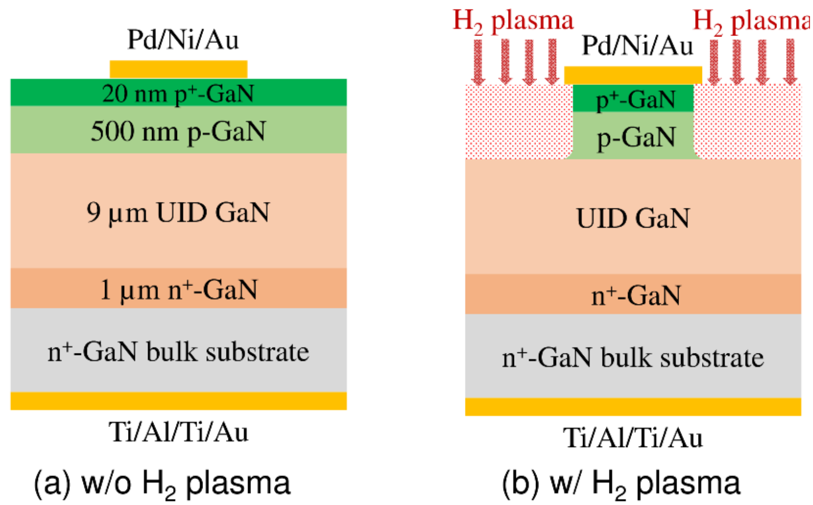

Fig. 31. Schematics of p-n diodes (a) without (b) with H_2 plasma treatment.

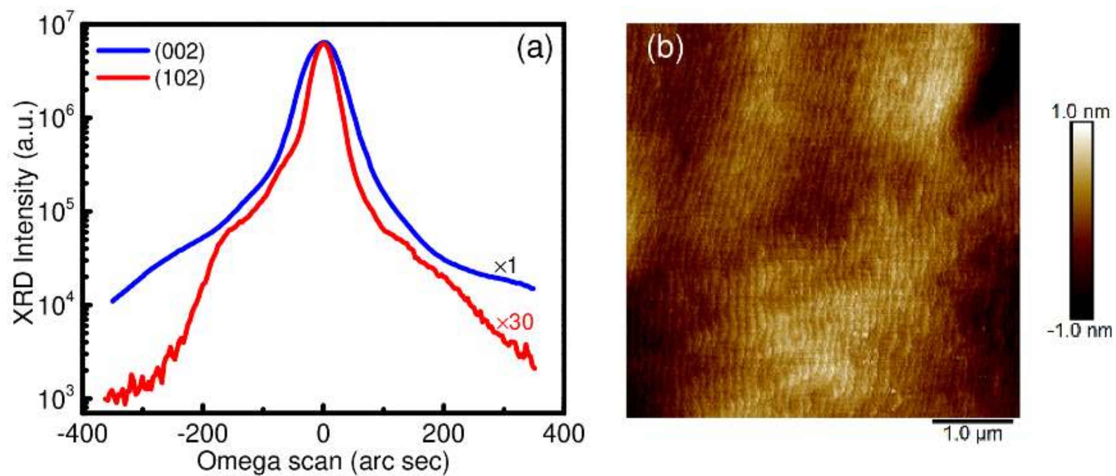

Fig. 32. (a) RCs of the (002) plane and the (102) plane of device. (b) The AFM image of the device with a 5×5 μm^2 scanning area.

5.2 Hydrogen-Plasma Treatment

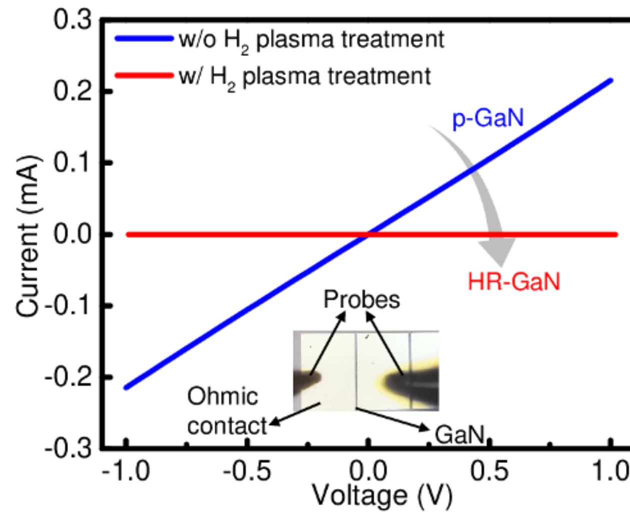

Fig. 33. I-V curves of two p-type ohmic contacts before and after H_2 plasma treatment.

The fabrication process before the H_2 plasma treatment was described in detail in Section 4. Then, the devices were treated by H_2 plasma using ICP at an ICP power of 300 W, an RF power of 10 W, a H_2 flow of 25 sccm, and a pressure of 8 mTorr for 10 minutes. Finally, the devices were annealed using RTA at 400 °C for 5 minutes to recover potential plasma damages and use the thermal diffusion process to fully passivate the p-GaN layer [79]. Figure 33 showed the currents between two ohmic contacts were completely blocked after the H_2 plasma treatment. This indicates that the H_2 plasma treatment has effectively passivated the p-GaN into HR-GaN that serves as the edge termination. The effects of ICP and RTA conditions on the device characteristics are worthy of further investigations. No passivation or FP were incorporated. The device without H_2 plasma treatment was used as a reference.

5.3 Capacitance-Voltage (C-V) Characteristics

According to Eq. 11, the $(N_D - N_A)$ of the UID GaN drift layer was estimated to be ~ 6.7×10^{15} cm^{-3}, due to the background doping of the MOCVD reactor.

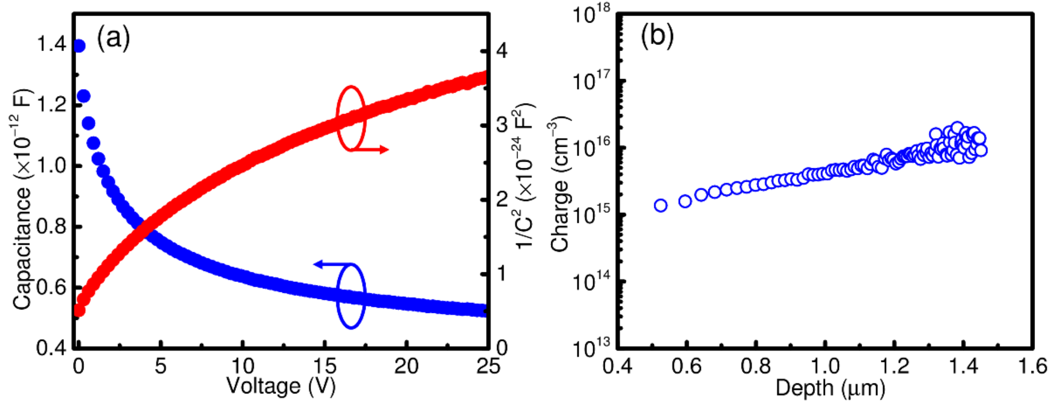

Fig. 34. (a) C and $1/C^2$ versus V at a frequency of 1 MHz. (b) The extracted carrier concentration profile.

5.4 Forward Current-Voltage (I-V) Characteristics

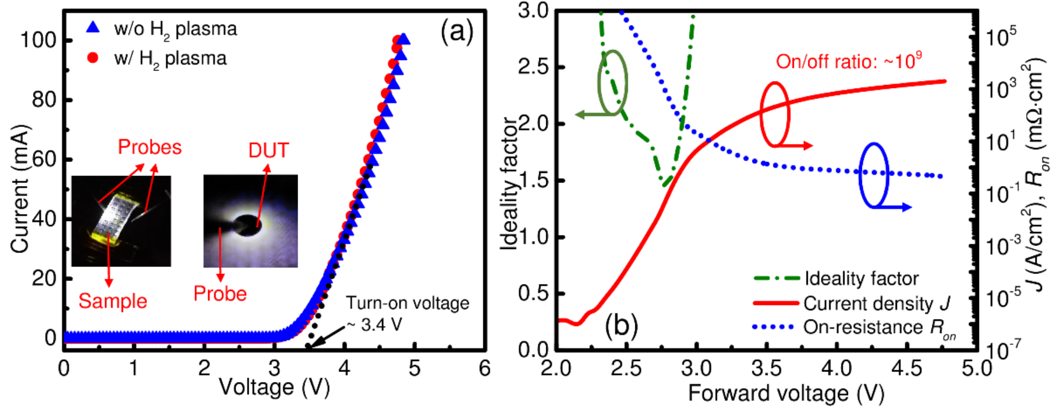

Fig. 35. (a) Forward I–V characteristics of GaN p-n diodes w/o and w/ the HEPT. (b) The current density, R_{on}, and ideality factor vs. voltage for the device w/ the HPET.

As shown in Fig. 35(a), the devices w/ and w/o the HPET showed comparable forward I-V characteristics with a V_{on} of ~3.5 V. This indicates that the H_2 plasma treatment doesn't degrade forward I-V characteristics. In addition, we also observed

strong light emission at bias beyond V_{on}, which was discussed in detail in Section 4. The device with the HPET exhibited good rectifying behaviors with a high on-current of ~ 2 kA/cm^2, a high on/off ratio ~ 10^9 and a low R_{on} of 0.45 mΩ·cm^2. The ideality factor n first deceases to a minimum of 1.4 at 2.7 V and then increase. The decrease is due to the transition from the Shockley-Read-Hall (SRH) recombination current to the diffusion current and the increase is due to the series resistance effects [69].

5.5 Reverse Breakdown

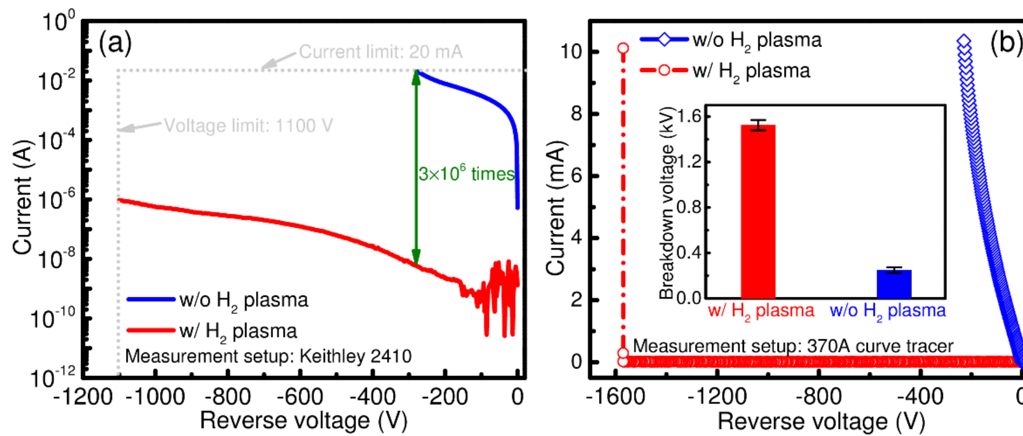

Fig. 36. Reverse *I–V* characteristics measured by (a) Keithley 2410 and (b) Tektronix 370A curve tracer.

Two setups were used to do the reverse breakdown measurements in Fig. 36: (i) Keithley 2410 with a voltage limit of 1.1 kV and (ii) Tektronix 370A curve tracer with a voltage limit of 2.0 kV. Keithley 2410 is mainly used to measure the leakage currents due to its high current resolution and 370A curve tracer to conduct the breakdown measurements due to its high voltage limit. The device with the HPET showed a 3×10^6 times smaller leakage current than the device without the HPET. This is likely attributed to two reasons: (1) The HPET confines the majority of the currents under the contacts

and avoids possible leakage pathways; (2) The HPET can help suppress the peak electric fields at the junction edge. The V_{BD} was enhanced significantly from ~ 300 V to 1570 V with the HPET. According to Eq. 12, the E_c of the device with the HPET was calculated to be ~ 3.0 MV/cm.

5.6 Benchmark Plot

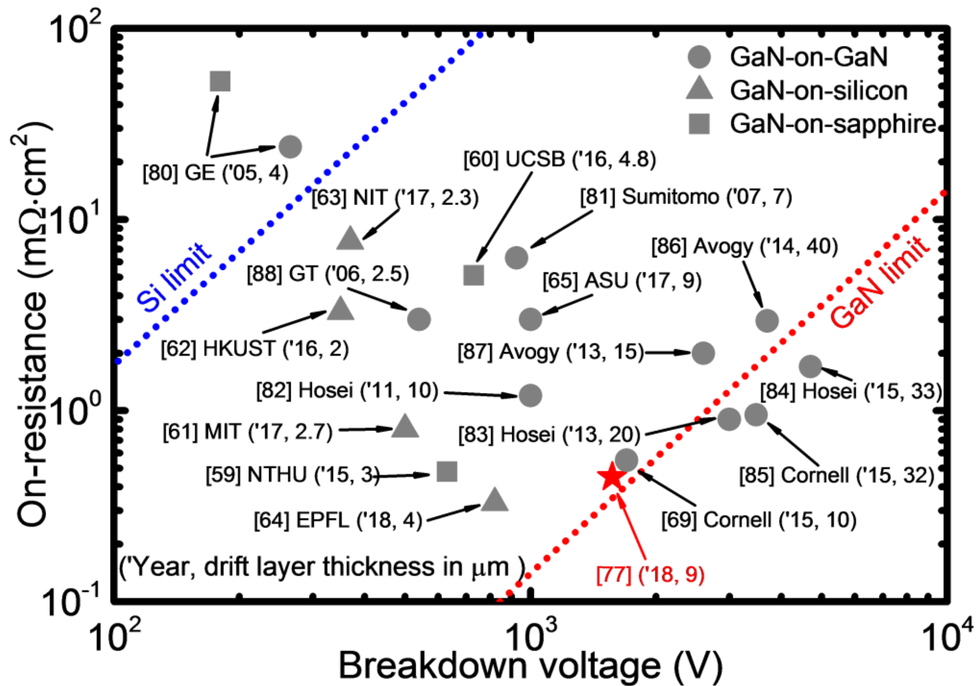

Fig. 37. Benchmark plot of R_{on} vs. V_{BD} for vertical GaN p-n diodes. The publication year and the drift layer thickness in μm of each device are marked.

Figure 37 shows the benchmark plot of the vertical GaN p-n diodes [59]-[65], [69], [77], [80]-[88]. The Baliga's figure-of-merit (FOM) (V^2_{BD}/R_{on}) of the device with the HPET in this work [77] was calculated to be 5.5 GW/cm^2, which is very close to the theoretical limit line of GaN. The V_{BD} of this GaN p-n diode [77] is comparable to or higher than other reports with similar drift layer thicknesses [65], [69], [81], [82]. The R_{on} of this work is among the lowest reported values for over 1 kV vertical GaN p-n diodes.

5.7 Summary

We experimentally demonstrated the HPET in vertical GaN p-n power diodes. The device performance was close to the theoretical limit of GaN with much reduced reverse leakage current and enhanced V_{BD}. These results confirmed the effectiveness of this technique. Future work includes the reliability issues and dynamic characteristics of the HPET in GaN power diodes. Considering the low-cost, low-damage and simplified fabrication processes, this demonstrates the potential of this technique for high performance GaN p-n diodes.

CHAPTER 6

VERTICAL GAN-ON-GAN SCHOTTKY BARRIER DIODES WITH DOUBLE DRIFT LAYERS

Recent years have seen intensive studies on vertical GaN-on-GaN p-n diodes and SBDs with high V_{BD}. Kizilyalli *et al.* [86] demonstrated a p-n diode with a high V_{BD} of 3.7 kV using a single drift layer (SDL). To further enhanced the V_{BD}, Ohta *et al.* [84] proposed a multi-drift-layer (MDL) design that enabled a V_{BD} of 4.7 kV. However, one of the major shortcomings of GaN p-n diodes is their large V_{on} (usually over 3 V) [67] due to the large bandgap of GaN (3.4 eV). This can lead to large power loss for power switching applications. The two major losses in a power switch are conduction loss (P_C, $IV_{on} + I^2R_{on}$) and switching loss (P_S, $IV(T_R+T_F)f$, where T_R is rise time, T_F is fall time and f is switching frequency) [18]. The large V_{on} of GaN p-n diodes will result in a large P_C. Since p-n diodes are minority carrier devices, they usually have very large T_R, T_F and therefore P_S, due to the reverse recovery charge during on/off transition.

GaN vertical SBDs are ideal candidates for efficient low loss power switching. SBDs can achieve small V_{on} (usually less than 1 V) due to the Schottky barrier interface, thus reducing P_C. Due to being majority devices, SBDs have no reverse recovery charge and thus almost no P_S. Despite these advantages, currently the device performance of GaN vertical SBDs are still inferior to those of GaN p-n diodes in terms of V_{BD} and R_{on} mainly due to two challenges. The first challenge is the growing high quality thick GaN drift layers and precisely controlling the doping concentrations in these drift layers [13]. This challenge can be solved through MOCVD growth optimizations. The second challenge is balancing R_{on} and V_{BD} since low R_{on} requires thin and highly doped drift

layers while high V_{BD} needs thick and lowly doped drift layers. The solution to this problem is to introduce MDL design into GaN vertical SBDs. It has already been shown in GaN p-n diodes that reducing the doping concentration of the top drift layer can suppress the peak electric field at the junction and thus enhance the V_{BD}. At the same time, the bottom drift layer can be moderately doped to achieve low R_{on} [84]. The same principle can also be applied to SBD devices. Figure 38 illustrates how double drift layer (DDL) structures can increase the V_{BD} in SBDs, where properties of top drift layer (doping, thickness, etc.) play significant roles. In this Section, we showed that GaN DDL SBDs can achieve low V_{on}, low R_{on}, and high V_{BD} simultaneously [89], which are ideal for high efficiency, high voltage, and high frequency power switching applications.

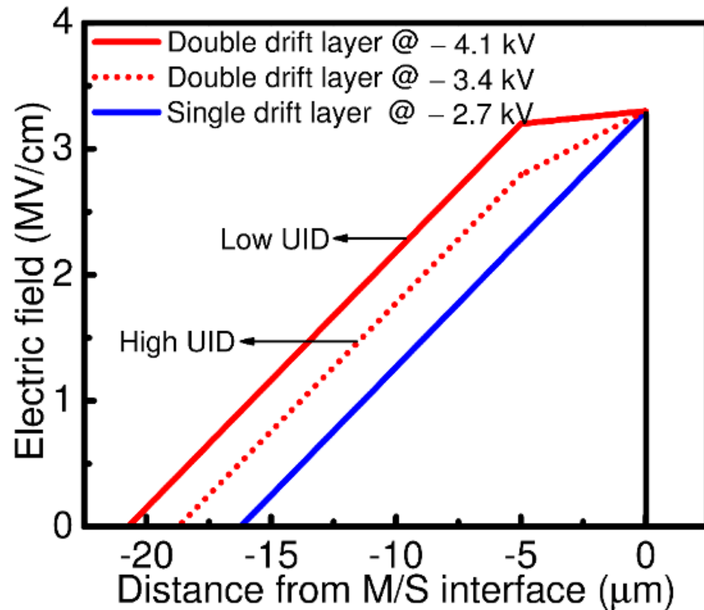

Fig. 38. Theoretical calculation of electric fields by one-dimensional Poisson's equation for SDL structure biased at −2.7 kV, DDL structure with high UID top drift layer biased at −3.4 kV, and DDL structure with low UID top drift layer biased at −4.1 kV. Breakdown was assumed to occur at a peak electric field of 3.3 MV/cm.

6.1 Device Structure and Material Characterization

The growth of GaN SBDs epilayers by MOCVD has been described in Section 4. Figure 39 shows the schematics of device structures for diode A and diode B. Diode A has a single drift layer of 9 µm. Diode B has double drift layer with a total thickness of 9 µm.

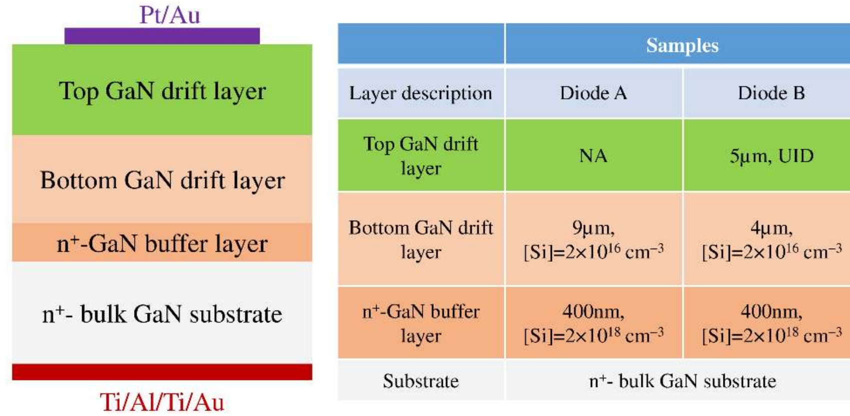

	Samples	
Layer description	Diode A	Diode B
Top GaN drift layer	NA	5µm, UID
Bottom GaN drift layer	9µm, [Si]=2×10^{16} cm^{-3}	4µm, [Si]=2×10^{16} cm^{-3}
n+-GaN buffer layer	400nm, [Si]=2×10^{18} cm^{-3}	400nm, [Si]=2×10^{18} cm^{-3}
Substrate	n+- bulk GaN substrate	

Fig. 39. Schematic view of cross-section (left) and device structure (right) for diode A and B.

The crystal quality of as-grown samples was characterized by HRXRD measurement as shown in Figs. 40 (a) and 40(b). For diode A, the FWHM of (002) RC was 60 arc sec and the FWHM of (102) RC was 26 arc sec. For diode B, they were 50 arc sec and 32 arc sec, respectively. Please be noted that in the homoepitaxially grown high quality GaN epilayers (102) FWHM is smaller than (002) FWHM, while heteroepitaxial growth usually have larger (102) FWHM [13]. The dislocation density of the samples can be estimated using the Eq. 10. The first term represents the screw dislocation density and the second term is the edge dislocation density. In both samples, the screw dislocation dominates. Both samples have dislocation densities in the low 10^6 cm^{-2} range. Figs. 40(c) and 40 (d) show the surface morphology of diode A and diode B by AFM. The RMS

roughness of the samples were 0.15 nm for diode A and 0.13 nm for diode B. Table 7 summarizes the material characterization results of the as-grown samples.

Table 7. Material characterizations of diode A and diode B by HRXRD and AFM.

Sample	(002) FWHM (arc sec)	(102) FWHM (arc sec)	Screw dislocation ($\times10^6$ cm^{-2})	Edge dislocation ($\times10^6$ cm^{-2})	RMS (nm)
Diode A	60	26	3.5	0.2	0.15
Diode B	50	32	2.4	0.3	0.13

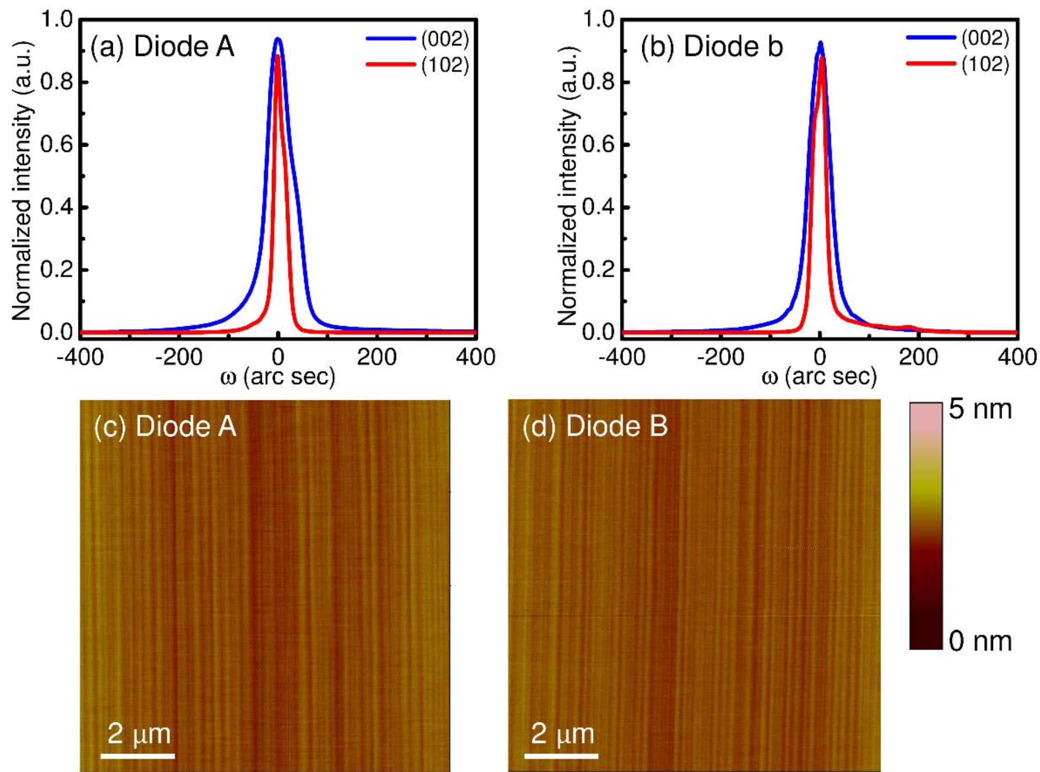

Fig. 40. (a)-(b) (002) and (102) RCs. (c)-(d) AFM images.

The fabrication of the GaN SBDs was described in Section 4. The Schottky contact (diameter of 200 μm) was Pt/Au (30 nm / 120 nm) metal stacks. For n-type ohmic

contact, non-alloyed Ti/Al/Ti/Au (20 nm / 50 nm / 20 nm / 100 nm) stacks were formed at the backside of GaN bulk substrate using electron beam evaporation without thermal annealing. No passivation, field plate (FP) or edge termination technologies were employed in the devices. The description about the measurement setups can be found in Section 4.

6.2 Forward I-V at Room Temperature (RT)

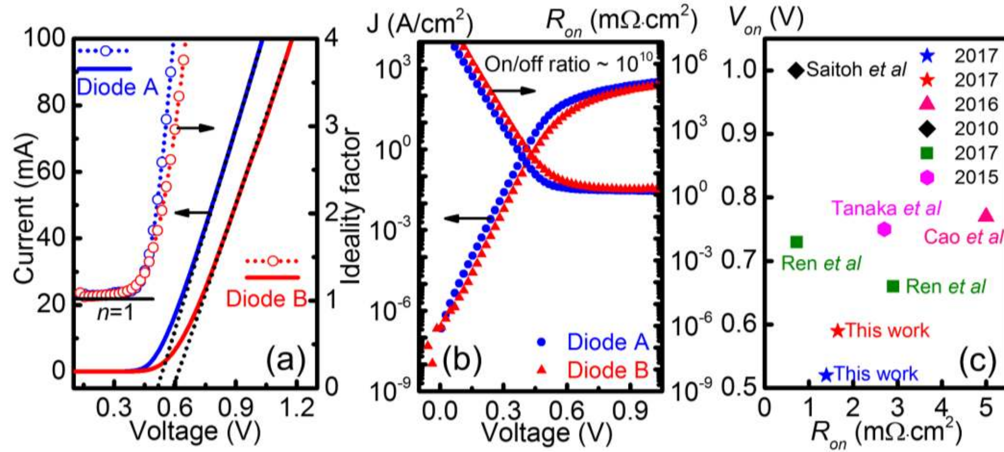

Fig. 41. (a) Forward current and ideality factor vs. voltage in linear scale. (b) Forward current density and R_{on} vs. voltage in semi-log scale. (c) Comparison of V_{on} and R_{on} of reported vertical GaN SBDs.

As shown in Fig. 41(a), Diode A had a V_{on} of ~ 0.52 V and diode B ~ 0.59 V. Both devices demonstrated record low V_{on} values for vertical GaN-on-GaN diodes. The ideality factor n as a function of voltage was also extracted by [13]

$$n = \frac{q}{kT}\frac{1}{d\log(J)/dV} \tag{13}$$

Near unity idealities were obtained for both diodes at low bias: n = 1.06 for diode A and n = 1.04 for diode B. In Fig. 41(b), both diodes showed high on/off ratio on the order of 10^{10}. At the current of 0.1 A, diode A has a R_{on} of 1.39 m$\Omega\cdot$cm^2 while diode B has a

slightly larger R_{on} of 1.65 mΩ·cm^2. Figure 41(c) shows that the devices in this work had comparable or better V_{on} and R_{on} compared with previous reports [13], [89]-[92]. The R_{on} can be decomposed into three components [13]

$$R_{on} = R_{sub} + R_{SBD} + R_{con} = R_{sh}d^2 + t/q\mu(N_D - N_A) + R_{con} \quad (14)$$

where R_{sub}, R_{SBD}, and R_{conN} are resistance of the substrate, the SBD, and the contact, respectively, R_{sh} is the sheet resistance of the substrate, d is the thickness of the substrate, t and μ are the thickness and the electron mobility of the drift layers of GaN SBDs. R_{sub} of our devices was 0.47 mΩ·cm^2. R_{con} is usually negligibly small compared with R_{sub} and R_{SBD} [13]. The μ of the drift layers was calculated to be 886.1 cm^2/(V·s) for diode A and 1045.2 cm^2/(V·s) for diode B. Diode A had a lower electron mobility possibly due to stronger impurity scattering from silicon dopants. These results indicated GaN SBDs with DDLs could have forward device characteristics comparable to SDL GaN SBDs.

6.3 C-V Measurement at RT

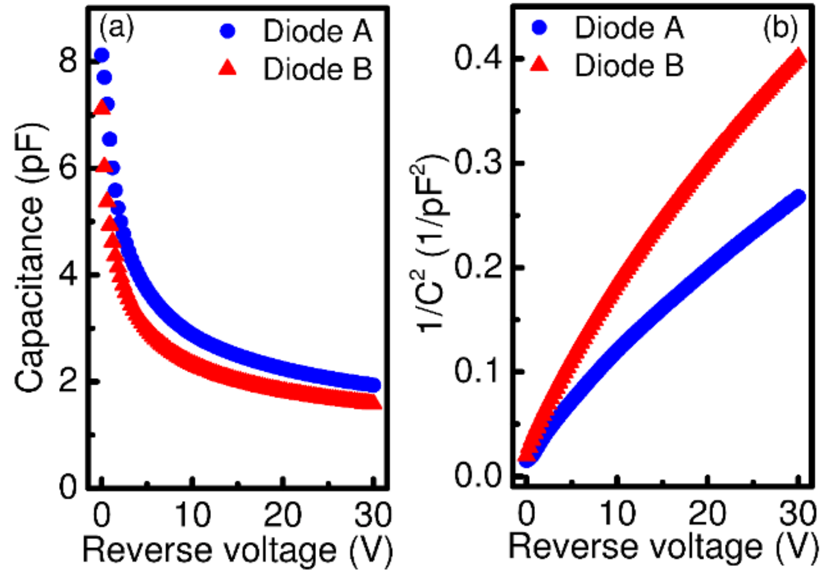

Fig. 42. (a) C–V and (b) 1/C^2–V characteristics of diode A and diode B at 1 MHz.

Figure 42 shows the C–V and $1/C^2$–V characteristics of diode A and diode B at a frequency of 1 MHz. According to Eq. 11, the ($N_D - N_A$) of the GaN SBDs of diode A and diode B are 6.9×10^{15} cm^{-3} and 4.6×10^{15} cm^{-3}, respectively. With a nominal Si concentration of 2×10^{16} cm^{-3}, the compensating acceptor concentration was estimated to be on the level of 10^{16} cm^{-3} [68].

6.4 Reverse Breakdown at RT

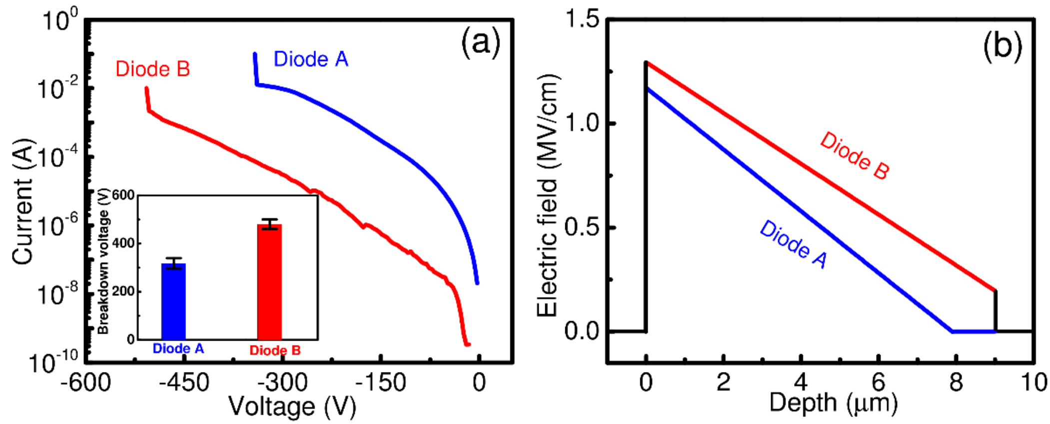

Fig. 43. (a) Reverse I–V characteristics of diode A and B. The inset shows V_{BD} of diode A and B. (b) Electric field profiles of diode A and B.

Figure 43(a) presents the reverse I–V characteristics of diode A and diode B. Diode A showed a V_{BD} of ~340 V while diode B broke down at ~503 V, indicating DDLs can enhance the breakdown capability of GaN SBDs. The catastrophic damages of the GaN SBDs indeed occurred at the edge of Schottky contacts possibly due to severe edge electric field crowding. With the critical electric fields obtained using Eq. 12, the electric field profiles in diode A and diode B were plotted in Fig. 43(b) by one-dimensional Poisson's equation.

$$\frac{dE}{dt} = \frac{q(N_D - N_A)}{\varepsilon_0 \varepsilon_r} \tag{15}$$

where dE/dt is the slope of the electric field profile. The E_c were calculated to be 1.17 MV/cm and 1.30 MV/cm for diode A and diode B, respectively. The smaller breakdown voltage and critical electric field of diode A can be a result of a larger net carrier concentration. Table 8 summarizes the device performance metrics of diode A and diode B at RT.

Table 8. Device parameters of diode A and diode B.

Sample	N_D-N_A ($\times 10^{15}$ cm^{-3})	n	Φ_B (eV)	Mobility [cm^2/(V·s)]	R_{ON} (mΩ·cm^2)	V_{ON} (V)	V_{BD} (V)
A	6.9	1.06	0.69	886.1	1.39	0.52	340
B	4.6	1.04	0.70	1045.2	1.65	0.59	503

6.5 Temperature-Dependent Forward I-V

The I–V–T curves were described by the thermionic emission model [93]

$$I = I_0 \exp(q(V - IR_s)/nkT - 1) \quad (16)$$

$$I_0 = AA^* T^2 \exp(-\Phi_B / kT) \quad (17)$$

where I_0 is the saturation current, Φ_B is the Schottky barrier height, A is the contact area, A^* is the Richardson constant and R_s is the series resistance. After plotting ln (I_0/T^2) vs $1/T$, the barrier height of the Pt/GaN were extracted from the slopes as shown in Fig. 44(c). Φ_B of diode A was 0.69 eV and that of diode B was 0.70 eV. In Fig. 44(d), the n and R_{on} were extracted as a function of temperature. n showed a very weak temperature dependence in the range of 1.02~1.09, indicating nearly ideal and highly homogeneous metal/semiconductor interface.

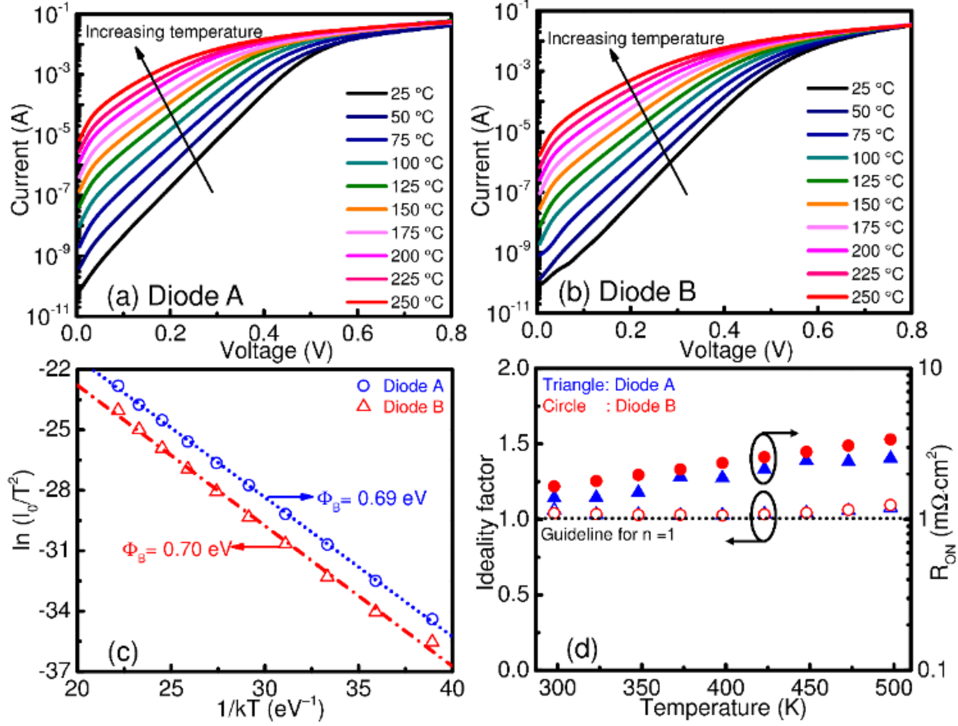

Fig. 44. Temperature-dependent forward I–V characteristics for (a) diode A and (b) diode B. (c) Richardson plot of the two diodes with Schottky barrier height extracted. (d) Ideality factor and R_{on} vs. temperature.

However, R_{on} clearly increased with increasing temperature. According to Eq. (14), the R_{SBD} and μ can be obtained as a function of temperature. ($N_D - N_A$) was almost constant from 25 °C to 250 °C. Therefore, the temperature dependence of R_{SBD} is due to μ. Over 100 K, μ(T) is mainly limited by the phonon scattering and can be characterized by the power-law relation [94], [95]

$$\mu(T) = \mu_0 (T / T_0)^{\gamma} \tag{18}$$

where μ_0 is the electron mobility at 300 K, T_0 is 300 K, and γ the power index. In Fig. 45, good agreements between experimental data and Eq. 18 were obtained on both devices. These results confirmed that the increase of R_{on} was caused by the decrease of phonon-

limited electron mobility with temperature. γ was −1.83 for diode A and −1.81 for diode B in the range between −1.5 and −2.5 [94]-[96].

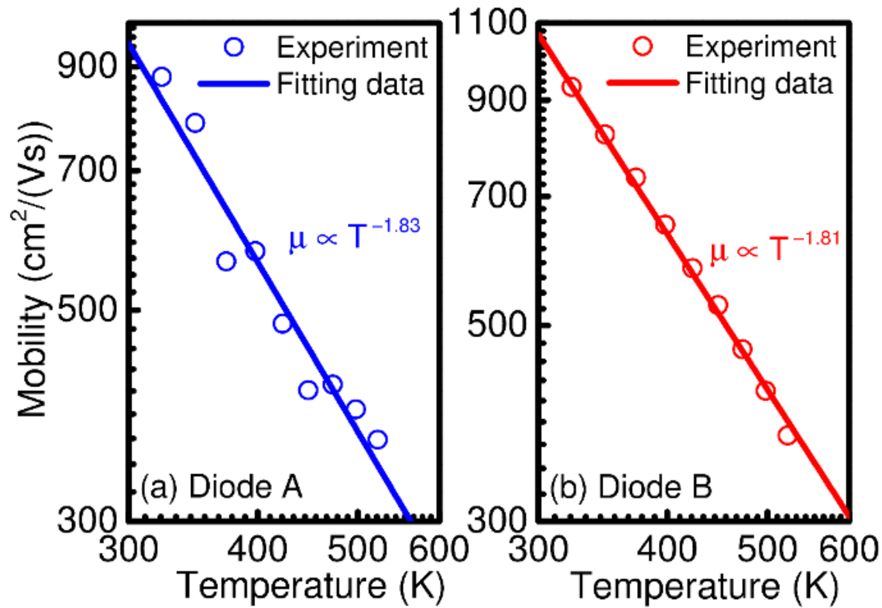

Fig. 45. Mobility vs. temperature for (a) diode A and (b) diode B in log-log scale.

6.6 Summary

This work shows that DDL design can balance the trade-off between desirable forward turn-on characteristics and high reverse breakdown capability, providing optimal overall device performances for power switching applications. Devices with DDL design had comparable forward characteristics and enhanced breakdown capability compared with those with SDL design. These results showed that GaN vertical SBDs with DDL designs are promising candidates for high efficiency, high voltage, high frequency power switching applications.

CHAPTER 7

OTHER WBG SEMICONDUCTORS BASED POWER ELECTRONICS

Recently, semiconductors with bandgap even larger than GaN have emerged for various optoelectronic and electronics applications, including beta-phase gallium oxide (β-Ga_2O_3) and AlN. In the following, we will mainly discuss β-Ga_2O_3 and AlN based power electronics. Due to the lack of the p-type semiconductors, only β-Ga_2O_3 and AlN SBDs have been demonstrated. With these new materials, new physics and device properties were revealed. Since β-Ga_2O_3 and AlN device studies are only in their inception, these preliminary results can serve as references and guidelines for future research.

7.1 Ga_2O_3 based Power Electronics

Compared with GaN, β-Ga_2O_3 has a larger bandgap (4.8 eV) and breakdown electric field (~ 8 MV/cm) and a 4 times larger Baliga's FOM. Cost-effective single-crystal β-Ga_2O_3 substrates are also commercially available, which is a big advantage of developing β-Ga_2O_3 devices. Due to its low cost and mass-production capability, edge-defined film-fed growth (EFG) has become one of the most popular methods used to grow β-Ga_2O_3 substrates [97].

7.1.1 Previous Studies on Material Anisotropy of Ga_2O_3

Due to the asymmetric monoclinic crystal structure of β-Ga_2O_3, its anisotropic material properties have garnered considerable attention, such as thermal [98], optical [99], and electronic properties [100], [101], and surface properties [102]-[104]. And, these anisotropic material properties may affect the performance of β-Ga_2O_3 electronic devices. Researchers have observed similar phenomena in III-nitride optoelectronics [1].

However, comprehensive study on the effect of crystalline anisotropy on the β-Ga_2O_3 electronic devices is still lacking. In the following, we fabricated vertical ($\bar{2}01$) and (010) β-Ga_2O_3 SBDs on EFG single-crystal substrates and systematically compared their electrical properties [105]. It's found out that the crystal orientations and associated surface properties do impact the device performance of β-Ga_2O_3 SBDs.

7.1.2 Surface Anisotropy Revealed by XPS

β-Ga_2O_3 crystal has a monoclinic structure ($C2$/m) with lattice constants $a = 1.223$ nm, $b = 0.304$ nm, and $c = 0.580$ nm and angles $\alpha = \gamma = 90°$, and $\beta = 104°$ [106], as shown in Fig. 46. There are two gallium sites: tetrahedrally-coordinated Ga_I and octahedrally-coordinated Ga_{II}, and three oxygen sites: O_I, O_{II} and O_{III}. ($\bar{2}01$) and (010) surfaces differ significantly in atomic configurations and density of dangling bonds [104].

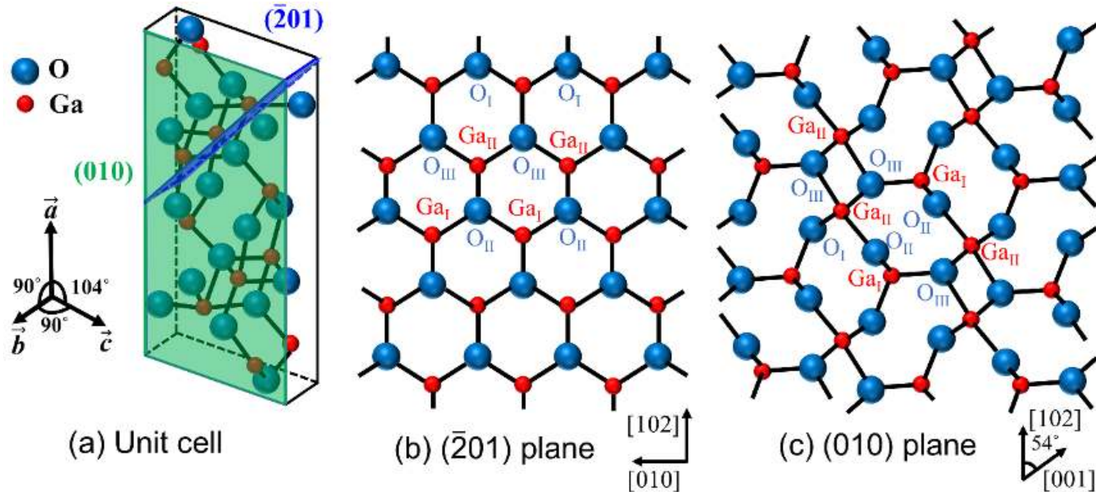

Fig. 46. (a) Unit cell of β-Ga_2O_3 crystal. Surface of (b) ($\bar{2}01$) and (c) (010) plane.

X-ray photoelectron spectroscopy (XPS) measurements were carried to study surface properties of the ($\bar{2}01$) and (010) surfaces. The valance band minimum (E_{VBM}) can be extracted by linearly extrapolating the leading edge of the valance band (VB) spectra to the baseline, as shown in Fig. 47. In n-type semiconductors, the Fermi level is pinned

at the charge neutrality level (CNL) at the surface due to surface states and defects. The surface barrier height Φ_{surf} is calculated as [107]

$$\Phi_{surf} = E_g - E_{VBM} \tag{19}$$

The Φ_{surf} was 1.14 eV for ($\bar{2}$01) and 1.63 eV for (010). The (010) surface has a much larger upward band bending. This explains the fact that it is more difficult to realize ohmic contacts on the (010) orientation [108], [109]. And the difference in Φ_{surf} can lead to different device performance.

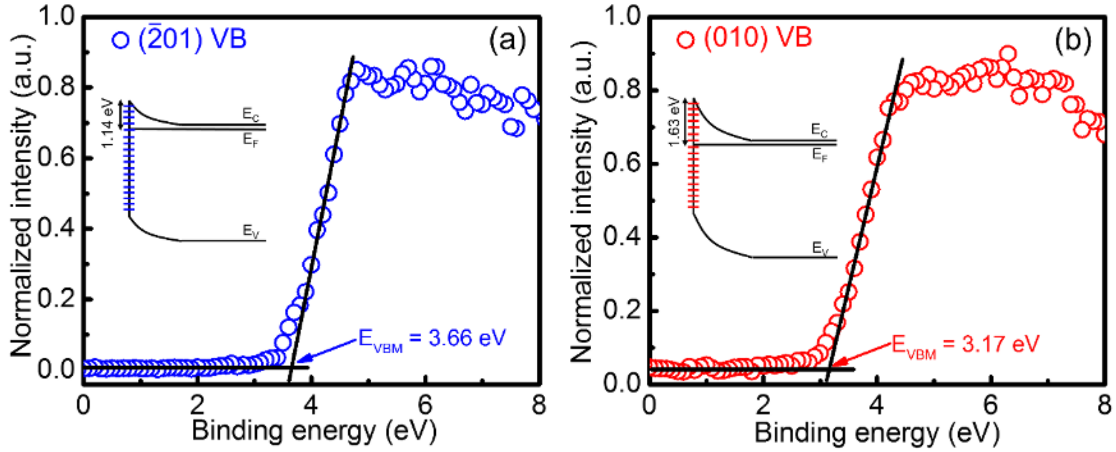

Fig. 47. XPS VB spectra of (a) ($\bar{2}$01) and (b) (010) β-Ga_2O_3. The insets indicate the upward band bending at the surfaces.

7.1.3 Anisotropic Electrical Properties of β-Ga_2O_3 SBDs

In Fig. 48(a), the V_{on} of ($\bar{2}$01) and (010) SBDs were 1.0 V and 1.3 V, respectively. At low bias, n was 1.34 and 1.55 for the ($\bar{2}$01) SBD and the (010) SBD, respectively. Both SBDs showed a high on-current of ~ 1.3 kA/cm^2 and on/off ratio of ~ 10^9. At 1.3 kA/cm^2, R_{on} was 0.56 and 0.77 mΩ·cm^2 for ($\bar{2}$01) and (010) SBDs, respectively. According to Eq. 14, the μ was calculated to be 125 cm^2/(V·s) for the ($\bar{2}$01) SBD and 65 cm^2/(V·s) for the (010) SBD. The difference is possibly due to anisotropic electron

transport properties on different crystal orientations [100], [101]. Figure 48 (c) shows this work obtained ultra-low R_{on} compared with previous reports.

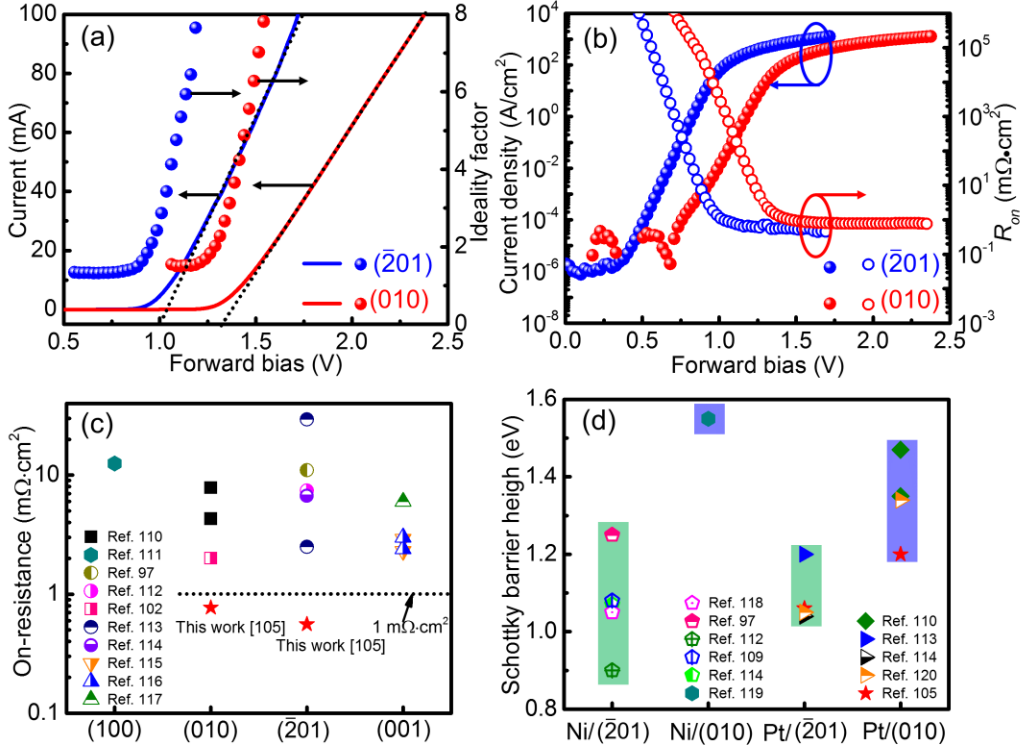

Fig. 48. (a) Current and ideality factor vs. forward bias in linear scale. (b) Current density and R_{on} vs. forward bias in semi-log scale. (c) Comparison of R_{on} of β-Ga_2O_3 SBDs on different orientations. (d) Comparison of Φ_B of reported ($\bar{2}01$) and (010) β-Ga_2O_3 SBDs.

The extracted Φ_B were 1.05 eV for the ($\bar{2}01$) SBD and 1.20 eV for the (010) SBD. Figure 48(d) shows that (010) SBDs generally have higher Φ_B than ($\bar{2}01$) SBDs, which is consistent with the larger Φ_{surf} of the (010) surface. Yao *et al*. showed Φ_B of β-Ga_2O_3 SBDs was more determined by surface states and defects than by metals used [120]. As shown in Figs. 46 and 47, the ($\bar{2}01$) and (010) surfaces have distinct Fermi level pinning and band bending. This indicates the interface states and defects between metal/β-Ga_2O_3 are different for ($\bar{2}01$) and (010) SBDs, leading to the discrepancy in Φ_B.

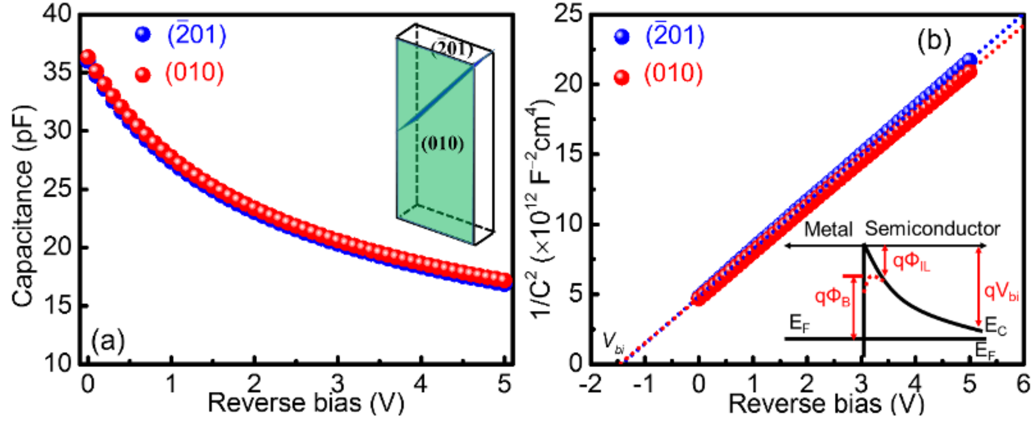

Fig. 49. (a) C–V and (b) $1/C^2$–V characteristics of ($\bar{2}$01) and (010) SBDs at 1 MHz. The inset in the right figure shows the band diagram of β-Ga_2O_3 Schottky interface.

The built-in voltage V_{bi} can be extracted from the x-intercept of $1/C^2$ vs. V in Fig. 49(b). The V_{bi} of the ($\bar{2}$01) SBD was 1.41 V and that of the (010) SBD was 1.44 V. The Φ_B can be decomposed into three components as shown in the inset of Fig. 49(b) [121]

$$q\Phi_B = qV_{bi} - q\Phi_{IL} + (E_C - E_F) \tag{20}$$

where Φ_{IL} is the image-force induced barrier height lowering, E_C is the CB minimum, and E_F is the Fermi level. Φ_{IL} is given by [121]

$$q\Phi_{IL} = \sqrt{qE_{SBD}/(4\pi\varepsilon_0\varepsilon_r)} \tag{21}$$

$$E_{SBD} = \sqrt{2qN_D V_{bi}/(\varepsilon_0\varepsilon_r)} \tag{22}$$

where E_{SBD} is the electric field at the metal/semiconductor interface. ($E_C - E_F$) is calculated by $kTln(N_C/(N_D - N_A))$ where N_C is the effective density states. The ($N_D - N_A$) was obtained from the slope of $1/C^2$ vs. V: 4.2×10^{18} cm^{-3} for ($\bar{2}$01) SBD and 4.3×10^{18} cm^{-3} for (010) SBD. After plugging in all the terms into Eq. 20, the Φ_B was 1.27 eV for ($\bar{2}$01) SBD and 1.30 eV for (010) SBD. Φ_B obtained from I-V are smaller than those from

C-V. This is usually attributed to the spatially inhomogeneous Φ_B caused by the interfacial states and defects [120], [122]. Furthermore, the two SBDs have very similar Φ_B according to the C-V data but a 0.15 eV Φ_B difference according to the I-V data. This is because C-V Φ_B doesn't involve current conduction and only determined by the doping concentrations of the semiconductors and, while the I-V Φ_B represents the barrier height for current flow [120]. Therefore, the C-V Φ_B is not impacted by crystal orientations and surface properties of β-Ga_2O_3.

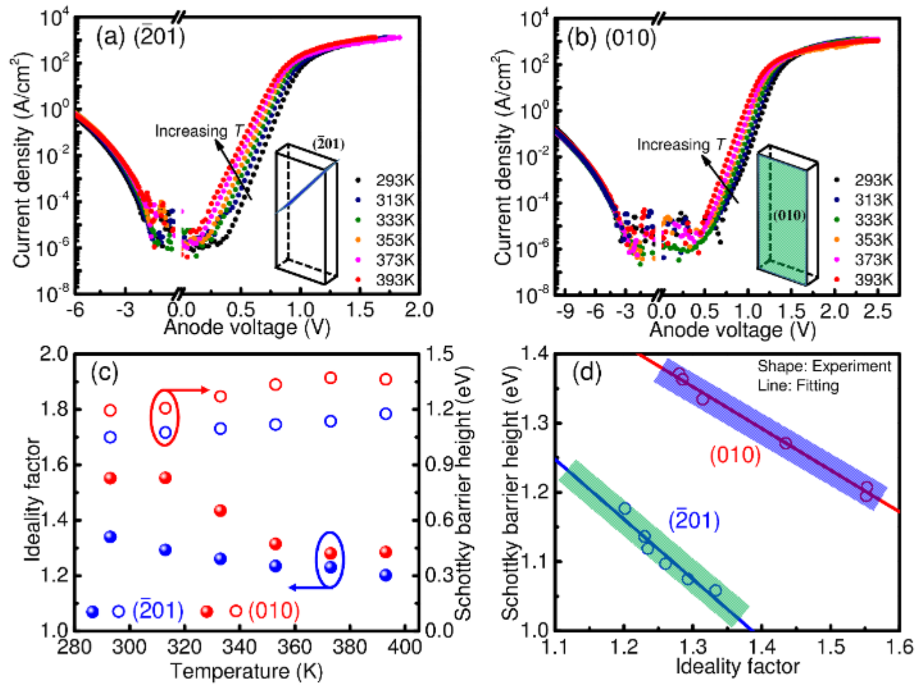

Fig. 50. Temperature-dependent I–V characteristics. (c) Ideality factor and Φ_B vs. temperature. (d) Φ_B vs. ideality factor.

The Φ_B and ideality factor of the devices were extracted as a function of temperature in Fig. 50(c). For the ($\bar{2}$01) [(010)] SBD, Φ_B increased from 1.05 (1.20) eV to 1.18 (1.36) eV and n decreased from 1.34 (1.55) to 1.20 (1.29) with increasing temperature. The temperature dependence of n, also called "T_0 anomaly", is caused by the

spatial inhomogeneity of Φ_B due to surface states and defects at the metal/semiconductor interface [122]. The n can be described as a function of temperature by [122]

$$n = 1 + T_0 / T \tag{23}$$

where T_0 is a constant associated with the standard deviation of the Φ_B distribution. In Fig. 50(d), there was a well-known linear relationship between the Φ_B and ideality factor due to the inhomogeneous Schottky barrier interfaces [122]. By extrapolation, the homogenous SBH ($\Phi_{B,\ I\text{-}V,\ h}$) when n = 1 was 1.33 eV for the ($\bar{2}$01) SBD and 1.53 eV for the (010) SBD. The device metrics of the two devices are summarized in Table 9.

Table 9. Device parameters of ($\bar{2}$01) and (010) Ga_2O_3 SBDs.

Sample	R_{on} (mΩ·cm^2)	V_{on} (V)	n	Mobility [cm^2/(V·s)]	$\Phi_{B,\ I\text{-}V,\ ih}$ (eV)	$\Phi_{B,\ I\text{-}V,\ h}$ (eV)	$\Phi_{B,\ C\text{-}V}$ (eV)
($\bar{2}$01)	0.56	1.0	1.34	125	1.05	1.33	1.27
(010)	0.77	1.3	1.55	65	1.20	1.53	1.30

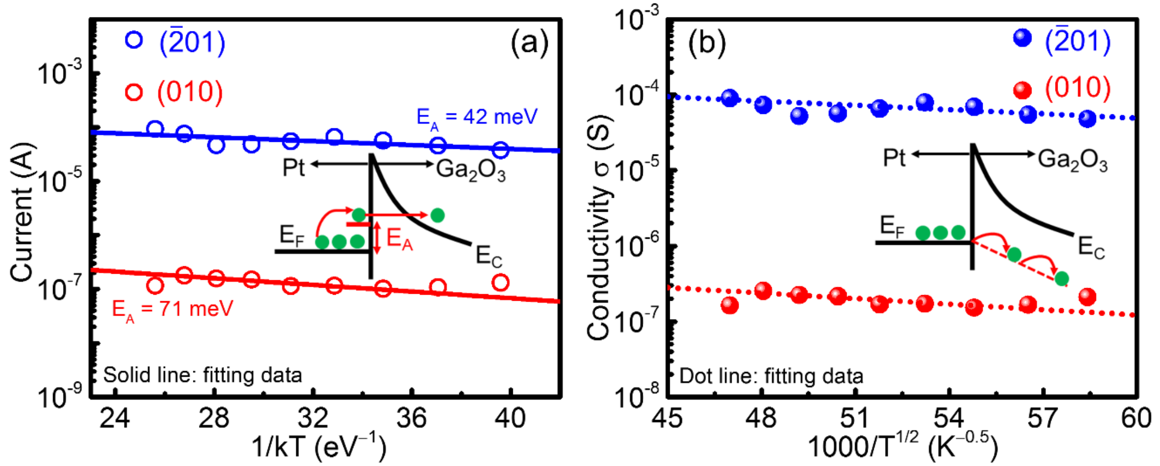

Fig. 51. (a) Arrhenius plot of reverse leakage current. (b) Conductivity as a function of $1/T^{1/2}$. The insets show the electron transport models.

The reverse leakage current of SBDs above RT is usually characterized by two models [123]. The first model is the two-step trap-assisted tunneling mechanism, where the electrons in the metal first are thermally excited to the trap states and then tunnel through the Schottky barrier. The reverse leakage current is proportional to $exp(-E_A/kT)$ where E_A is the activation energy. A good agreement was obtained between the experiment and this model in the Arrhenius plot in Fig. 51(a). E_A was 42 meV for the ($\bar{2}01$) SBD and 71 meV for the (010) SBD. Another possible model is the one-dimensional variable-range-hopping conduction (1D-VRH) model, where the electrons in the metal first fall into defect states associated with a dislocation near or below the Fermi level and are then transported into the semiconductor by hopping conduction. In this model, the conductivity is given by [123]

$$\sigma = \sigma_0 \exp[-(T_1 / T)^{1/2}] \tag{24}$$

where T_1 is the characteristic temperature, and σ_0 is a constant. Figure 51(b) shows a good linear fitting between experimental and simulation data. Further investigations are needed to determine the dominant mechanism. In addition, the ($\bar{2}01$) SBD exhibited higher reserve leakage current and smaller V_{BD} due to lower SBH.

7.2 AlN based Power Electronics

Ultra-wide bandgap semiconductors such as AlN (6.2 eV) have unique material properties that promise high power high frequency next generation RF and power applications. Compared to other semiconductors, AlN exhibits the largest bandgap, the highest breakdown field, and a decent thermal conductivity (Table 10). Furthermore, owning to the larger bandgap and excellent thermal performance, superior performance under harsh environment such as radiation and high temperature is also expected from

AlN devices. Despite these appealing properties, a coherent understanding is still elusive on the fundamental material properties of AlN, which significantly hinder the development of high performance electronic devices based on the material. Moreover, the majority of AlN SBDs are lateral devices that suffers from low breakdown voltage, large chip area and high cost.

Table 10. Properties of Si, SiC, GaN, and AlN power electronics [124].

Material	Bandgap (eV)	Electron mobility (cm^2/Vs)	Thermal conductivity (W/(mK))	Maximum operation (°C)	E_c (MV/cm)	Baliga's FOM
SiC	3.3 (I)	950	490	500	3.0	1
GaN	3.4 (D)	1200	130	650	3.3	2.5
AlN	6.3 (D)	1090	290	690	12	17

7.2.1 Ohmic Contacts to n-AlN

Due to the large bandgap of AlN, the activation energy of Si in n-AlN is ~250 meV, meaning less than 1% of donors can be thermally activated. This poses significant limitations to the developments of AlN based electronics. Through comprehensive optimizations, we successfully obtained high-quality ohmic contacts to n-AlN [125], [126]. Ti/Al/Ti/Au (20 nm / 100 nm / 20 nm / 50 nm) metal stacks were deposited by electron beam deposition followed by thermal annealing at 1000 °C in nitrogen for 30 seconds using RTA. The ohmic contacts of the devices were investigated by TLM from RT to 300 °C. As shown in Fig. 52(a), the contacts had good ohmic behavior with a low

contact resistance of 2.8×10^{-5} Ω·cm^2. In addition, the ohmic contacts also showed good thermal stability up to 300 °C.

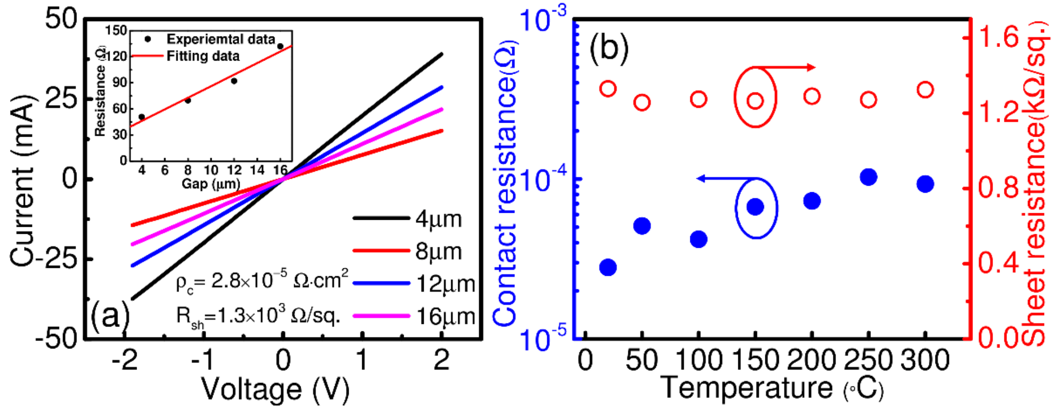

Fig. 52. (a) TLM I–V characteristics of the ohmic contacts at RT. (b) Contact resistance and sheet resistance vs. temperature.

7.2.2 Effect of Surface States on AlN SBDs

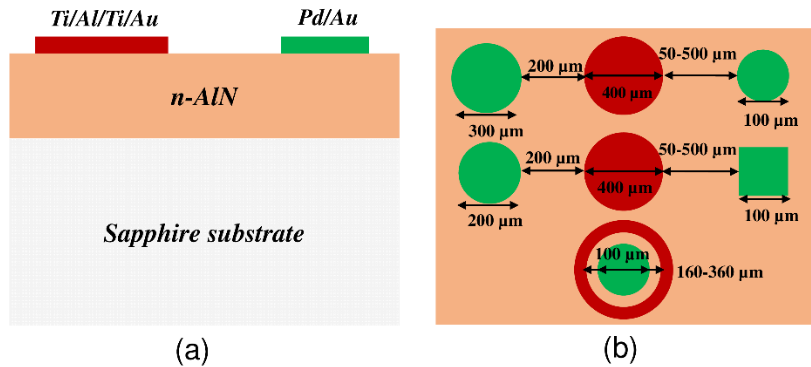

Fig. 53. (a) Schematic view of the cross-section of a lateral AlN SBD. (b) Top view of AlN SBDs with different geometries.

Due to strong polar nature of AlN, large amount of surface states exist on the AlN surface. However, the effects of surface states on reverse breakdown and current leakage of AlN SBDs have not yet been investigated, and their high temperature performance is still unclear. The AlN epilayers were grown by MOCVD on sapphire substrates. The Al

and N sources were trimethylaluminum (TMAl) and NH_3, respectively. SiH_4 was the precursor for n-type donor Si. The carrier gas was H_2. After growth, we fabricated lateral Pd/AlN SBDs with various devices geometries (Fig. 53) and their temperature-dependent current-voltage characteristics were comprehensively analyzed [125]. The reverse V_{BD} decreases with increasing operating temperature (Fig. 54), indicating that the breakdown is surface-dominated breakdown [127] that is possibly associated with surface states between Schottky contact and ohmic contact. These surface states, possibly originated from the threading dislocations accessible at the surface, dangling bonds, and ions absorbed from the environment, are commonly observed in III-nitride devices [128]. Furthermore, Fig. 55 shows that the reverse leakage current has a positive temperature dependence and is well fitted by the variable-range hopping (VRH) conduction model [125]. These results suggest that surface states can adversely affect the device performance of AlN SBDs, such as reverse breakdown and current leakage. Plotting the reverse V_{BD} and leakage current vs. contact distance, Fig. 56 shows a surface breakdown electric field of 450V/cm and a surface leakage current of 0.4 µA/cm at −30V.

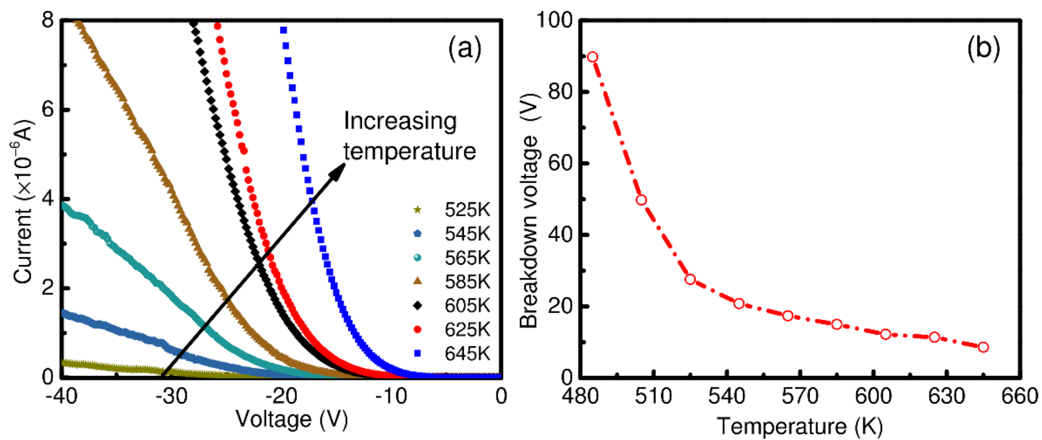

Fig. 54. (a) Temperature-dependent reverse I–V characteristics of AlN SBDs. (b) V_{BD} vs. temperature.

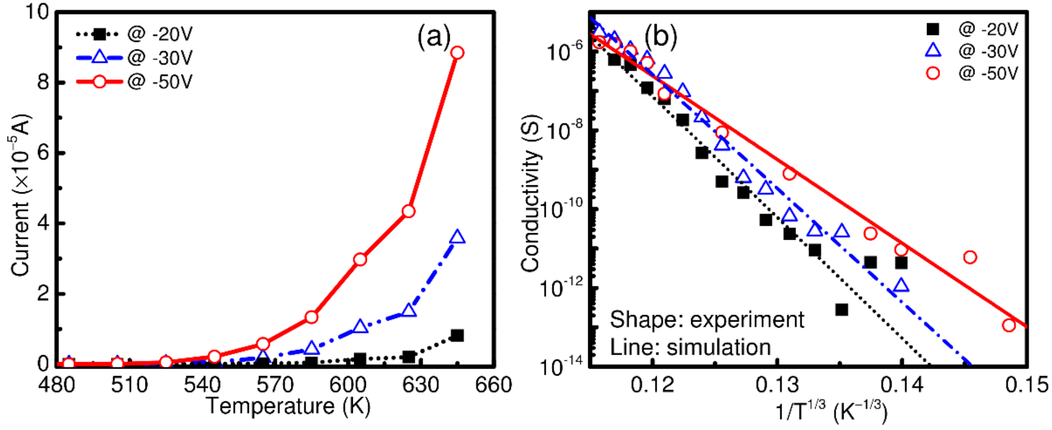

Fig. 55. (a) Temperature-dependent reverse leakage current at different reverse voltages. (b) Conductivity of AlN SBDs as a function of $1/T^{1/3}$ at different reverse voltages.

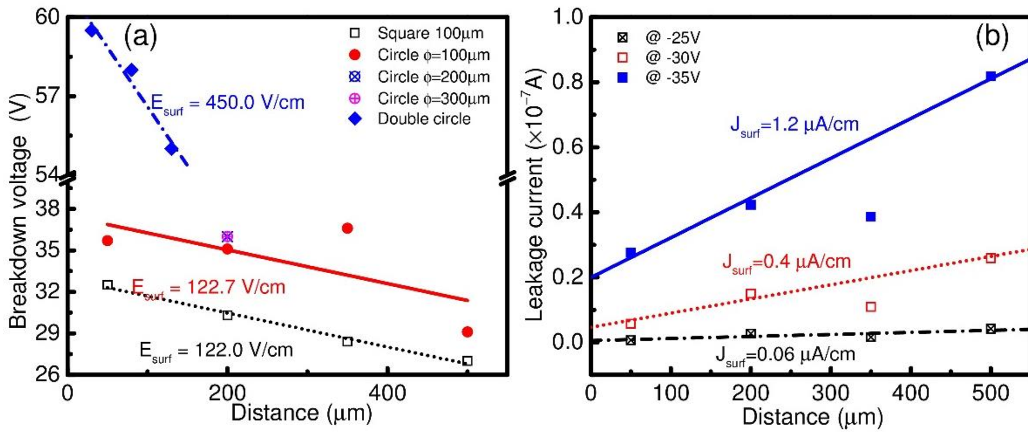

Fig. 56. (a) V_{BD} vs. contact distance. (b) Leakage current vs. contact distance at different reverse voltages.

7.2.3 1-kV-Class AlN SBDs

Figure 57 schematically show the device structure of the AlN SBDs, which consists of an AlN buffer layer, a 1-μm-thick UID AlN underlayer (UL), a 300 nm Si-doped n-AlN layer and a 2 nm GaN capping layer. The thin GaN capping layer was used to prevent the oxidation of AlN.

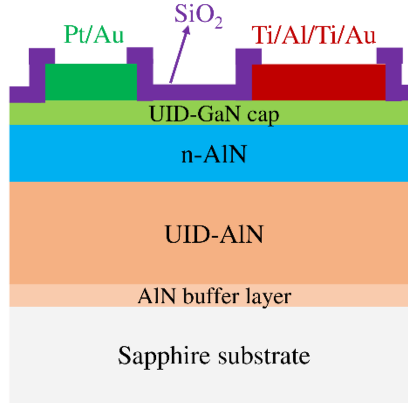

Fig. 57. Schematic view of the fabricated AlN SBDs.

The device fabrication process is similar to what was described in Section 4. The distance between the ohmic contact and Schottky contact is 200 µm. We added a 200 nm SiO_2 passivation layer on the devices using plasma-enhanced chemical vapor deposition (PECVD) at 350 °C and a RF power of 20 W. Finally, the fluorine-based reactive ion etching (RIE) was used to open the contact vias.

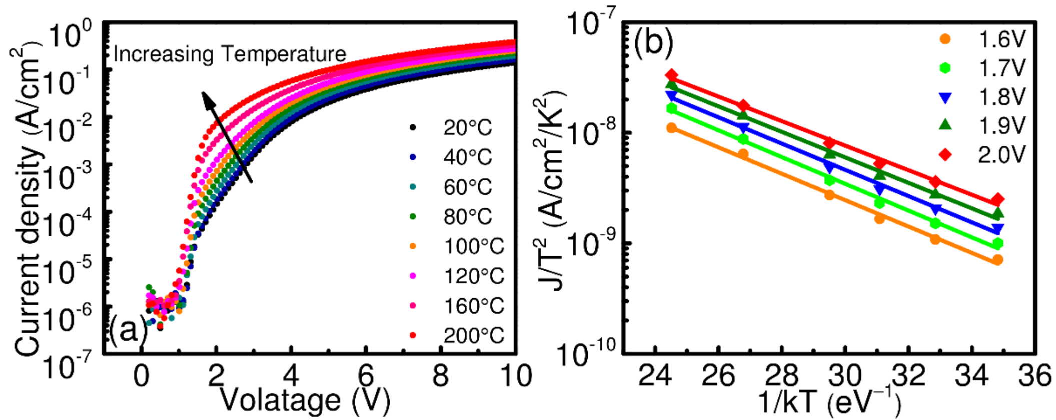

Fig. 58. (a) Temperature-dependent forward I–V characteristics. (b) The Richardson plot from 1.6V to 2.0 V.

As shown in Figure 58(a), the on/off ratio was ~10^5 and the V_{on} was 1.2 V. The slope of Richardson plot in Fig. 58(b) was constant, indicating the current conduction mechanism is thermionic emission [129].

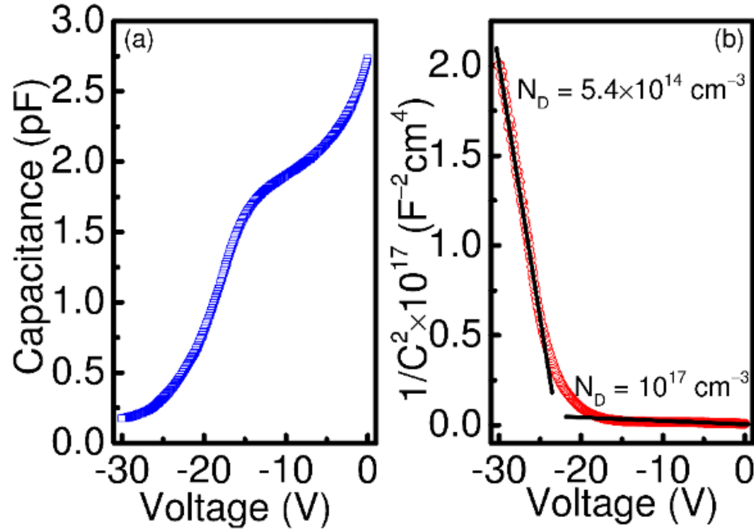

Fig. 59. C-V and $1/C^2$ vs. V characteristics for AlN SBDs at 1 MHz.

In Fig. 59, two slopes were observed $1/C^2$ vs. V. They corresponded to the n-AlN layer (10^{17} cm^{-3}) and resistive UID AlN UL (5.4×10^{14} cm^{-3}), respectively. The Silvaco ATLAS simulation showed the majority of current were confined in the thin n-AlN layer due to the resistive UID AlN UL. Therefore, it's desired to grow thick resistive UID AlN UL since they can not only improve the material quality of n-AlN epilayer, but may also reduce the current leakage pathways and increase V_{BD}.

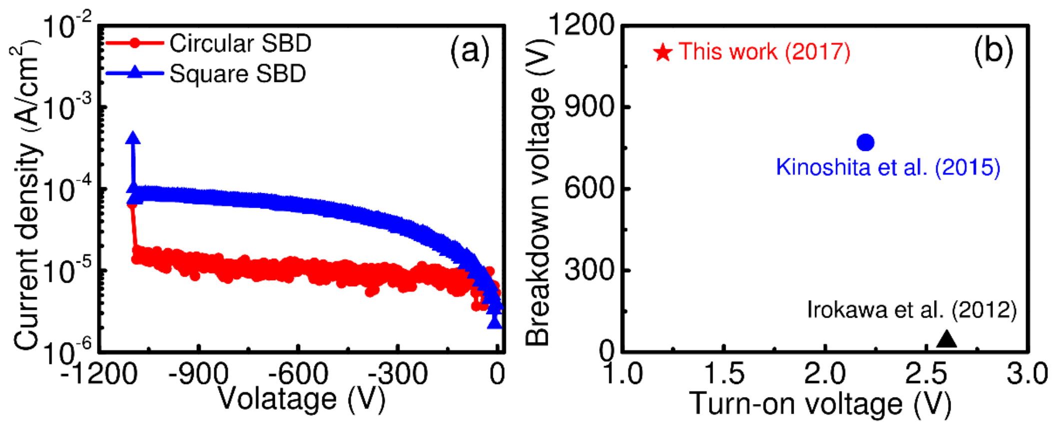

Fig. 60. (a) Reverse I-V characteristics of circular and square AlN SBDs. (b) Comparison of V_{BD} and V_{on} of reported AlN SBDs.

The AlN SBDs exhibited a V_{BD} of over 1 kV as shown in Fig. 60(a), which are higher than all the previous reports [130], [131]. The breakdown was hard breakdown with catastrophic damages at the edge of Schottky contacts due to the edge electric field crowding effects. V_{BD} can be further increased by employing FP and/or edge termination, improving the material quality, increasing the resistivity of the UID AlN UL and optimizing passivation. These results showed the great potential of AlN SBDs on sapphire for high power and high voltage applications.

7.2.4 Challenges and Proposed Work

The first challenge is the epitaxial growth of AlN materials with good crystal quality on different substrates, e.g., low defect densities in as-grown layers. Defects will act as major leakage pathways that reduce V_{BD} and increase leakage current. The effect of defects on electrical properties of AlN SBDs is however poorly understood. Single crystal AlN bulk substrate are currently available and will be used to improve the epitaxial layer quality compared with that grown on sapphire. The second challenge is growing thick epilayers with low doping concentrations. The V_{BD} is determined by the epilayer thickness and doping concentration. Comprehensive studies on growth conditions are needed, and material characterization such as XRD, TEM and Hall measurement should be performed to extract the key material parameters. Third, it's observed that surface states can considerably influence the device performance of AlN SBDs grown on sapphire without any surface treatments or passivation. Effective passivation methods are highly desired. Fourth, lateral AlN SBDs suffer from surface states related issues and pseudo and fully vertical structures should be developed to enhance device performance.

CHAPTER 8

CONCLUSIONS AND OUTLOOK

8.1 Conclusions

III-nitride material systems have been the workhorse of various optoelectronic and electronic technologies. InGaN based LEDs have revolutionized our lifestyle and made our life more energy-efficient and environmentally friendly. However, the reduction of efficiency with increasing current density and temperature hinders the potential of LEDs. We have proposed systematic research to explain and address the thermal droop problem, including investigation of thermal escape, QCSE, defects, Auger recombination, alloy fluctuations, phonon scattering and so on. On the other hand, III-nitride ISBT devices offer great advantages for THz and FIR applications. Certain semipolar planes ($55° < \theta < 90°$) are found to have improved device performance compared with both the *c*-plane and *m*-plane in terms of material quality, efficiency and transition frequency. Furthermore, a novel application of LEDs in visible light communication (LiFi) has attracted considerable interests [132]. Combining plasmonic effects and material modifications, high speed LEDs can be achieved to support the development of LiFi.

In the area of electronic devices, GaN, Ga_2O_3 and AlN based electronics will play an increasingly important role due to their high critical electric field and thermal conductivity, which can outperform current SiC based devices. For GaN power diodes, we demonstrated thick buffer layer designs, a hydrogen-plasma based edge termination technique and double-drift-layer designs to improve device performance. These methods may be applied to other semiconductor based power electronics. For Ga_2O_3 devices, we

identified the anisotropic electrical properties of Ga_2O_3 SBDs. There is a high probability that other semiconductors can exhibit the similar phenomenon. For AlN devices, surface states and leakage may adversely impact the device performance. Proper surface passivation and treatment are needed. In addition, designing vertical AlN devices will not only avoid surface issues, but also realize better devices with smaller size.

8.2 Outlook

Recent years have witnessed the tremendous progress in WBG semiconductor materials and devices. There are several interesting and important research topics that need to be extensively investigated to further advance this field.

The first topic is that of selective-area doping in GaN power electronics. The goal is to demonstrate randomly placed, reliable, contactable, and generally usable lateral p-n junctions. Figure 61(a) schematically shows the lateral p-n junction. In the other WBG semiconductor SiC, this lateral p-n junction can be readily realized by ion-implantation. How, ion-implantation technique in GaN is far from mature and faces inherent material challenges. The first challenge is that the postimplantation annealing temperature in GaN is limited to ~1000 °C because of severe decomposition of GaN at high temperatures. In contrast, SiC can stand over 1500 °C annealing temperatures. This annealing process is critical to the activation of implanted atoms and healing of the implantation damages. The second challenge is the low hole concentration in implanted p-GaN. It’s been reported that the state-of-the-art hole concentration in implanted p-GaN is 1-2 orders of magnitude lower than epitaxially grown p-GaN [133]. Therefore, the epitaxial growth method is the preferred method to achieve lateral p-n junctions. Figure 61(b)-(c) show the proposed growth steps of this junction. First, the n-GaN is grown by MOCVD; then, part of the n-

GaN is etched away by dry etching; finally, the p-GaN is regrown by MOCVD in the etched regions. There is also a reverse growth method which starts with p-GaN growth and finishes with n-GaN regrowth.

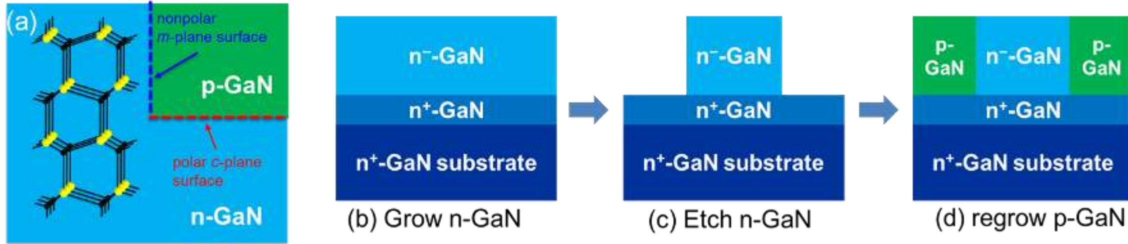

Fig. 61. (a) Schematics of the selective-area doping and the resulting lateral p-n junction. (b)-(c) The epitaxial growth and regrowth process for the lateral p-n junction.

The successful realization of the lateral p-n junction can enable a variety of advanced device structures in GaN power electronics [134]. Figure 62 shows several possible structures including junction barrier Schottky (JBS) or merged PIN Schottky (MPS) diodes, superjunctions, and vertical junction field effect transistors (VJFETs).

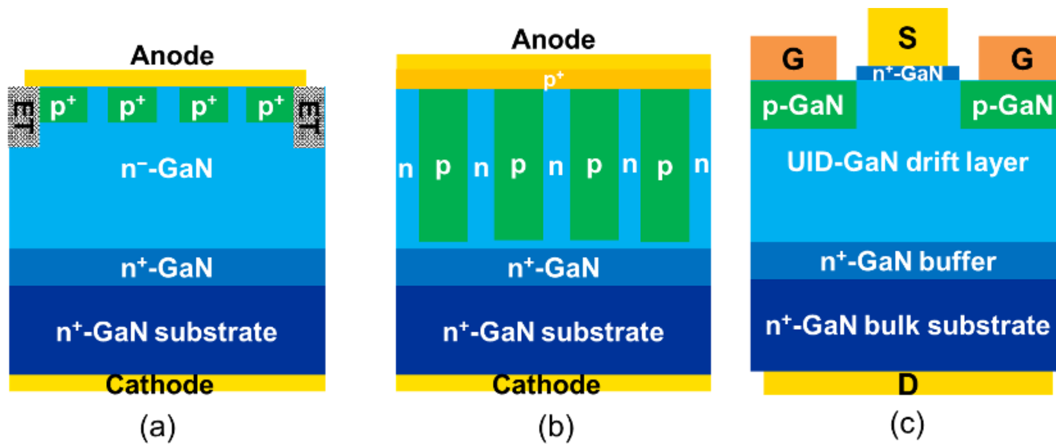

Fig. 62. (a) JBS or MPS diodes. (b) Superjunctions. (c) VJFETs.

There are also several challenges associated with the epitaxial growth method. The first one is the accumulation of impurities at the regrown interface as shown in Fig.

63(a), where high concentration of Si and O were observed [135]. O may come from the atmosphere or metalorganic precursors, and the origin of Si is still unclear and needs further investigation. These impurities serve as donors and can adversely affect the device performance. The proposed methods to mitigate the effects include HF treatment, insertion layer, p-type compensation layer and so on. The second one is the interfacial defects and etching damages. As shown in Fig. 63(b), an interface between the regrown p-GaN and UID-GaN was clearly visible [135]. This interface is highly disordered and can impact the regrowth process and serve as leakage pathways in devices. Developing low-damage etching and damage-repairing techniques is necessary. The third one is the Mg deficiency in the sidewall of the regrown p-GaN revealed by cathodoluminescence (CL) in Fig. 63(c). The sidewall exhibited a darker contrast compared with the lower and upper mesa. This is due to different Mg incorporation rates along different crystal orientations during growth. Etching recipes that produce vertical mesa sidewall is needed.

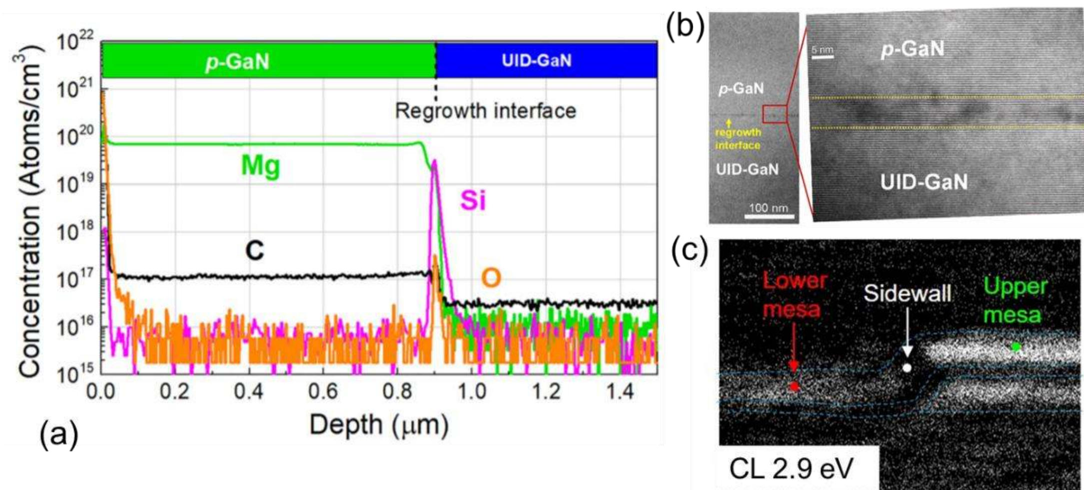

Fig. 63. (a) SIMS profile of the regrown p-n junction. (b) TEM images of the regrown p-n junction interface. (b) CL image of the regrown p-n junction.

The second topic is demonstrating vertical AlN power devices. XPS data [Fig. 64(a)] shows that there is a large upward band bending due to the high density of surface states on the order of 10^{14} $eV^{-1}cm^{-2}$. These surface states can significantly degrade device performances such as large leakage and current collapse, which are commonly observed in lateral devices. To avoid surface-related issues, vertical devices can be developed. Other advantages of vertical devices over lateral devices include larger voltage and current handling capabilities, smaller chip size and weight, and better thermal management. Figure 65(b)-(c) show two possible vertical AlN devices. In addition, the radiation effects on AlN devices are also worth investigating [136].

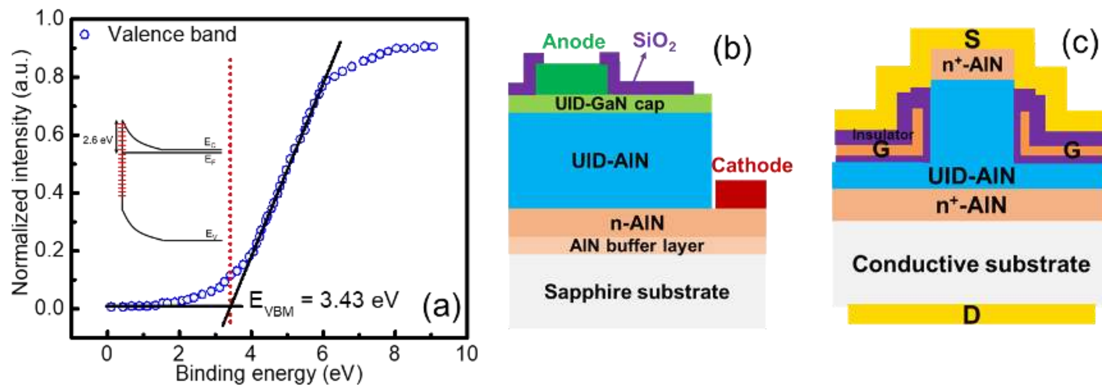

Fig. 64. (a) XPS valence band spectrum of AlN. (b) Vertical AlN SBDs. (c) Vertical AlN FinFETs.

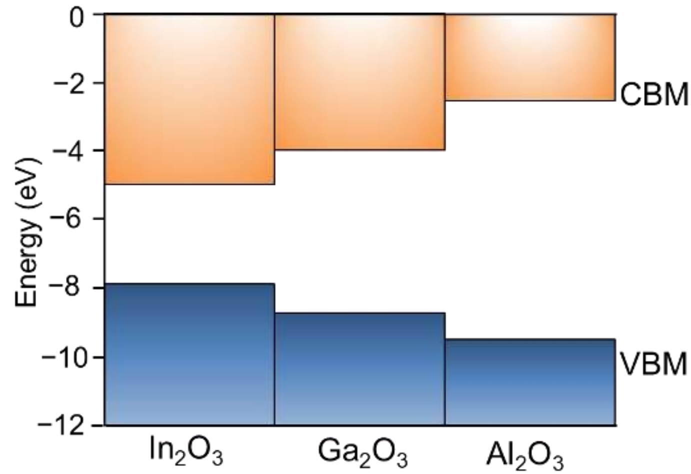

Fig. 65. Band alignments between In_2O_3, Ga_2O_3 and Al_2O_3.

The third topic is related to (Al, Ga, In)$_2$O$_3$ materials and devices. Recent research interests on the Ga_2O_3 have spurred tremendous efforts in growing (Al, Ga, In)$_2$O$_3$ materials and demonstrating their devices. Like the III-nitrides and its alloys (Al, Ga, In) N, oxides can also be alloyed with different compositions depending on the growth conditions. This dramatically expands the engineering space for oxide-based power electronics. Figure 65 shows the band alignments between In_2O_3, Ga_2O_3 and Al_2O_3. Heterostructure $(Al_xGa_{1-x})_2O_3/Ga_2O_3$ and associated transistors have been demonstrated [137], [138]. More efforts can be expected in the growth and devices of (Al, Ga, In)$_2$O$_3$, such as increasing the composition of Al, realizing $(In_xGa_{1-x})_2O_3$ growth, and forming double heterostructures and quantum wells for both electronic and optoelectronic applications. Another exploration direction is theoretical and experimental study of viable p-type dopants in Ga_2O_3.

REFERENCES

[1] Y. Zhao, H. Fu, G. T. Wang, and S. Nakamura, "Toward ultimate efficiency: progress and prospects on planar and 3D nanostructured nonpolar and semipolar InGaN light emitting diodes," *Adv. Opt. Photonics*, vol. 10, no. 1, pp. 246-308, Feb. 2018.

[2] C. C. Pan, Q. Yan, H. Fu, Y. Zhao, Y. R. Wu, C. G. Van de Walle, S. Nakamura, and S. P. DenBaars, "High optical power and low efficiency droop blue light-emitting diodes using compositionally step-graded InGaN barrier," *Electron. Lett*., vol. 51, no. 15, pp. 1187-1189, Jul. 2015.

[3] H. Chen, H. Fu, Z. Lu, X. Huang, and Y. Zhao, "Optical properties of highly polarized InGaN light-emitting diodes modified by plasmonic metallic grating," *Opt. Express*, vol. 24, no. 10, pp. A856- A867, Apr. 2016.

[4] H. Chen, H. Fu, X. Huang, Z. Lu, X. Zhang, J. Montes, and Y. Zhao, "Optical cavity effects in InGaN core-shell light-emitting diodes with metallic coating," *IEEE Photonics J*., vol. 9, no.3, p. 8200808, Jun. 2017.

[5] S. Nakamura, G. Fasol, and S. J. Pearton, "The Blue Laser Diode: The Complete Story," 2nd ed., *Springer*, Berlin, Germany, 2000.

[6] M. Beeler, E. Trichas, and E. Monroy, "III-nitride semiconductors for intersubband optoelectronics: a review," *Semicond. Sci. Technol*., vol. 28, no. 7, p. 074022, Jun. 2013.

[7] X. Huang, H. Fu, H. Chen, Z. Lu, D. Ding, and Y. Zhao, "Analysis of loss mechanisms in InGaN solar cells using a semi-analytical model," *J. Appl. Phys*., vol. 119, no. 21, p. 213101, Jun. 2016.

[8] X. Huang, H. Fu, H. Chen, X. Zhang, Z. Lu, J. Montes, M. Iza, S. P. DenBaars, S. Nakamura, and Y. Zhao, "Nonpolar and semipolar InGaN/GaN multiple-quantum-well solar cells with improved carrier collection efficiency," *Appl. Phys. Lett*., vol. 110, no. 16, p. 161105, Apr. 2017.

[9] X. Huang, H. Fu, H. Chen, Z. Lu, I. Baranowski, J. Montes, T. H. Yang, B. P. Gunning, D. Koleske, and Y. Zhao, "Reliability analysis of InGaN/GaN multi-quantum-well (MQW) solar cells under thermal stress," *Appl. Phys. Lett*., vol. 111, no. 23, p. 233511, Dec. 2017.

[10] H. Chen, X. Huang, H. Fu, Z. Lu, X. Zhang, J. A. Montes, and Y. Zhao "Characterizations of nonlinear optical properties on GaN crystals in polar, nonpolar, and semipolar orientations," *Appl. Phys. Lett*., vol. 110, no. 18, p. 181110, May 2017.

[11] Y. Wu, D. Kapolnek, J. P. Ibbetson, P. Parikh, B. P. Keller, and U. K. Mishra, "Very-high power density AlGaN/GaN HEMTs," *IEEE Trans. Electron Devices*, vol. 48, no. 3, pp. 586-590, Mar. 2001.

[12] I. C. Kizilyalli, A. P. Edwards, O. Aktas, T. Prunty, and D. Bour, "Vertical power p-n diodes based on bulk GaN," *IEEE Trans. Electron Devices*, vol. 62, no. 2, pp. 414-422, Feb. 2015.

[13] Y. Cao, R. Chu, R. Li, M. Chen, R. Chang, and B. Hughes, "High-voltage vertical GaN Schottky diode enabled by low-carbon metal-organic chemical vapor deposition growth," *Appl. Phys. Lett*., vol. 108, no. 6, p. 062103, Feb. 2016.

[14] Y. Zhao, "High performance semipolar blue and green III-nitride light-emitting diodes," PhD Dissertation, UCSB, Dec. 2012.

[15] E. Bellotti, K. Driscoll, T. Moustakas, and R. Paiella, "Monte Carlo study of GaN versus GaAs terahertz quantum cascade structures," *Appl. Phys. Lett*., vol. 92, no. 10, p. 101112, Mar. 2008.

[16] D. Feezell, Y. Sharma, and S. Krishna, "Optical properties of nonpolar III-nitrides for intersubband photodetectors," *J. Appl. Phys*., vol. 113, no. 13, p. 133103, Apr. 2013.

[17] N. Horiuchi, "Terahertz technology: Endless applications," *Nat. Photon*., vol. 4, no. 3, p. 140, Mar. 2010.

[18] S. Chowdhury, and U. K. Mishra, "Lateral and vertical transistors using the AlGaN/GaN heterostructure," *IEEE Trans. Electron Devices*, vol. 60, no. 10, pp. 3060-3066, Oct. 2013.

[19] H. Fu, and Y. Zhao, "Efficiency droop in GaInN/GaN LEDs," Nitride Semiconductor Light-Emitting Diodes (LEDs): Materials, Technologies, and Applications, ch. 9, Woodhead Publishing, 2017.

[20] Y. Zhao, R. M. Farrell, Y. R. Wu, and J. S. Speck, "Valence band states and polarized optical emission from nonpolar and semipolar III–nitride quantum well optoelectronic devices" *Jpn. J. Appl. Phys*., vol. 53, no. 10, p. 100206, Sept. 2014.

[21] A. Romanov, T. Baker, S. Nakamura, and J. S. Speck, "Strain-induced polarization in wurtzite III-nitride semipolar layers," *J. Appl. Phys*., vol. 100, no. 2, p. 023522, Jul. 2006.

[22] V. Fiorentini, F. Bernardini, F. Della Sala, A. Di Carlo, and P. Lugli, "Effects of macroscopic polarization in III-V nitride multiple quantum wells," *Phys. Rev. B*, vol. 60, no. 12, p. 8849, Sept. 1999.

[23] K. Fujito, S. Kubo, H. Nagaoka, T. Mochizuki, H. Namita, and S. Nagao, “Bulk GaN crystals grown by HVPE,” *J. Cryst. Growth*, vol. 311, no. 10, pp. 3011-3014, May 2009.

[24] T. Hashimoto, F. Wu, J. S. Speck, and S. Nakamura, “A GaN bulk crystal with improved structural quality grown by the ammonothermal method,” *Nat. Mat*., vol. 6, pp. 568-571, Jul. 2007.

[25] M. H. Kim, M. F. Schubert, Q. Dai, J. K. Kim, E. F. Schubert, J. Piprek, and Y. Park, “Origin of efficiency droop in GaN-based light-emitting diodes,” *Appl. Phys. Lett.*, vol. 91, no. 18, p. 183507, Oct. 2007.

[26] Y. Zhao, S. Tanaka, C. C. Pan, K. Fujito, D. Feezell, J. S. Speck, S. P. DenBaars, and S. Nakamura, “High-power blue-violet semipolar $(20\bar{2}\bar{1})$ InGaN/GaN light-emitting diodes with low efficiency droop up at 200A/cm^2,” *Appl. Phys. Express*, vol. 4, no. 8, p. 082104, Jul. 2011.

[27] J. Piprek, “Efficiency droop in nitride-based light-emitting diodes,” *Phys. Status Solidi A*, vol. 207, no. 10, pp. 2217-2225, Oct. 2010.

[28] C. Weisbuch, M. Piccardo, L. Martinelli, J. Iveland, J. Peretti, and J. S. Speck, “The efficiency challenge of nitride light‐emitting diodes for lighting,” *Phys. Status Solidi A*, vol. 212, no. 5, pp. 899-913, May 2015.

[29] J. Iveland, L. Martinelli, J. Peretti, J. S. Speck, and C. Weisbuch, “Direct measurement of auger electrons emitted from a semiconductor light-emitting diode under electrical injection: identification of the dominant mechanism for efficiency droop,” *Phys. Rev. Lett*., vol. 110, no. 17, p. 177406, Apr. 2013.

[30] J. Cho, E. F. Schubert, and J. K. Kim, “Efficiency droop in light‐emitting diodes: Challenges and countermeasures,” *Laser Photonics Rev*., vol. 7, no. 3, pp. 408-421, May 2013.

[31] H. Y. Ryu, D. S. Shin, and J. I. Shim, “Analysis of efficiency droop in nitride light-emitting diodes by the reduced effective volume of InGaN active material,” *Appl. Phys. Lett*., vol. 100, no. 13, p. 131109, Mar. 2012.

[32] J. Wang, L. Wang, W. Zhao, Z. Hao, and Y. Luo, “Understanding efficiency droop effect in InGaN/GaN multiple-quantum-well blue light-emitting diodes with different degree of carrier localization,” *Appl. Phys. Lett*., vol. 97, no. 20, p. 201112, Nov. 2010.

[33] B. Monemar and E. B. Sernelius, “Defect related issues in the ‘current roll-off’ in InGaN based light emitting diodes” *Appl. Phys. Lett.*, vol. 91, no. 18, p. 181103, Oct. 2007.

[34] E. Kioupakis, P. Rinke, K. T. Delaney C. G. Van de Walle, "Indirect Auger recombination as a cause of efficiency droop in nitride light-emitting diodes," *Appl. Phys. Lett.*, vol. 98, no. 16, p. 161107, Apr. 2011.

[35] Q. Dai, Q. Shan, J.Wang, S. Chhajed, J. Cho, E. F. Schubert, M. H. Crawford, D. D. Koleske, M.-H. Kim, and Y. Park, "Carrier recombination mechanisms and efficiency droop in GaInN/GaN light-emitting diodes," *Appl. Phys. Lett*., vol. 97, no. 13, p. 133507, Sept. 2010.

[36] S. F. Chichibu, A. Uedono, T. Onuma, B. A. Haskell, A. Chakraborty, T. Koyama, P. T. Fini, S. Keller, S. P. DenBaars, J. S. Speck, U. K. Mishra, S. Nakamura, S. Yamaguchi, S. Kamiyama, H. Amano, I. Akasaki, J. Han, and T. Sota, "Origin of defect-insensitive emission probability in In-containing (Al, In, Ga)N alloy semiconductors" *Nat. Mat.*, vol. 5, pp. 810-816, Sept. 2006.

[37] A. David and M. J. Grundmann, "Droop in InGaN light-emitting diodes: A differential carrier lifetime analysis," *Appl. Phys. Lett.*, vol. 96, no. 10, p. 103504, Mar. 2010.

[38] P. Walterweit, O. Brandt, A. Trampert, H. T. Grahn, J. Menniger, M. Ramsteiner, M. Reiche, and K. H. Ploog, "Nitride semiconductors free of electrostatic fields for efficient white light-emitting diodes," *Nature*, vol. 406, pp. 865-868, Aug. 2000.

[39] D. L. Becerra, Y. Zhao, S. H. Oh, C. D. Pynn, K. Fujito, S. P. DenBaars, and S. Nakamura, "High-power low-droop violet semipolar ($30\bar{3}\bar{1}$) InGaN/GaN light-emitting diodes with thick active layer design," *Appl. Phys. Lett.*, vol. 105, no. 17, p. 171106, Oct. 2014.

[40] S. Nakamura and M.R. Krames, "History of gallium–nitride-based light-emitting diodes for illumination," *Proc. IEEE*, vol. 101, no. 10, pp. 2211-2220, Aug. 2013.

[41] J. Hader, J. V. Moloney, and S. W. Koch, "Beyond the ABC: Carrier Recombinations in Semiconductor Lasers," *Proc. SPIE*, vol. 6115, p. 61151T, Feb. 2006.

[42] H. Fu, Z. Lu, and Y. Zhao, "Analysis of low efficiency droop of semipolar InGaN quantum well light-emitting diodes by modified rate equation with weak phase-space filling effect", *AIP Adv*., vol. 6, no. 6, p. 065013, Jun. 2016.

[43] H. Fu, Z. Lu, X. Zhao, Y. Zhang, S. P. DenBaars, S. Nakamura and Y. Zhao, "Study of low efficiency droop in semipolar ($20\bar{2}\bar{1}$) InGaN light-emitting diodes by time-resolved photoluminescence," *J. Disp. Technol*., vol. 12, no. 7, pp. 736-741, Jul. 2016.

[44] T. Onuma, Y. Sugiura, T. Yamaguchi, T. Honda, and M. Higashiwaki, "Impacts of AlO_x formation on emission properties of AlN/GaN heterostructures," *Appl. Phys. Express*, vol. 8, no. 5, p. 052401, Apr. 2015.

[45] D. Zhu, C. McAleese, M. Haberle, C. Salcianu, T. Thrush, M. Kappers, A. Phillips, P. Lane, M. Kane, D. Wallis, T. Martin, M. Astles, N. Hylton, P. Dawson and C. Humphreys, “Efficiency measurement of GaN-based quantum well and light-emitting diode structures grown on silicon substrate,” *J. Appl. Phys.*, vol. 109, no. 1, p. 014502, Jan. 2011.

[46] S. Deshpande, T. Frost, L. Yan, S. Jahangir, A. Hazari, X. Liu, J. M. Millunchick, Z. Mi and P. Bhattacharya, “Formation and nature of InGaN quantum dots in GaN nanowires”, *Nano Lett.*, vol. 15, no. 3, pp. 1647-1653, Feb. 2015.

[47] C. C. Pan, S. Tanaka, F. Wu, Y. Zhao, J. S. Speck, S. Nakamura, S. P. DenBaars, and D.
Feezell, “High-power, low-efficiency-droop semipolar $(20\bar{2}\bar{1})$single-quantum-well blue light-emitting diodes,” *Appl. Phys. Express*, vol. 5, no. 6, p. 062103, Jun. 2012.

[48] K. J. Vampola, N. N. Fellows, H. Masui, S. E. Brinkley, M. Furukawa, R. B. Chung, H. Sato, J. Sonoda, H. Hirasawa, M. Iza, S. P. DenBaars and S. Nakamura, “Highly efficient broad-area blue and white light-emitting diodes on bulk GaN substrates”, *Phys. Stat. Sol. A*, vol. 206, no. 2, pp. 200-202, Feb. 2009.

[49] Y. Narukawa, M. Ichikawa, D. Sanga, M. Sano, and T. Mukai, “White light emitting diodes with super-high luminous efficacy,” *J. Phys. D: Appl. Phys*., vol. 43, no. 35, p. 354002, Aug. 2010.

[50] M. B. Mclaurin, A. Hirai, E. Young, F. Wu, and J. S. Speck, “Basal plane stacking-fault related anisotropy in x-ray rocking curve widths of m-plane GaN,” *Jpn. J. Appl. Phys*., vol. 47, no. 7R, pp. 5429-5431, Jul. 2008.

[51] F. Wu, Y. D. Lin, A. Chakraborty, H. Ohta, S. P. DenBaars, S. Nakamura, and J. S. Speck, “Stacking fault formation in the long wavelength InGaN/GaN multiple quantum wells grown on m-plane GaN,” *Appl. Phys. Lett*., vol. 96, no. 23, p. 231912, May 2010.

[52] Y. Zhao, Q. Yan, C. Huang, S. Huang, P. Hsu, S. Tanaka, C. Pan, Y. Kawaguchi, K. Fujito, C. G. Van de Walle, J. Speck, S. DenBaars, S.Nakamura, and D. Feezell, “Indium incorporation and emission properties of nonpolar and semipolar InGaN quantum wells,” *Appl. Phys. Lett*., vol. 100, no. 20, p. 201108, May 2012.

[53] H. Fu, Z. Lu, X. Huang, H. Chen, and Y. Zhao, “Crystal orientation dependent intersubband transition in semipolar AlGaN/GaN single quantum well for optoelectronic applications,” *J. Appl. Phys.*, vol. 119, no. 17, p. 174502, May 2016.

[54] H. Fu, H. Chen, X. Huang, Z. Lu, and Y. Zhao, “Theoretical analysis of modulation doping effects on intersubband transition properties of semipolar AlGaN/GaN quantum well,” *J. Appl. Phys*., vol. 121, no. 1, p. 014501, Jan. 2017.

[55] V. F. Mymrin, K. A. Bulashevich, N. I. Podolskaya, I. A. Zhmakin, S. Yu. Karpov, and Yu. N. Makarov, "Modelling study of MQW LED operation," *Phys. Status Solidi C*, vol. 2, no. 7, pp. 2928-2931, May 2005.

[56] D. Ahn and S. Chuang, "Calculation of linear and nonlinear intersubband optical absorptions in a quantum well model with an applied electric field," *IEEE J. Quantum Electron*., vol. 23, no. 12, pp. 2196-2204, Dec 1987.

[57] J. J. Wierer Jr., D. D. Koleske, and S. R. Lee, "Influence of barrier thickness on the performance of InGaN/GaN multiple quantum well solar cells," *Appl. Phys. Lett*., vol. 100, no. 11, p. 111119, Mar. 2012.

[58] G. B. Lin, D. Y. Kim, G. Shan, J. Cho, E. F. Schubert, H. Shim, C. Sone, and J. K. Kim, "Effect of quantum barrier thickness in the multiple-quantum-well active region of GaInN/GaN light-emitting diodes," *IEEE Photon. J*., vol. 5, no. 4, p. 1600207, Aug. 2013.

[59] B. S. Zheng, P. Y. Chen, C. J. Yu, Y. F. Chang, C. L. Ho, M. C. Wu, and K. C. Hsieh, "Suppression of current leakage along mesa surfaces in GaN-based p-i-n diodes," *IEEE Electron Device Lett*., vol. 36, no. 9, pp. 932-934, Sep. 2015.

[60] C. Gupta, Y. Enatsu, G. Gupta, S. Keller, and U. K. Mishra, "High breakdown voltage p–n diodes on GaN on sapphire by MOCVD," *Phys. Status Solidi A*, vol. 213, no. 4, pp. 878-882, Apr. 2016.

[61] Y. Zhang, D. Piedra, M. Sun, J. Hennig, A. Dadgar, L. Yu, and T. Palacios, "High-performance 500 V quasi- and fully-vertical GaN-on-Si pn diodes," *IEEE Electron Device Lett*., vol. 38, no. 2, pp. 248–251, Feb. 2017.

[62] X. Zou, X. Zhang, X. Lu, C. W. Tang, and K. M. Lau, "Fully vertical GaN p-i-n diodes using GaN-on-Si epilayers," *IEEE Electron Device Lett*., vol. 37, no. 5, pp. 636-639, May 2016.

[63] S. Mase, T. Hamada, J. J. Freedsman, and T. Egawa, "Effect of drift Layer on the breakdown voltage of fully-vertical GaN-on-Si p-n diodes," *IEEE Electron Device Lett.*, vol. 38, no. 12, pp. 1720-1723, Dec. 2017.

[64] R. A. Khadar, C. Liu, L. Zhang, P. Xiang, K. Cheng, and E. Matioli, "820 V GaN-on-Si quasi-vertical p-i-n diodes with BFOM of 2.0 GW/cm^2," *IEEE Electron Device Lett*., vol. 39, no. 3, pp. 401-404, Mar. 2018.

[65] H. Fu, X. Huang, H. Chen, Z. Lu, X. Zhang, and Y. Zhao, "Effect of buffer layer design on vertical GaN-on-GaN p-n and Schottky power diodes," *IEEE Electron Device Lett*., vol. 38, no. 6, pp. 763-766, Jun. 2017.

[66] T. Ide, M. Shimizu, X. Q. Shen, K. Jeganathan, H. Okumura, and T. Nemoto, "Improvement of film quality using Si-doping in AlGaN/GaN heterostructure grown by plasma-assisted molecular beam epitaxy," *J. Crystal Growth*, vol. 245, no. 1-2, pp. 15-20, Nov. 2002.

[67] M. Qi, K. Nomoto, M. Zhu, Z. Hu, Y. Zhao, V. Protasenoko, B. Song, X. Yan, G. Li, J. Verma, S. Bader, P. Fay, H. G. Xing and D. Jena, "High breakdown single-crystal GaN p-n diodes by molecular beam epitaxy," *Appl. Phys. Lett*., vol. 107, no. 23, p. 232101, Dec. 2015.

[68] Z. Hu, K. Nomoto, B. Song, M. Zhu, M. Qi, M. Pan, X. Gao, V. Protasenko, D. Jena, and H. G. Xing, "Near unity ideality factor and Shockley-Read-Hall lifetime in GaN-on-GaN p-n diodes with avalanche breakdown," Appl. Phys. Lett., vol. 107, no. 24, p. 243501, Dec. 2015.

[69] K. Nomoto, B. Song, Z. Hu, M. Zhu, M. Qi, N. Kaneda, T. Mishima, T. Nakamura, D. Jena, and H. G. Xing, "1.7-kV and 0.55-mΩcm^2 GaN p-n diodes on bulk GaN substrates with avalanche capability," *IEEE Electron Device Lett*., vol. 37, no. 2, pp. 161–164, Feb. 2016.

[70] D. Cherns, and C. G. Jiao, "Electron holography studies of the charge on dislocations in GaN," *Phys. Rev. Lett*., vol. 87, no. 20, p. 205504, Oct. 2002.

[71] A. M. Ozbek and B. J. Baliga, "Planar nearly ideal edge-termination technique for GaN devices," *IEEE Electron Device Lett*., vol. 32, no. 3, pp. 300-302, Mar. 2011.

[72] S. Han, S. Yang, and K. Sheng, "High-voltage and high-I_{ON}/I_{OFF} vertical GaN-on-GaN Schottky varrier diode with nitridation-based termination," *IEEE Electron Device Lett*., vol. 39, no. 4, pp. 572-575, Apr. 2018.

[73] W. Sung, E. V. Brunt, B. J. Baliga, and A. Q. Huang, "A new edge termination technique for high-voltage devices in 4H-SiC-multiple-floating-zone junction termination extensioin," *IEEE Electron Device Lett.*, vol. 32, no. 7, pp. 880-882, Jul. 2011.

[74] A. V. Bolotnikov, P. G. Muzykov, Q. Zhang, A. K. Agarwal, and T. S. Sudarshan, "Junction termination extension implementing drive-in diffusion of boron for high-voltage SiC devices," *IEEE Trans. Electron Devices*, vol. 57, no. 8, pp. 1930-1935, Aug. 2010.

[75] R. Ghandi, B. Buono, M. Domeij, C.-M. Zetterling, and M. Östling, "High Voltage (2.8 kV) implantation-free 4H-SiC BJTs with long-term stability of the current gain," *IEEE Trans. Electron Devices*, vol. 58, no. 8, pp. 2665 – 2669, Jun. 2011.

[76] A. Salemi, H. Elahipanah, K. Jacobs, C.-M. Zetterling, and M. Östling, “15 kV-Class implantation-free 4H-SiC BJTs with record high current gain,” *IEEE Electron Device Lett*., vol. 39, no. 1, pp. 63-66, Jan. 2018.

[77] H. Fu, K. Fu, X. Huang, H. Chen, I. Baranowski, T. H. Yang, J. Montes, and Y. Zhao, “High performance vertical GaN-on-GaN p-n diodes with hydrogen-plasma based edge termination,” *IEEE Electron Device Lett*., accepted, 2018.

[78] S. Nakamura, N. Iwasa, M. Senoh, and T. Mukai, “Hole compensation mechanism of p-type GaN films,” *Jpn. J. Appl. Phys*., vol. 31, no. 5A, pp. 1258-1266, Feb. 1992.

[79] R. Hao, N. Xu, G. Yu, L. Song, F. Chen, J. Zhao, X. Deng, X. Li, K. Cheng, K. Fu, Y. Cai, X. Zhang, and B. Zhang, “Studies on fabrication and reliability of GaN high-resistivity-cap-layer HEMT,” *IEEE Trans. Electron Devices*, vol. 65, no. 4, pp. 1314-1320, Apr. 2018.

[80] X. A. Cao, H. Lu, S. F. LeBoeuf, C. Cowen, S. D. Arthur and W. Wang “Growth and characterization of GaN PiN rectifiers on free-standing GaN,” *Appl. Phys. Lett*., vol 87, no 5, p. 053503, Jul. 2005.

[81] Y. Yoshizumi, S. Hashimoto, T. Tanabe, and M. Kiyama, “High-breakdown-voltage pn-junction diodes on GaN substrates,” *J. Cryst. Growth*, vol. 298, pp. 875-878, Jan. 2007

[82] K. Nomoto, Y. Hatakeyama, H. Katayose, N. Kaneda, T. Mishima, and T. Nakamura, “Over 1.0 kV GaN p-n junction diodes on free-standing GaN substrates,” *Phys. Status Solidi (A)*, vol. 208, no. 7, pp. 1535-1537, Jul. 2011.

[83] Y. Hatakeyama, K. Nomoto, A. Terano, N. Kaneda, T. Tsuchiya, T. Mishima, and T. Nakamura, “High-breakdown-voltage and low-Specific-on-resistance GaN p–n junction diodes on free-standing GaN substrates fabricated through low-damage field-plate process,” *Jpn. J. Appl. Phys*., vol. 52, no. 2R, p. 028007, Feb. 2013.

[84] H. Ohta, N. Kaneda, F. Horikiri, Y. Narita, T. Yoshida, T. Mishima, and T. Nakamura, Vertical GaN p-n Junction diodes with high breakdown voltages over 4 kV, *IEEE Electron Device Lett*., vol. 36, no. 11, pp. 1180-1182, Nov. 2015.

[85] K. Nomoto, Z. Hu, B. Song, M. Zhu, M. Qi, R. Yan, V. Protasenko, E. Imhoff, J. Kuo, N. Kaneda, T. Mishima, T. Nakamura, D. Jena, and H. G. Xing, “GaN-on-GaN p-n power diodes with 3.48 kV and 0.95 mΩcm^2: a record high figure-of-merit of 12.8 GW/cm^2”, *IEEE IEDM*, pp. 971-974, Dec. 2015.

[86] I. C. Kizilyalli, A. P. Edwards, H. Nie, D. Bour, T. Prunty, and D. Disney, “3.7 kV vertical GaN pn diodes,” *IEEE Electron Device Lett*., vol. 35, no. 2, pp. 247-249, Feb. 2014.

[87] I. C. Kizilyalli, A. P. Edwards, H. Nie, D. Disney, and D. Bour, “High voltage vertical GaN p-n diodes with avalanche capability,” *IEEE Trans. Electron Devices*, vol. 60, no. 10, pp. 3067-3070, Oct. 2013.

[88] J. B. Limb, D. Yoo, J.-H. Ryou, W. Lee, S.-C. Shen, and R. D. Dupuis, “High performance GaN pin rectifiers grown on free-standing GaN substrates,” *Electron. Lett.*, vol. 42, no. 22, pp. 1313-1314, Oct. 2006.

[89] H. Fu, X. Huang, H. Chen, Z. Lu, I. Baranowski, and Y. Zhao, “Ultra-low turn-on voltage and on-resistance vertical GaN-on-GaN Schottky power diodes with high mobility double drift layers,” *Appl. Phys. Lett.*, vol. 111, no. 15, p. 152102, Oct. 2017.

[90] Y. Saitoh, K. Sumiyoshi, M. Okada, T. Horii, T. Miyazaki, H. Shiomi, M. Ueno, K. Katayama, M. Kiyama, and T. Nakamura, “Extremely low on-resistance and high breakdown voltage observed in vertical GaN Schottky barrier diodes with high-mobility drift layers on low-dislocation-density GaN substrates,” *Appl. Phys. Express*, vol. 3, no. 8, p. 081001, Jul. 2010.

[91] N. Tanaka, K. Hasegawa, K. Yasunishi, N. Murakami, and T. Oka, “50 A vertical GaN Schottky barrier diode on a free-standing GaN substrate with blocking voltage of 790 V,” *Appl. Phys. Express*, vol. 8, no. 7, p. 071001, Jun. 2015.

[92] B. Ren, M. Liao, M. Sumiya, L. Wang, Y. Koide, and L. Sang, “Nearly ideal vertical GaN Schottky barrier diodes with ultralow turn-on voltage and on-resistance,” *Appl. Phys. Express*, vol. 10, no. 5, p. 051001, Mar. 2017.

[93] L. Wang, M. I. Nathan, T. H. Lim, M. A. Khan, and Q. Chen, “High barrier height GaN Schottky diodes: Pt/GaN and Pd/GaN,” *Appl. Phys. Lett.*, vol. 68, no. 9, p. 1267, Aug. 1996.

[94] S. Adachi, Properties of Group IV, III-V, and II-VI Semiconductors. John Wiley and Sons, Ltd., ch. 12, 2005.

[95] T. T. Mnatsakanov, M. E. Levinshtein, L. I. Pomortseva, S. N. Yurkov, G. S. Simin, and M.
A. Khan, “Carrier mobility model for GaN,” *Solid-State Electron.*, vol. 47, no. 1, pp. 111-115, Jan. 2003.

[96] S. Vitanov, V. Palankovski, S. Maroldt, and R. Quay, “High-temperature modeling of AlGaN/GaN HEMTs,” *Solid-State Electron.*, vol. 54, no. 10, pp. 1105-1112, Oct. 2010.

[97] T. Oishi, Y. Koga, K. Harada, and M. Kasu, "High-mobility *β*-Ga_2O_3 ($\bar{2}01$) single crystals grown by edge-defined film-fed growth method and their Schottky barrier diodes with Ni contact," *Appl. Phys. Express*, vol. 8, no. 3, p. 031101, Feb. 2015.

[98] Z. Guo, A. Verma, X. Wu, F. Sun, A. Hickman, T. Masui, A. Kuramata, M. Higashiwaki, D. Jena, T. Luo, "Anisotropic thermal conductivity in single crystal *β*-gallium oxide," *Appl. Phys. Lett*., vol. 106, no. 11, p. 111909, Mar. 2015.

[99] H. Chen, H. Fu, X. Huang, J. A. Montes, T. H. Yang, I. Baranowski, and Y. Zhao, "Characterizations of the nonlinear optical properties for (010) and ($\bar{2}01$) beta-phase gallium oxide," *Opt. Express*, vol. 26, no. 4, pp. 3938-3946, Feb. 2018.

[100] M. H. Wong, K. Sasaki, A. Kuramata, S. Yamakoshi, and M. Higashiwaki, "Electron channel mobility in silicon-doped Ga_2O_3 MOSFETs with a resistive buffer layer," *Jpn. J. Appl. Phys*., vol. 55, no. 12, p. 1202B9, Oct. 2016.

[101] M. Schubert, R. Korlacki, S. Knight, T. Hofmann, S. Schöche, V. Darakchieva, E. Janzén, B. Monemar, D. Gogova, Q.-T. Thieu, R. Togashi, H. Murakami, Y. Kumagai, K. Goto, A. Kuramata, S. Yamakoshi, and M. Higashiwaki, "Anisotropy, phonon modes, and free charge carrier parameters in monoclinic *β*-gallium oxide single crystals," *Phys. Rev. B*, vol. 93, no. 12, p. 125209, Mar. 2016.

[102] K. Sasaki, A. Kuramata, T. Masui, E. G. Víllora, K. Shimamura, and S. Yamakoshi, "Device-Quality *β*-Ga_2O_3 Epitaxial Films Fabricated by Ozone Molecular Beam Epitaxy," *Appl. Phys. Express*, vol. 5, no. 3, p. 035502, Feb. 2012.

[103] J. E. Hogan, S. W. Kaun, E. Ahmadi, Y. Oshima, and J. S. Speck, "Chlorine-based dry etching of *β*-Ga_2O_3," *Semicond. Sci. Technol.*, vol. 31, no. 6, p. 065006, Apr. 2016.

[104] S. Jang, S. Jung, K. Beers, J. Yang, F. Ren, A. Kuramata, S. J. Pearton, and K. H. Baik, "A comparative study of wet etching and contacts on ($\bar{2}01$) and (010) oriented *β*-Ga_2O_3," *J Alloys Compd*., vol. 731, pp. 118-125, Jan. 2018.

[105] H. Fu, H. Chen, X. Huang, I. Baranowski, J. Montes, T. H. Yang, and Y. Zhao, "A comparative study on the electrical properties of vertical ($\bar{2}01$) and (010) β-Ga_2O_3 Schottky barrier diodes on EFG single-crystal substrates," *IEEE Trans. Electron Devices*, under review, 2018.

[106] M. Kasu, T. Oshima, K. Hanada, T. Moribayashi, A. Hashiguchi, T. Oishi, K. Sasaki, A. Kuramata, and O. Ueda, "Crystal defects observed by the etch-pit method and their effects on Schottky-barrier-diode characteristics on ($\bar{2}01$) *β*-Ga_2O_3," *Jpn. J. Appl. Phys*., vol. 56, no. 9, p. 091101, Jul. 2017.

[107] P. Reddy, I Bryan, Z. Bryan, W. Guo, L. Hussey, R. Collazo, and Z. Sitar, "The effect of polarity and surface states on the Fermi level at III-nitride surfaces," *J. Appl. Phys.*, vol. 116, no. 12, p. 123701, Sept. 2014.

[108] M. Higashiwaki, K. Sasaki, A. Kuramata, T. Masui, and S. Yamakoshi, "Gallium oxide (Ga_2O_3) metal-semiconductor field-effect transistors on single-crystal β-Ga_2O_3 (010) substrates," *Appl. Phys. Lett.*, vol. 100, no. 1, p. 013504, Jan. 2012.

[109] J. Yang, S. Ahn, F. Ren, S. J. Pearton, S. Jang, and A. Kuramata, "High Breakdown Voltage ($\bar{2}01$) β-Ga_2O_3 Schottky Rectifiers," *IEEE Electron Device Lett*., vol. 38, no. 7, pp. 906-909, Jul. 2017.

[110] K. Sasaki, M. Higashiwaki, A. Kuramata, T. Masui, and S. Yamakoshi, "Ga_2O_3 Schottky barrier diodes fabricated by using single-crystal β– Ga_2O_3 (010) substrates," *IEEE Electron Device Lett.*, vol. 34, no. 4, pp. 493-495, Apr. 2013.

[111] Q. He, W. Mu, H. Dong, S. Long, Z. Jia, H. Lv, Q. Liu, M. Tang, X. Tao, and M. Liu, "Schottky barrier diode based on β-Ga_2O_3 (100) single crystal substrate and its temperature-dependent electrical characteristics," *Appl. Phys. Lett.*, vol. 110, no. 9, p. 093503, Mar. 2017.

[112] T. Oishi, K. Harada, Y. Koga, and M. Kasu, "Conduction mechanism in highly doped β-Ga_2O_3 ($\bar{2}01$) single crystals grown by edge-defined film-fed growth method and their Schottky barrier diodes," *Jpn. J. Appl. Phys*., vol. 55, no. 3, p. 030305, Feb. 2016.

[113] B. Song, A. K. Verma, K. Nomoto, M. Zhu, D. Jena, and H. G. Xing, "Vertical Ga2O3 Schottky barrier diodes on single-crystal β-Ga_2O_3 ($\bar{2}01$) substrates," in *Proc. 74th IEEE Device Res. Conf*., pp. 1-2, Aug. 2016.

[114] S. Ahn, F. Ren, L. Yuan, S. J. Pearton, and A. Kuramata, "Temperature-dependent characteristics of Ni/Au and Pt/Au Schottky diodes on β-Ga_2O_3," *ECS J. Solid State Sci. Technol*., vol. 6, no. 1, pp. P68-P72, Jan. 2017.

[115] K. Sasaki, D. Wakimoto, Q. T. Thieu, Y. Koishikawa, A. Kuramata, M. Higashiwaki, and S. Yamakoshi, "First demonstration of Ga_2O_3 trench MOS-type Schottky barrier diodes," *IEEE Electron Device Lett*., vol. 38, no. 6, pp. 783-785, Jun. 2017.

[116] M. Higashiwaki, K. Sasaki, K. Goto, K. Nomura, Q. T. Thieu, R. Togashi, H. Murakami, Y. Kumagai, B. Monemar, A. Koukitu, A. Kuramata, and S. Yamakoshi, "Ga_2O_3 Schottky barrier diodes with n^--Ga_2O_3 drift layers grown by HVPE" in *Proc. 73rd IEEE Device Res. Conf*., pp. 29-30, Aug. 2015.

[117] J. Yang, S. Ahn, F. Ren, S. J. Pearton, S. Jang, J. Kim, and A. Kuramata, "High reverse breakdown voltage Schottky rectifiers without edge termination on Ga_2O_3," *Appl. Phys. Lett*. vol. 110, no. 19, p. 192101, May 2017.

[118] Z. Zhang, E. Farzana, A. R. Arehart, and S. A. Ringel, "Deep level defects throughout the bandgap of (010) β-Ga_2O_3 detected by optically and thermally stimulated defect spectroscopy," *Appl. Phys. Lett.*, vol. 108, no. 5, p. 052105, Feb. 2016.

[119] A. M. Armstrong, M. H. Crawford, A. Jayawardena, A. Ahyi, and S. Dhar, "Role of self-trapped holes in the photoconductive gain of β-gallium oxide Schottky diodes," *J. Appl. Phys.*, vol. 119, no. 10, p. 103102 Mar. 2016.

[120] Y. Yao, R. Gangireddy, J. Kim, K. K. Das, R. F. Davis, and L. M. Porter, "Electrical behavior of β-Ga_2O_3 Schottky diodes with different Schottky metals," *J. Vac. Sci. Technol. B*, vol. 35, no. 3, p. 03D113, May 2017.

[121] M. Higashiwaki, K. Konishi, K. Sasaki, K. Goto, K. Nomura, Q. T. Thieu, R. Togashi, H. Murakami, Y. Kumagai, B. Monemar, A. Koukitu, A. Kuramata, and S. Yamakoshi, "Temperature-dependent capacitance–voltage and current–voltage characteristics of Pt/Ga_2O_3 (001) Schottky barrier diodes fabricated on n^-–Ga_2O_3 drift layers grown by halide vapor phase epitaxy," *Appl. Phys. Lett*., vol. 108, no. 13, p. 133503, Mar. 2016.

[122] F. Lucolano, F. Roccaforte, F. Giannazzo, and V. Raineri, "Barrier inhomogeneity and electrical properties of Pt/GaN Schottky contacts," *J. Appl. Phys*., vol. 102, no. 11, p. 113701, Dec. 2007.

[123] E. J. Miller, E. T. Yu, P. Waltereit, and J. S. Speck, "Analysis of reverse-bias leakage current mechanisms in GaN grown by molecular-beam epitaxy," *Appl. Phys. Lett*., vol. 84, no. 4, p. 535, Jan. 2004.

[124] J. Piprek, "Nitride semiconductor devices: principles and simulation," WILEY VCH, 1st edition, Apr. 2007.

[125] H. Fu, X. Huang, H. Chen, Z. Lu, and Y. Zhao, "Fabrication and characterization of ultra-wide bandgap AlN-based Schottky diodes on sapphire by MOCVD," *IEEE J. Electron Devices Soc*., vol. 5, no. 6, pp. 518-524, Nov. 2014.

[126] H. Fu, I. Baranowski, X. Huang, H. Chen, Z. Lu, J. Montes, X. Zhang, and Y. Zhao, "Demonstration of AlN Schottky barrier diodes with blocking voltage over 1 kV," *IEEE Electron Device Lett*., vol. 38, no. 9, pp. 1286-1289, Sept. 2017.

[127] Y. Ohno, T. Nakao, S. Kishimoto, K. Maezawa, and T. Mizutani, "Effects of surface passivation on breakdown of AlGaN/GaN high-electron-mobility transistors," *Appl. Phys. Lett.*, vol. 84, no. 12, pp. 2184-2186, Mar. 2004.

[128] B. M. Green, K. K. Chu, E. M. Chumbes, J. A. Smart, J. R. Shealy, and L. F. Eastman, "The effect of surface passivation on the microwave characteristics of undoped AlGaN/GaN HEMTs," *IEEE Electron Device Lett.*, vol. 21, no. 6, pp. 268-270, Jun. 2000.

[129] M. Dutta, F. Koeck, R. Hathwar, S. Goodnick, R. Nemanich, and S. Chowdhury, "Demonstration of diamond-based Schottky p-i-n diode with blocking voltage > 500 V," *IEEE Electron Device Lett*., vol. 37, no. 9, pp. 1170-1173, Sep. 2016.

[130] Y. Irokawa, E. Villora, and K. Shimamura, "Shottky Barrier Diodes on AlN Free-Standing Substrates," *Jpn. J. Appl. Phys*., vol. 51, no. 4R, p. 040206, Mar. 2012.

[131] T. Kinoshita, T. Nagashima, T. Obata, S. Takashima, R. Yamamoto, R. Togashi, Y. Kumagai, R. Schlesser, R. Collazo, A. Koukitu, and Z. Sitar, "Fabrication of vertical Schottky barrier diodes on n-type freestanding AlN substrates grown by hydride vapor phase epitaxy," *Appl. Phys. Express*, vol. 8, no. 6, p. 061003, May 2015.

[132] Z. Lu, P. Tian, H. Chen, I. Baranowski, H. Fu, X. Huang, J. Montes, Y. Fan, H. Wang, X. Liu, R. Liu, and Y. Zhao, "Active tracking system for visible light communication using a GaN-based micro-LED and NRZ-OOK," *Opt. Express*, vol. 25, no. 15, pp. 17971-17981, Jul. 2017.

[133] Y. Zhang, Z. Liu, M. J. Tadjer, M. Sun, D. Piedra, C. Hatem, T. J. Anderson, L. E. Luna, A. Nath, A. D. Koehler, H. Okumura, J. Hu, X. Zhang, X. Gao, B. N. Feigelson, K. D. Hobart, and T. Palacios, "Vertical GaN junction barrier Schottky rectifiers by selective ion implantation," *IEEE Electron Device Lett*., vol. 38, no. 8, pp. 1097-1100, Jun. 2017.

[134] H. Fu, X. Zhang, K. Fu, H. Liu, S. R. Alugubelli, X. Huang, H. Chen, I. Baranowski, Tsung-Han Yang, K. Xu, F. A. Ponce, B. Zhang, and Y. Zhao, "Nonpolar vertical GaN-on-GaN p-n diodes grown on free-standing (10-10) m-plane GaN substrates," *Appl. Phys. Express*, vol. 11, no. 11, p. 111003, Oct. 2018.

[135] K. Fu, H. Fu, H. Liu, S. R. Alugubelli, T.-H. Yang, X. Huang, H. Chen, I. Baranowski, J. Montes, F. A. Ponce, and Y. Zhao, "Investigation of GaN-on-GaN vertical p-n diode with regrown p-GaN by metalorganic chemical vapor deposition," *Appl. Phys. Lett*., vol. 113, no. 23, p. 233502, Dec. 2018.

[136] J. Montes, T.-H. Yang, H. Fu, H. Chen, X. Huang, K. Fu, I. Baranowski, and Y. Zhao, "Effect of proton radiation on ultra-wide bandgap AlN Schottky barrier diodes," *IEEE Trans. Nucl. Sci*., Nov. 2018.

[137] S. W. Kaun, F. Wu, and J. S. Speck, "β-$(Al_xGa_{1-x})_2O_3/Ga_2O_3$ (010) heterostructures grown on β-Ga_2O_3 (010) substrates by plasma-assisted molecular beam epitaxy," *J. Vac. Sci. Technol. A*, vol. 33, no. 4, p. 041508, Jun. 2015.

[138] Y. Zhang, A. Neal, Z. Xia, C. Joishi, J. M. Johnson, Y. Zheng, S. Bajaj, M. Brenner, D. Dorsey, K. Chabak, G. Jessen, J. Hwang, S. Mou, J. P. Heremans, and S. Rajan, "Demonstration of high mobility and quantum transport in modulation-doped β-$(Al_xGa_{1-x})_2O_3/Ga_2O_3$ heterostructures," *Appl. Phys. Lett.*, vol. 112, no. 17, p. 173502 Apr. 2018.